Improved Electrical Model and Experimental Validation of the PVMD Toolbox

Extending the Energy Yield Prediction Model to Tandem PV Modules

Abdallah Nour El Din

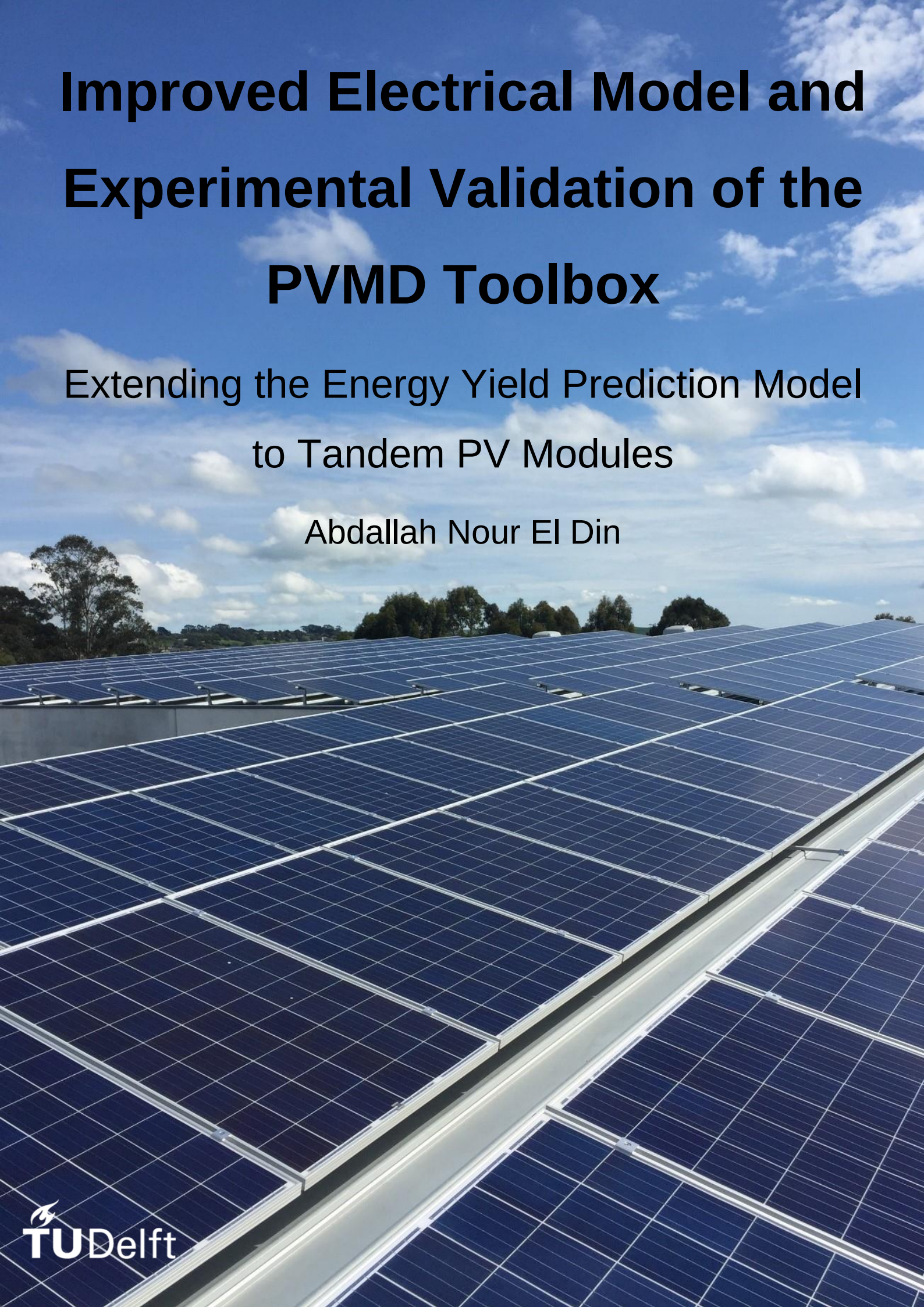

TU Delft

Improved Electrical Model and Experimental Validation of the PVMD Toolbox

Extending the Energy Yield Prediction Model to Tandem PV Modules

By

Abdallah Nour El Din (4789628)

in partial fulfilment of the requirements for the degree of

Master of Science* in *Sustainable Energy Technology

at the Delft University of Technology,

to be defended publicly on Wednesday July 15, 2020 at 10:00 am

Project duration:	11 November 2019 - 15 July 2020		
Thesis Committee:	Dr. O. Isabella	Associate Professor – PVMD	Supervisor
	Dr. R. Santbergen	Assistant Professor - PVMD	
	Dr. S.H. Tindemans	Assistant Professor – IEPG	External committee member
	Dr. M.R. Vogt	Postdoc - PVMD	Daily supervisor

TU Delft

PVMD Delft University of Technology

Preface

This thesis concludes my *Sustainable Energy Technology* master's program at Delft University of Technology. The last two years have been a challenging, yet exciting journey.

First, I would like to express my gratitude to my parents and siblings, *Mohammed* and *Fatima*, for their endless love and motivation. Besides, I would like to thank my lifelong companion, *Randa*. You, along with my family, are genuine partners of my success! كل الحب والشكر والتقدير

I would like to thank the *PVMD group* for the professional environment and cooperation. Besides, I would like to thank *Dr. Olindo* Isabella and *Dr. Malte Ruben Vogt* for sharing their knowledge and support. My gratitude is also to *Dr. Rudi Santbergen;* the work progress would have never been possible without your experience and insight. In addition, I am thankful to *Dr. Carlos Ruiz Tobon* and *Dr. Hesan Ziar* for their contributions to my thesis work.

I would like to thank one of my best friends, and by far the best study/project partner, *Patrycja*. My journey would have never been the same without my dear friends, *Georgia* and *Kyriakos*. Thank you for sharing unforgettable memories and experiences. In addition, I am grateful to my LB 02.500 officemates *Lyndon*, *Mohammed* and *Martijn* for making the office feel like a second home!

Now that this journey is over, I can say that it was nothing but a life-changing experience. It helped me grow on the personal and academic levels and it broadened my perspective. I hope that this research progress helps in the spread of green energy and in making this world a better place.

"The whole of science is nothing more than a refinement of everyday thinking."

Albert Einstein

Delft, July 8th 2020

Abdallah Nour El Din

Abstract

In the field of photovoltaics, tandem cells have emerged as a promising technology with high power conversion efficiencies. The academic society grew interest toward this technology due to its high generation capabilities at low production costs. For the time being, most of the research efforts are limited to the lab performance of these cells. However, real life performance studies allow for better understanding of the design effects and yield potentials of this technology.

The commercially available yield prediction tools do not involve energy yield prediction models for tandem modules. In addition, they fall short at modelling all the aspects influencing the PV energy yield. The PVMD Toolbox, developed by the Photovoltaic Materials and Devices group at Delft University of Technology, is proposed to serve this need.

This thesis presents the work done to develop version 4 of the toolbox. A *calibrated lumped element model (CLEM)* was developed to simulate the electric performance at the cell level. The *CLEM* combines the accuracy of physical models with the speed of lumped-element models to generate hundreds of thousands of simulations within a single minute. Additional models were implemented in the toolbox to account for the effects of cell interconnections and metallization on the energy output. Besides, a cell mapping algorithm was developed to reduce the AEY simulation time. This algorithm proved beneficial by reducing the number of required electric simulations by 86% at the small cost of 0.226% bias. Afterwards, the accuracy of the thermal and electric models was validated against two datasets. The simulated results showed a great agreement to the measurements with total energy yield deviations from the measurement of 2.65% and 4.15%, compared to 7.43% in version 3. Therefore, version 4 of the toolbox offers more accurate simulations with a reduced computation speed by a factor of 45.

The *CLEM* and cell interconnection models were utilized to perform energy yield simulations on tandem modules. Case studies were performed on c-Si/tandem modules to investigate the implications of design choices. After optimizing the STC output of four design options, the toolbox was used to simulate the energy yield for each of them. Then, the optical and electric performance of the modules were studied. The tandem modules proved advantageous, with energy yield increase ranging between 12.91% and 27.13% compared to SHJ modules. In addition, specific yield computations confirmed the sensitivity of tandem modules to meteorological conditions. The final result of this thesis is a first-time combination of modelling spectral irradiance, thermal, and cell and module electric aspects for energy yield simulations of tandem modules.

Contents

Nomenclature

LCOE	Levelised cost of energy
c-Si	Crystalline silicon
SHJ	Silicon heterojunction
AOI	Angle of incidence
Λ	Wavelength
AM	Air mass
FF	Fill factor
θ_s	Solar zenith angle
APE	Average photon energy
I_{ph}	Photo-generated current
n	Ideality factor
I_0	Saturation current
R_s	Series resistance
R_{sh}	Shunt resistance
EQE	External quantum efficiency
STC	Standard test conditions
q	Elementary charge
k_B	Boltzmann constant
Φ	Photon flux
σ	Stefan-Boltzmann constant
E_g	Bandgap energy
V_{th}	Thermal voltage
K_v	Voltage thermal coefficient
K_i	Current thermal coefficient
VBY	Bypass voltage
GHI	Global horizontal irradiance
DNI	Direct normal irradiance
DHI	Diffuse horizontal irradiance

RMSE	Root mean square difference
MBD	Mean bias difference
SBF	Slope of best-line fit
WIA	Willmott's index of agreement
E_{Ex}	Extra-terrestrial irradiance
E_{sc}	Solar constant
k_t	Sky clearness index
k_d	Diffuse coefficient
T_{SS}	Steady-state temperature
k	thermal conductivity
h_{forced}	Forced convection coefficient
h_{free}	Free convection coefficient
SD	Standard deviation of the residual
U_{95}	95% confidence interval
2TT	Two-terminal tandem
4TT	Four-terminal tandem
RT	Rear-textured
DT	Double-textured
PR	Performance ratio

1

Literature Study

This chapter is a review of the status quo to formulate the research questions. Section 1.1 presents an introduction to the trends and future of photovoltaic energy technology. Section 1.2 includes an overview of tandem cell technology and its working principles. Afterward, section 1.3 introduces state-of-the-art photovoltaic energy yield simulation tools and their key attributes. Later, the constituents, features, and limitations of the current version of the PVMD energy yield simulation toolbox are described in section 1.4. Based on the previous sections, the thesis objectives are defined in section 1.5, followed by a concise thesis outline in section 1.6.

1.1 Background

Our energy requirements, as human civilization, are intensifying due to growing economies and rising standards of living. In fact, 2018 witnessed a 2.9% growth in primary energy consumption, accompanied by a 2% increase in carbon emissions from energy use [1]. Currently, fossil fuels are the major constituents of energy resources used. However, because of the finite available fossil reserves and the pollution dilemma, renewable energy use is being advocated. The goal of the Paris Agreement of limiting global warming to 2°C, requires complete decarbonisation of the power sector and electrification by 2050 [2].

At present, a growing quantity of energy is being harvested from renewable energy sources, such as solar, wind, geothermal, hydro and tidal energy; the annual renewable energy generation grew from 3,898 TWh in 2009 to 6,191 TWh in 2017 [3]. Among the renewable energy sources solar energy is considered in favour when compared to other resources for several reasons. First, it is, by far, the energy source with the highest power potential available, with 23,000 TW incident power on the earth surface [4]. Besides, it is highly flexible in terms of capacity, with generation capacities ranging from watts to gigawatts. Furthermore, photovoltaic solar energy shows the most promising learning curve and the highest drop in costs among other available sources. This can be demonstrated by the large drop in global levelised cost of energy (LCOE) over the last years. Figure 1.1 portrays the change of LCOE for different renewable energy resources between the years of 2010 and 2018 [5]. The LCOE of solar photovoltaic, shown in yellow, shows the highest drop compared to other technologies. It decreased from $0.371/kWh in 2010 to $0.085/kWh in 2018, resulting in a 77% decrease over a period of 8 years.

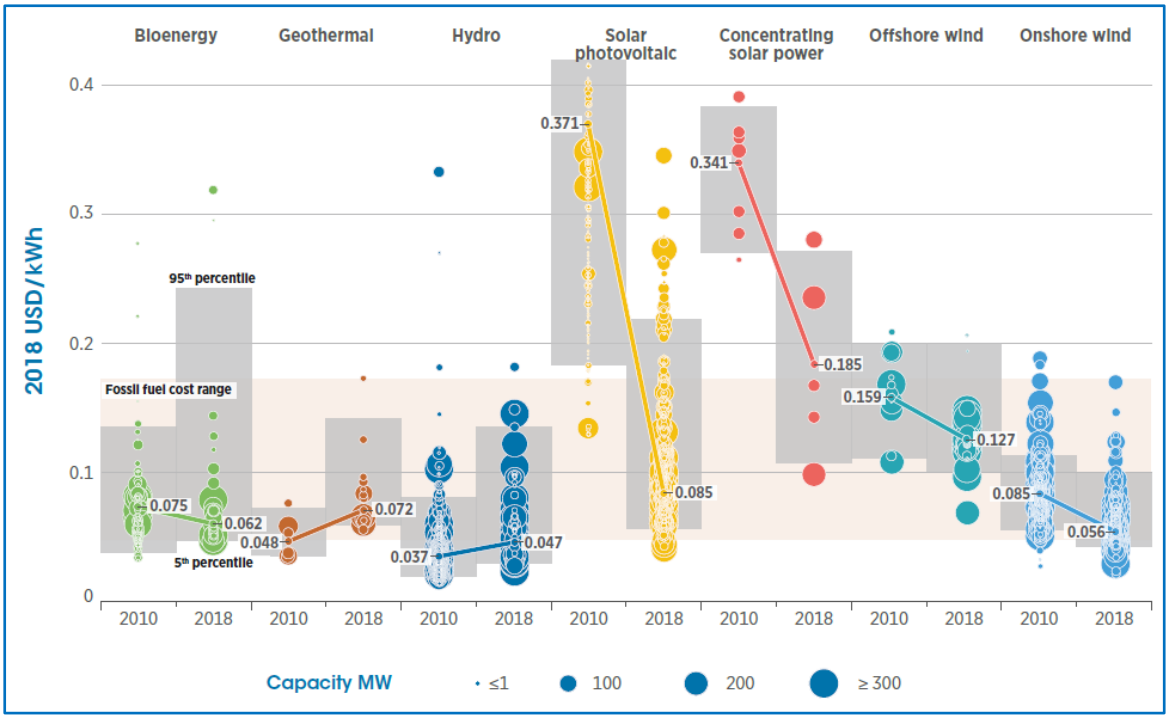

Figure 1.1 Global LCOE of renewable energy generation technologies, 2010-2018 [5].

As a result, the photovoltaic industry has witnessed exponential growth since the beginning of the twenty-first century. Figure 1.2 shows the contribution of energy harvesting technologies to the net global generating capacity added in 2017 [6]. Not only did solar energy account for third of the global generation capacity added, but also it recorded a 30% market growth in 2017.

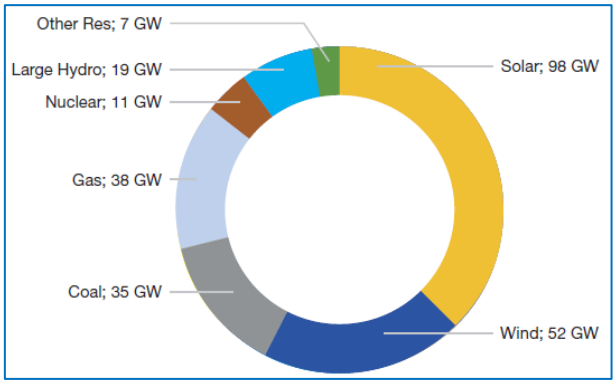

Figure 1.2. Net power generating capacity added in 2017 [6].

With this growing contribution to the energy market, the economic and environmental benefits of this technology are becoming more evident [7]. In addition, governments and industry leaders are allocating investments for research and development in order to enhance the performance and durability of PV modules. Consequently, new promising technologies are emerging, such as bifacial modules, thin-film technologies, and tandem solar cells.

1.2 Tandem Cell Technology

Similar to other energy harvesting technologies, the efficiency of photovoltaic solar cells is limited by several factors. The Shockley-Queisser limit is one of the most recognized attempts to foresee

the maximum possible efficiency of a single junction solar cell [8]. Optical losses, mainly spectral mismatches, are the main factor that delimits the cell's efficiency shown in blue and red in the figure below. Figure 1.3 depicts the three major loss mechanisms for a solar cell [9]. *Thermalization* and *below bandgap* losses are due to a mismatch in energy between the incident photons and the absorber's bandgap. *Other* losses represent mainly the radiative recombination occurring after generating the charge carriers. Tandem cell technology presents a solution to reduce the spectral mismatch losses. This technology, is expected to be commercialized in 2020 [10].

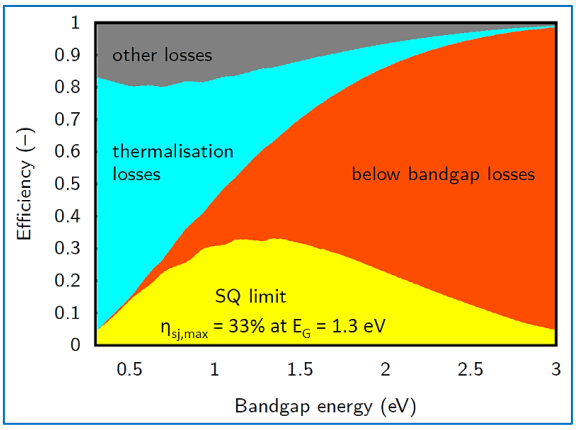

Figure 1.3 The major loss mechanisms for a solar cell under AM 1.5 spectrum [9].

1.2.1 Working principle

A tandem cell is a multi-junction solar cell where absorber layers of considerably different band gaps are combined. The purpose behind this design is to optimize the utilization of incident irradiance by reducing the spectral mismatch losses. The simplest design includes two cells: a top cell with a wide bandgap and a bottom cell with a narrow bandgap. Figure 1.4 shows the basic concept of tandem solar cells [11]. The top cell absorbs the higher energy photons leading to a drop in the thermalization losses. On the other hand, the bottom, cell absorbs the lower energy photons. Under the standard solar spectrum, this technology enables the solar cell to achieve high theoretical limits, reaching 46% for a multijunction cell with two sub-cells and 52% for a multijunction cell with three sub-cells [12].

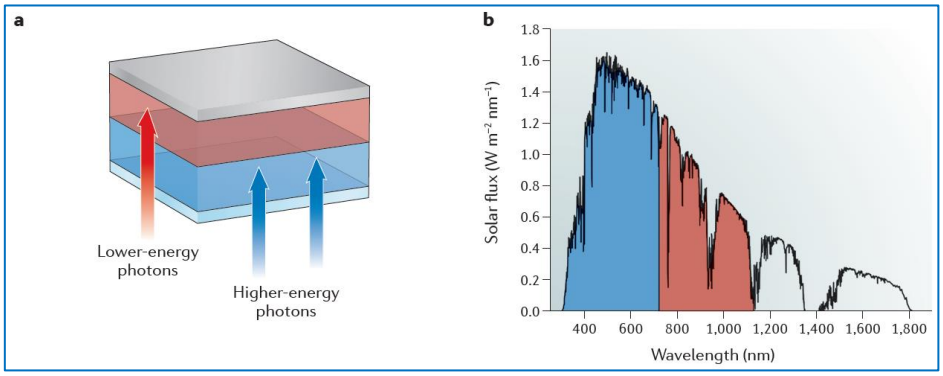

Figure 1.4 Operating principle of tandem cell: a) Tandem cell concept b) Spectral regions for absorbing cells [11].

1.2.2 Cell Configuration

The connection between sub-cells has been also a topic of research. For two sub-cells, the two possible options are two-terminal (2T) and four-terminal (4T) connections. Figure 1.5 depicts the possible configurations for tandem cells with two sub-cells [13].

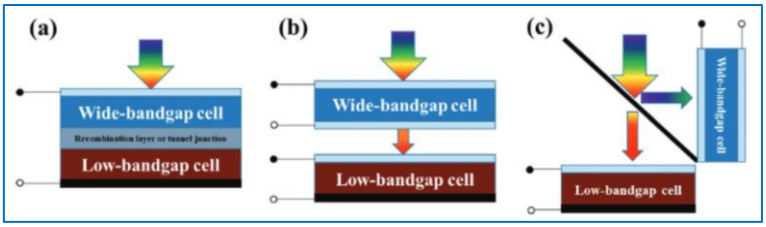

Figure 1.5. Tandem cell configurations: a) 2T b) 4T stacked c) 4T decoupled [13].

4T tandem cells suffer from manufacturing obstacles that hinder their commercialisation. For 4T stacked tandem cells, the four terminals must have specified spectral and optical properties. On the other hand, the design of 4T decoupled tandem cells requires a dichroic mirror, an optical splitter that is very expensive for large scale manufacturing. The performance of 2T tandem cell, the easiest to manufacture and commercialise, can be impeded by current mismatch. The 2T architecture implies that the two sub-cells are connected in series. Thus, the component with the lowest current density will determine the overall current of the cell. To overcome the current mismatch challenge, researches are conducted to optimise the design parameters of monolithic tandem cells [14], [15].

1.2.3 Perovskite Attributes

Perovskite is a material described by the formula ABX_3, where A is a large cation, B is a small cation and X is an anion. Recently, perovskite has become a topic of interest in the photovoltaic industry because of its promising attributes. A key attribute is the strong optical absorption implying a smaller material thickness needed. The possibility of a thin-film application, combined with the low non-radiative recombination, reduces the losses of collecting the photo-generated charge carriers. Besides, the commercialization of large scale photovoltaic applications with perovskite is possible due to the ease of perovskite fabrication and diversity of methods [16]. The mentioned characteristics favour the perovskite as a material used for tandem cell design.

1.3 Energy Yield Prediction

1.3.1 Motivation

Despite the auspicious features of the photovoltaic technology, an undeniable fact is hindering its progress; it is an intermittent source of energy. In fact, the intermittency of power generation creates a substantial challenge for power producers, utility companies and system operators [17]. This section presents three main benefits of developing accurate energy yield prediction models.

At the technical level, fluctuating generation jeopardizes the grid stability and may result in electricity congestion, frequency swings and possible power outages [18], [19]. To avoid the risk of failure, many technical solutions are investigated. These solutions include the integration of storage, or response, systems and applying demand-side management algorithms and policies [20]–

[22]. These solutions present additional, indirect, costs for installing and integrating photovoltaic systems.

The total energy yield is a decisive factor in assessing investments in PV systems. Energy yield uncertainty of PV system have always questioned the credibility of any financial appraisal. Overestimating the energy yield of a prospective project implies overrating the profits of the project and thus may lead to financial losses. On the other hand, underestimating the energy yield would discourage potential investors. For energy trading, this uncertainty in power output results in low capacity credit in the day-ahead markets and reduced utilization of available plants [23]. As the penetration of photovoltaic technology to the power sector increases, the economic and social costs of it intensify [24]. Therefore, from an economic perspective, obtaining an accurate energy yield prediction for PV systems will reduce the effect of intermittency and encourage prospective investors.

At the operational level, the output of a PV system is sensitive to numerous factors, especially for advanced technologies. An accurate model of a PV system can be an indicator of the system's condition and may help in detecting any unusual occurrences.

Therefore, developing prediction models for PV systems is needed to reduce the social, economic, and technical costs of generation uncertainty. These models would pave the way for more convenient decisions on the operational and strategic levels. An efficient forecast of the generated PV power will reduce the technical and economic challenges of integrating photovoltaic energy generation [25].

1.3.2 Energy yield prediction models

The significant growth of the PV technology has motivated the development and continuous refinement of energy yield models. Not only are these tools beneficial for the modelling of energy output, but also they can be used to quantify the impacts of PV system design choices. At the fundamental level, most software packages are based on similar analytical models: an optical model to simulate the incident light interactions, a thermal model to estimate the module's temperature, and an electric model to predict the module's performance under the simulated conditions. Some packages allow the user to benefit from additional features. Below is a list of some of the commercial models with their characteristic features.

SAM (System Advisor Model) is a simulation tool developed by the National Renewable Energy Laboratory (NREL) in the United States of America. Its scope of application extends beyond the photovoltaic technology to include geothermal, wind and biomass power. It involves the power output at an hourly or sub-hourly basis and investigates the effects of uncertainty by stochastic and probability of exceedance analyses. SAM allows the user to model a variety of systems, such as PV with battery storage and high concentration PV. Moreover, SAM is helpful for financial appraisals as it calculates financial metrics that include net energy savings, after-tax present value and payback period [26].

PVsyst is another software package that was developed at the University of Geneva. It focuses on the technical side more than the economic. The software allows the user to define the project by specifying the desired power, PV technology and system location. Besides, it can be utilized to

consider additional issues such as grid storage and system aging [27]. PVsyst has a user-friendly, multilingual interface, and offers the users comprehensive reports and analyses about design aspects [28].

MoBiDiG (Modelling of Bifacial Distributed Gain) is another simulation tool developed in ISC Konstanz that models monofacial and bifacial modules. Similar to the previous tool, it is based on optical, thermal and electrical sub-models. Perez model is used to simulate the irradiance distribution across the sky dome. Moreover, the economic aspect is considered by calculating the LCOE for any given system. This tool achieves a great level of accuracy with a deviation of 4.9% for five extreme-days case [29].

BIGEYE is a computational tool developed by ECN, part of TNO. It is mainly focused on modelling bifcial modules and optimizing the system design. The model requires meteorological data as an input to incident irradiance via three-dimensional view factors and calculate the temperature via thermal model [30]. Then, a single-diode electric model is implemented to simulate the hourly, daily, monthly or yearly energy yield of the system [31]. The BIGEYE model is capable of optimizing the system, or module, design in order to guarantee the highest possible energy output, lowest possible energy cost, or best alignment with the daily demand curve [32].

1.4 PVMD Toolbox version 3

PVMD toolbox is a simulation tool developed by Photovoltaic Materials and Devices (PVMD) group members at Delft University of Technology. In fact, the current model is a result of accumulated effort and work by previous MSc students, Elias Garcia-Goma, Julen Garro Etxebarria and Zidan Wang. The latest version was developed by Zidan Wang in her master's thesis "Improvements and Experimental Validation of the PVMD Toolbox" [33]. The main effort will be on improving version 3 of the PVMD Toolbox, which will be referred to as *Toolbox.*

1.4.1 Toolbox description

At the fundamental level, the toolbox is composed of five main models. The models, programmed on MatLab, run sequentially to simulate the coupled optical, thermal and electrical phenomena. Figure 1.6 shows the logic and flow of data within the toolbox, followed by a brief description of each of the five models.

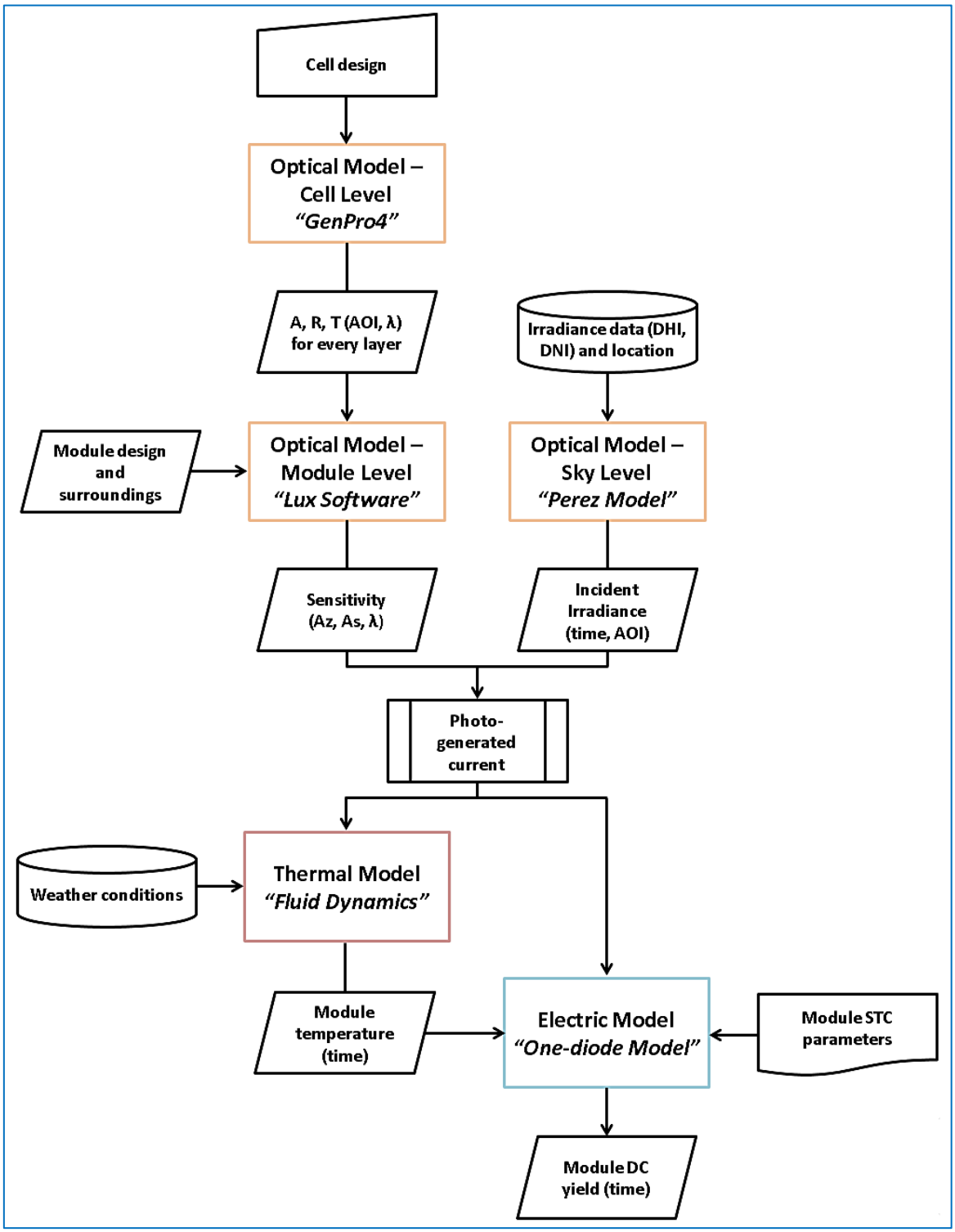

Figure 1.6 Toolbox flowchart with optical, thermal and electric models.

The Optical Models

The *Cell Level Model* studies the light interactions inside the cell. *GenPro4*, a software package developed by Santbergen et al, is integrated into the toolbox. It utilizes ray optics and wave optics to achieve high accuracy at a tolerable computational cost. *GenPro4* models the solar cell layers as 1-D cross-sections and performs simulations in order to calculate external quantum efficiency as a function of wavelength [34]. Within this model,

the available cell technologies for simulation are mono-facial and bifacial crystalline silicon heterojunction (SHJ) as well as perovskite/c-Si tandem cells. The user can modify the cell design by adjusting the geometric properties of the cell layers. The cell characteristics, including layer texture, refractive indices and extinction coefficients are inputted into the model. Then, light interaction simulations are performed for every wavelength and angle of incidence. The output of this model is layer reflection, absorption, and transmission values for every angle of incidence and wavelength.

The *Module Level Model* uses the optical properties of a single cell, output of the previous model, to simulate the performance of the module. The first task executed in this model is constructing the PV module. This can be done by arranging the cells, according to a given configuration, and sealing the module with an encapsulation material and glass layer at the front and back sides. Then, the module is placed on mounting frames on its corners. An additional option of adding reflectors with defined positions and tilt angles is available for users. After the construction of the module, *Lux*, a software developed by Santbergen [35], is integrated. This software performs ray-tracing simulations in order to create sensitivity maps. Sensitivity is defined as the module's utilization of an incident spectrum. Its values range between 0, the case where the module absorbs 0% of the incident light, and 1, the case where the module fully utilizes the incident light. The sensitivity values are wavelength-dependent and can be calculated for the whole module or for individual cells. These values are plotted on a circle representing the position of incident light on the sky dome.

The *Sky Level Model* studies the distribution of incident irradiance across the sky. This model utilizes direct normal irradiance (DNI) and diffuse horizontal irradiance (DHI) available on solar radiation databases such as *Meteonorm*. Then, Perez diffuse irradiance model is applied to simulate the light incident from predefined elements across the sky dome. To convert the irradiance intensity value into a spectrum, air mass (AM) is calculated according to the solar zenith angle. Based on AM value, the solar spectrum is given for the considered time and location. In addition, the impact of shading caused by nearby objects or neighbouring cells is considered according to the principle of horicatcher [36], which corrects incident irradiance based on the skyline of studied location. The output of this sky model is incident spectrum from sky elements for all modelled hours of the year.

The Thermal Model

With the available sensitivity map and sky irradiance from the optical models, the photo-generated current is calculated for the cells. Then, the model takes the photo-generated current, incident irradiance and weather conditions as an input to calculate the temperature. Using fluid dynamics relations, the model calculates the temperature on an hourly basis. Due to the small cross section between the neighbouring cells, thermal conduction between cells is assumed to be negligible. Then, the temperature is calculated for each cell individually. Because the time constant of a module is in the range of 7 minutes [9], steady-state models are used for the thermal calculation.

The Electric Model

In this model, the electric performance of the module is simulated via the one-diode model. Similar to thermal and optical models, individual cells or the whole module can be considered. The model utilizes the calculated temperature and datasheet thermal coefficients to simulate the effect of temperature on the module's performance. Subsequently, based on the photo-generated current and module's properties, hourly I-V curves are created via the diode model. Then, maximum power points are identified, and the DC annual energy yield of the system can be calculated.

1.4.2 Features and limitations

The toolbox offers the user a variety of options for energy yield simulation. Regarding available technologies, the toolbox is capable of simulating the performance of mono facial as well as bifacial SHJ cells. Unlike common commercial software, the toolbox also simulates perovskite/c-Si tandem cells. Besides, the user is able to modify the photovoltaic system design by considering the effects of reflectors and shading caused by neighbouring modules or nearby objects. In addition, the last version models the irradiance distribution across the sky and considers the AM spectra. This had led to an 8.6% accuracy when validating the toolbox outputs.

However, some limitations hinder the performance of the toolbox. The first limitation of the toolbox lies in the electrical model. Although the diode model is capable of effectively stimulating the electric performance, enhancements are needed in order to maintain its accuracy under varying operating conditions. Fill factor is a key element in determining the DC yield of a PV module. It is highly influenced by series resistance, shunt resistance and diode properties [37]. In the latest version, several modifications were implemented to account for temperature's influence on the model's parameters. Yet, the ideality factor, as well as shunt and series resistances, is assumed to be constant. This may have been a source of inaccuracy in the toolbox.

The current version of the toolbox does not fully consider the losses resulting from cell-to-module transition. In fact, the *geometric losses* are accounted for by setting cells spacing and module's borders. In addition, *optical losses*, such as the influence of glass and encapsulant, are calculated via the optical models. However, the toolbox does not take into consideration the influence of solar cells interconnections.

The last limitation of the toolbox is the limited amount of experimental validation. Last year, experimental validation was carried out under standard test conditions and real-life conditions. The validation has resulted in an 8.6% accuracy. However, experimental validation was only implemented on the global level and for a short period of time. In fact, model-level validation can help in assessing individual performance and identifying sources of inaccuracy. In addition, performing further validation will examine the robustness and accuracy of the toolbox under different conditions.

1.5 Thesis objectives

Based on the prior work of students on the PVMD Toolbox, this thesis aims at developing version 4 with additional features and amended performance. Therefore, the main research goal is to implement:

Improvements and Experimental Validation of Energy Yield Modelling for Photovoltaic Systems-

Extending the Energy Yield Prediction Model to Tandem PV Modules

To serve this purpose, the following sub-goals are defined as:

Objective I: Improving the Electric Model

To simulate the electric performance of a solar cell, a one-diode model is implemented. Although the model generates acceptable results, it is desired to improve its accuracy. The effectiveness of this model will be compared with available models in the literature. In addition, the effects of several factors, such as operating temperature and irradiance, on the equivalent circuit parameters will be investigated. This can be done by utilizing the Advanced Semiconductor Analysis (ASA) package, developed at TU Delft. ASA is an optoelectronic simulator that models devices based on amorphous and crystalline semiconductors using one-dimensional semiconductor equations [38]. The program's outputs will be set as a reference to enhance the accuracy of the diode model implemented in the toolbox. Furthermore, cell interconnections are to be taken into account. This can be done by implementing a metallization model. In addition, the influence of cells connections on the module's I-V curve is to be studied.

Objective II: Validating Toolbox Results

After refining the current models and implementing the described modifications, an experimental validation of the toolbox will be conducted. In fact, the validation will not be limited to the predicted energy output of the toolbox. The results and performance of the thermal model will be examined. Consequently, the source of any inaccuracy will be identified and resolved. Besides, this would preclude the possibility of any deviations.

Objective III: Tandem Modules - Case Study

Record efficiencies for tandem solar cells are usually measured at the cell level in a lab under standard test conditions and AM1.5 spectrum. However, the performance of tandem modules is highly sensitive to operating conditions. To demonstrate the capabilities of version 4 of the Toolbox, a case study will be performed to predict the energy yield of tandem modules. The developed electric model, along with the existing optical models, will be used to compare the performance of different design choices.

1.6 Thesis Outline

The thesis report comprises 6 chapters. Below is a brief description of the chapters' contents.

Chapter 2 provides details on the developed electric model at the cell level. Then, based on ASA simulations, the effects of absorbed irradiance and operating temperature on cells' performance are studied. The final result is a *calibrated lumped element model (CLEM)* that can predict I-V curves of a solar cell based on the operating conditions.

Chapter 3 utilizes the developed model in chapter 2 to simulate the electric performance at the module level. First, solar cells' interconnections are studied. Then, a metallization model is implemented. Finally, a cell mapping algorithm, that improves the computation speed, is developed and analysed. The work presented in chapter 2 and 3 serves the first objective by modelling the electric behaviours at the cell and module levels.

Chapter 4 presents the results of toolbox models' validations. The thermal model is improved and validated. Then, the results of electric model simulations are compared with two different datasets.

Chapter 5 applies the models developed in chapters 2 and 3 to perform a case study on the annual energy yield of c-Si/Perovskite tandem modules. A case study is performed to analyse the AEY of different design options.

Chapter 6 includes answers of the research questions and provides suggestions to extend the scope of simulation options

2

Electric Model – Cell Level

This chapter describes the work on improving the electrical model at the cell level. The function of this model is to generate I-V curves for given irradiance level and temperature based on user input. The user input can be I-V curves or input from module datasheet. Section 2.1 presents a brief overview of the lumped element model used, the one-diode model. Section 2.2 includes a brief overview of common parameter extraction techniques in literature. Afterwards, section 2.3 describes the state-of-the-art cells used as model cells for the toolbox simulations. The parameter extraction method based on ASA simulations is explained in section 2.4. Section 2.5 includes a comparison between extraction results and findings from literature. In section 2.6, a method for coupling the effects of irradiance and temperature on the parameters is developed. Section 2.7 presents Lambert-W function, an explicit function that will be used for faster electric simulations. Then, section 2.8 presents the formulation of a *Calibrated Lumped Element Model (CLEM)* and a comparison between the *CLEM* results and simulations performed by ASA. In section 2.9, a parameter extraction method, based on datasheet input, is described. Finally, section 2.10 summarizes the work and results of this chapters and draws out conclusions.

2.1 Overview on the diode models

In the field of photovoltaics, the behaviour of devices and systems is weather-dependent. In other words, the I-V curves of these devices is affected by the incident irradiance and their operating temperature. Therefore, predicting the electric output requires simulations at diverse operating conditions. Two main approaches are used to simulate the behaviour of a system: The physical model and the lumped element method. For photovoltaic simulations, the first approach is based on solving semi-conductor equations in a system of finite elements. Although this method can generate accurate results, it represents a massive computational load if applied for every cell in the PV system over the simulation period timesteps.

On the other hand, the lumped element approach is based on representing the physical phenomena inside the cell by lumped elements. The one and two-diode models are widely used for simulating the photovoltaic behaviour due to their simplicity and capability of generating results with acceptable accuracy. Research was conducted to assess the accuracy and usability of these models as well as simpler models with fewer number of components [39]. However, in this report, the five-parameter one-diode model will be used for solar cell simulations.

Figure 2.1 shows the diode-model equivalent circuit followed by its governing equation (2.1).

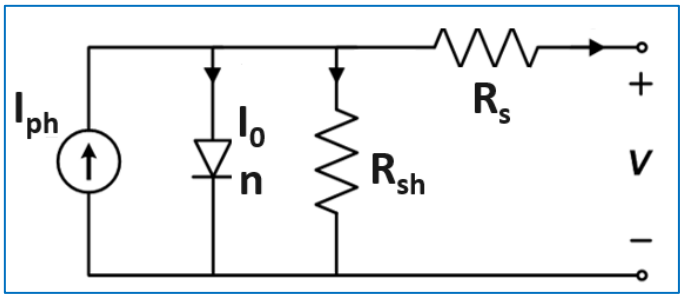

Figure 2.1. The one-diode model equivalent circuit.

$$I = I_{ph} - I_0 \cdot \left\{ exp\left[\frac{q(V + I \cdot R_s)}{n \cdot K_B \cdot T}\right] - 1 \right\} - \frac{V + I \cdot R_s}{R_{sh}} \tag{2.1}$$

The parameters used in the diode equivalent circuit are:

- The photo-generated current (I_{ph}): it quantifies electron-hole pairs generated from absorbed photons as explained in equation 2.2. Its value is used for the ideal current source.

$$I_{ph} = q \cdot A \cdot \int_0^{\infty} EQE(\lambda) \cdot \Phi(\lambda) \cdot d\lambda \tag{2.2}$$

- The ideality factor (n): it is a dimensionless quantity that identifies the dominant recombination mechanism in the solar cell [40]. It is a characteristic of the diode.
- The saturation current (I_0): it is the sum of recombination currents resulting from recombination mechanisms inside the solar cell. It is also a characteristic of the diode.
- The series resistance (R_s): it is the ohmic losses resulting from charge carriers' movement inside the solar cell bulk.
- The shunt resistance (R_{sh}): it quantifies the leakage of the charge carries movement inside the solar cell. There are several factors that impact the value of this quantity. These factors include edge shunts, recombinative crystal defects, scratches and bulk cracks and holes [41].

Each of these five parameters represents a physical phenomenon occurring inside the solar cell. The dynamics and magnitude of these phenomena are highly impacted by the incident irradiance intensity and operating temperature.

2.2 I-V curves and parameter extraction techniques

The solution for equation 2.1 is an I-V, or J-V, curve relating the output current to voltage. Figure 2.2 shows an illuminated J-V curve with its respective P-V curve for a typical solar cell. In addition, the cell's external parameters are labelled.

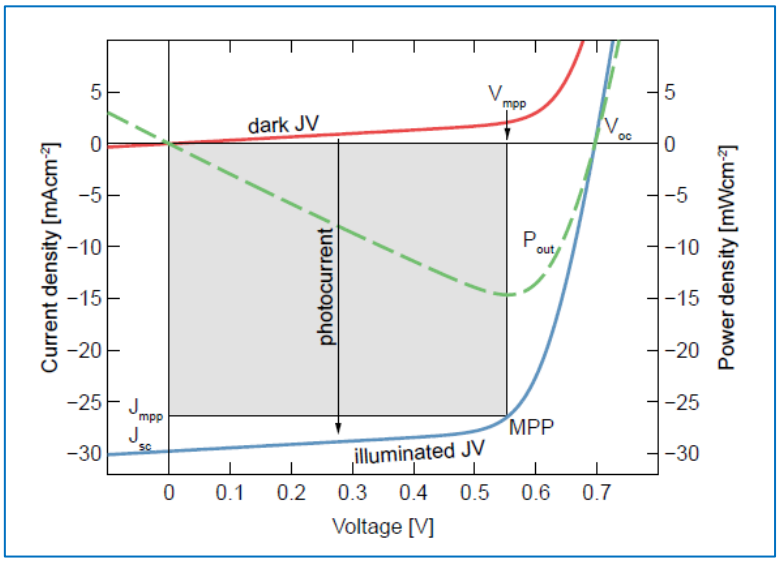

Figure 2.2 Dark and illuminated J-V curves of a typical solar cells with external parameters.

Below are the external parameters:

- V_{OC}: the open-circuit voltage
- J_{SC}: the short-circuit current density
- P_{MAX}: the maximum output power on the J-V curve
- V_{MPP} & J_{MPP}: the voltage and current density at the maximum power point
- FF: the fill factor, a dimensionless parameter that measures the squareness of a J-V curve. It is defined by the following equation:

$$FF = \frac{V_{MPP} \cdot J_{MPP}}{V_{OC} \cdot J_{SC}} \tag{2.3}$$

Despite the convenience of the lumped element model as a performance predictive tool, it suffers from a shortcoming: the parameters, included in equation 2.1, are not easily identified. Therefore, to create a diode model, a reverse process of parameter extraction from simulated or measured I-V curves has to be executed. The extraction can be challenging because the mathematical system is underdetermined. In other words, fitting five parameters from a single curve can result in an infinite set of solutions. Although all the fitted solutions are mathematically valid, only one of them represents the physical parameters of the solar cell [42]. Several techniques were developed to ensure the extraction of the realistic parameters of a solar cell equivalent circuit. These techniques can be categorized into two main types: those using distinctive points on the I-V curve, and others utilizing the whole curve.

Some of the developed techniques for parameter fittings include applying approximations and assumptions to simplify the governing equation over certain regions of the I-V curves. These assumptions are based on previous knowledge of parameters' order of magnitude or physical essence [43]. Other techniques are based on using mathematical tools, such as pade´ approximants and Lambert W-function [44]–[46]. Furthermore, efforts have been exerted to exploit computer algorithms for the parameter fittings. These algorithms include artificial neural networks, harmony search-based algorithms and genetic algorithms [47]–[50].

2.3 Reference Cells

The chosen reference cells for the optical and electric simulations are novel cells with high efficiencies. The model cells are silicon heterojunction and perovskite solar cells. The toolbox can simulate any of the two cells, in addition to tandem cells formed by the model cells. GenPro4 is used to match the cells' designs to obtain comparable optical performance to the reference cells. Afterwards, the cells' electric properties are tuned using ASA to match the I-V curves of the model cells.

2.3.1 Silicon heterojunction cell

The reference cell is the silicon heterojunction fabricated by Kaneka Corporation with an efficiency of 25.1% [51]. This cell consists of an n-type c-Si wafer, with an a-Si:H i/p stack in the front and a-Si:H i/n stack at the back. Moreover, the design includes a transparent conductive oxide front contact and metallic rear contact.

First, the cell layout was tuned to match the optical performance of the model cell using GenPro4. The selected materials for the design cells were chosen based on the layout mentioned in the manufacturer's paper. Then, using n, refractive index, and k, absorption coefficient, datasets available in the PVMD group, a trial and error process was performed to match the GenPro4 simulated EQE with the manufacturer's EQE. The layers' thicknesses were tuned so that the optical performance of the design cell showed a good agreement with the reference cell.

Afterwards, based on the generation profile results from GenPro4, Carlos Ruiz Tobon, a Postdoc in the PVMD group, optimized the electric properties of the cell materials using ASA7. The optimization process included constraints that limit the electric properties within the physical values. Figure 2.3 compares the optical and electric performance of the designed cell to those of the reference cells[52]. Detailed description of the cell design can be found in appendix A.

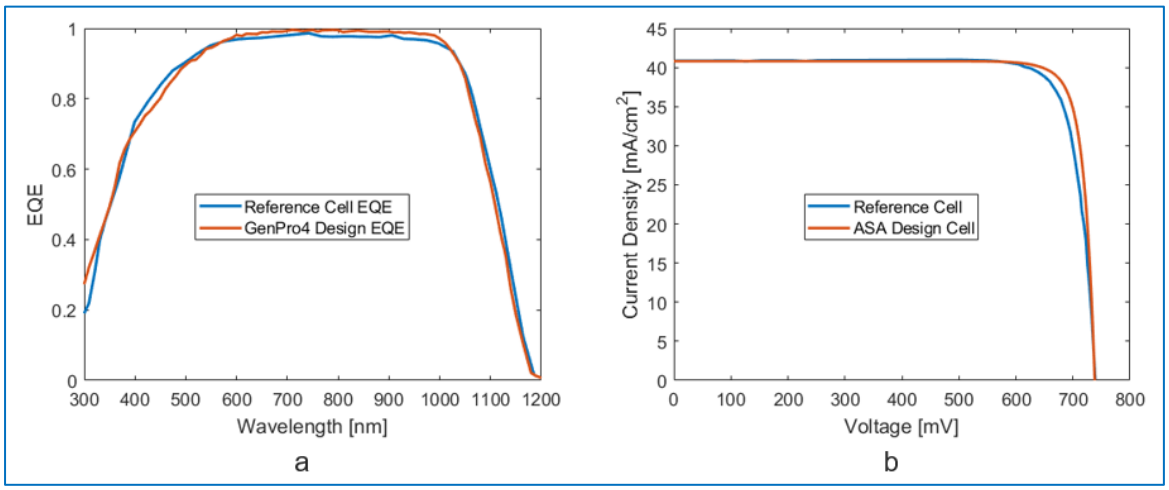

Figure 2.3 Comparison of a) EQE and b) J-V curve between reference cell and designed cell [52].

2.3.2 Perovskite cell

The reference cell is the novel perovskite cell fabricated at KRICT with an efficiency of 22.7% [53]. The cell design includes a perovskite layer with TiO_2 and FTO at the front side and P3HT and a metallic rear contact at the back side. Figure 2.4 compares the optical and electric performance of the designed cell to those of the reference cells [54].

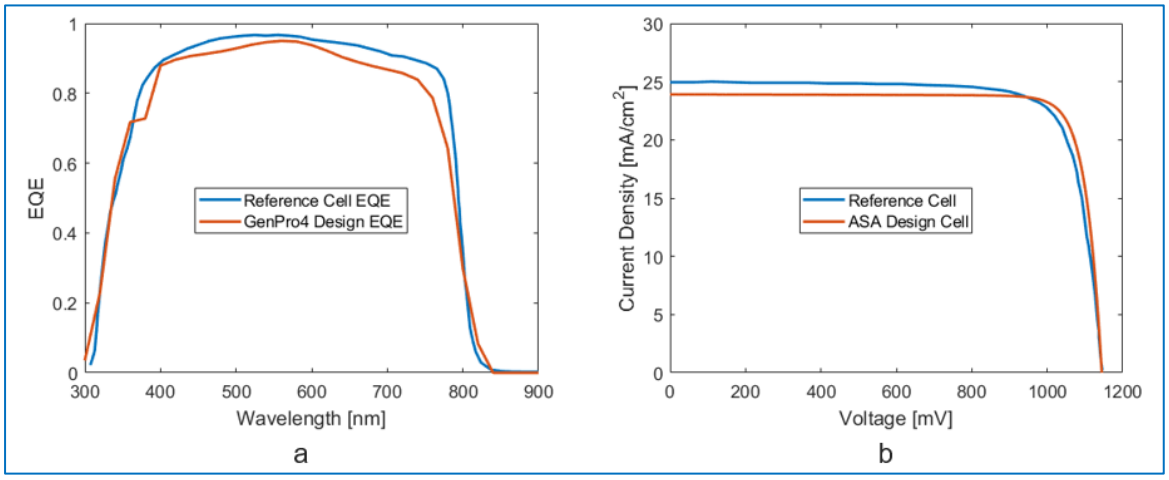

Figure 2.4 Comparison of a) EQE and b) J-V curve between reference cell and designed cell [54].

The same steps taken to tune the SHJ design were used for the design of the perovskite cell. As mentioned in section 1.2.3, perovskite is a material with a general formula of ABX_3, where A, B and X are ions. The ions choice affects the material's optical and electric properties. Therefore, the small difference in optical performance between the design and reference cells can be linked to the difference in n and k values between the PVMD dataset and the material used by the manufacturer. This difference in the EQE resulted in a lower photo-generated current of the design cell when compared to the reference cell. Detailed description of the cell design can be found in appendix A.

2.4 Parameters extraction based on ASA J-V curves

The purpose behind the developed electric model is to combine the benefits of the two modelling approaches: speed and accuracy. The lumped element model is a fast tool for simulating I-V curves. However, the lumped elements are usually considered as constants. As mentioned in section 2.1, these elements represent physical phenomena in the solar cells. The magnitude and dynamics of these phenomena are sensitive to the operating irradiance and temperature.

Based on simulations generated by physical model, ASA, the behaviour of the model parameters is studied. Therefore, it would be possible to express these parameters as functions of irradiance and temperature. Plugging these functions in the lumped element model results in a *calibrated lumped element model (CLEM).* In short, the steps included in this methodology are defined in figure 2.6.

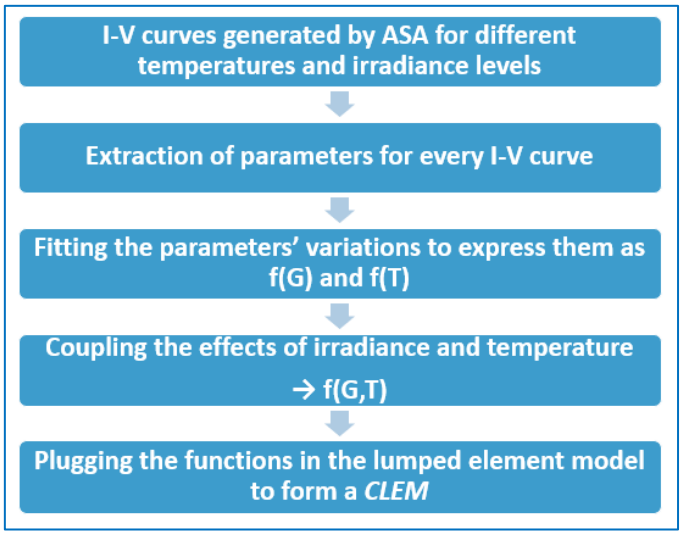

Figure 2.5 Flow chart showing steps needed to form a CLEM.

As mentioned in section 1.5, the ASA package is utilized in order to model the electric performance of the solar cell. As a first step, a series of simulations were performed with only one variable changing, while the other is fixed at the STC value. The purpose behind these simulations is to cover the largest possible set of operating conditions. Thus, 12 simulations were performed with temperature values ranging between 250 and 360 K (-23.15 °C and 87.15 °C) while irradiance is held constant at AM 1.5G. On the other hand, 16 simulations were performed with irradiance ranging between 100 W/m^2 and 1500 W/m^2 under 25 °C temperature. It is important to note that irradiance levels were generated by scaling the AM 1.5 spectrum to avoid any spectral effect. With ASA output being available, the parameters can be extracted and their dependence on irradiance and temperature can be studied. Figure 2.6 shows the generated I-V curves by ASA at different irradiance levels and temperature for the SHJ model cell. The thick plots represent the I-V curves at STC conditions.

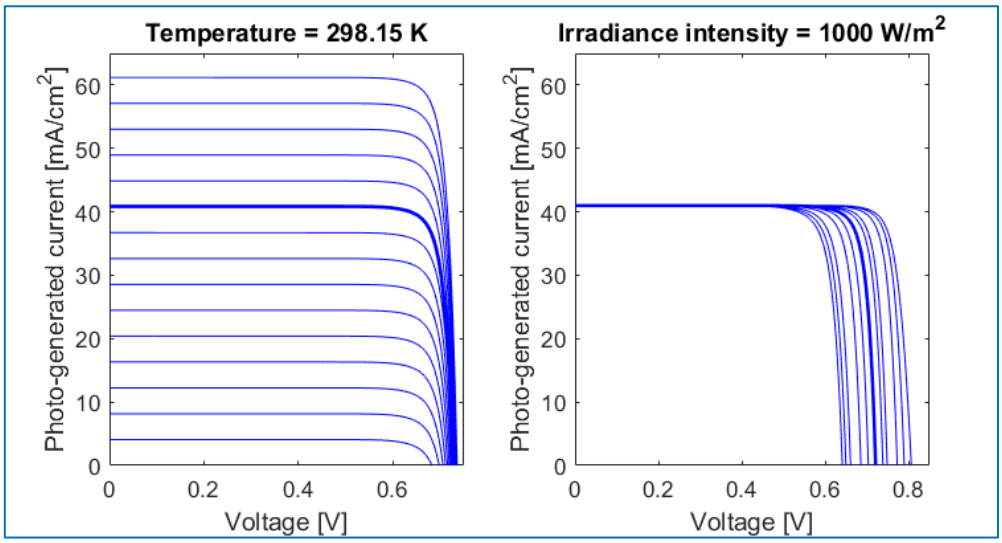

Figure 2.6 ASA I-V curves for different irradiance levels (left) and different temperature levels (right).

2.4.1 Simultaneous approach

The ASA generated J-V curves were imported to MatLab. Then, numerical functions, such as *fmincon* and *fminsearch*, were used to fit simultaneously all the diode model parameters, hence the name *Simultaneous Approach*. Figure 2.5 presents the fitted series resistance values, shown as blue circles, as the irradiance intensity varies; the red line connecting the points is a guide for the eye.

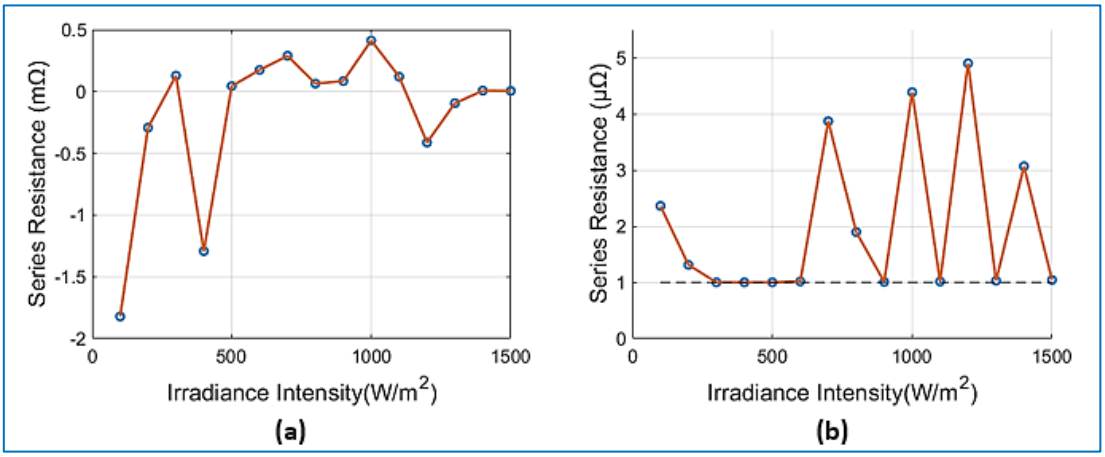

Figure 2.7 Series resistance fitting results using a) unconstrained and b) constrained simultaneous approaches.

Figure 2.2.a shows the results of unconstrained fittings. The parameters are fitted without lower or upper bounds. From this graph, the first flaw of this approach can be recognized: the unrealistic fitting results shown here as negative resistance values. To overcome this issue, constrained fitting was tested. Figure 2.2.b shows the results of this approach. Although this eliminates the unrealistic resistance values, the approach still suffers from the absence of any trend in the fitted results. In addition, the fitted values are highly sensitive to the initial guess. Therefore, a new approach that relies more on the physical significance of the fitted parameters is to be investigated.

2.4.2 Parameter-by-parameter approach

In this approach, the extraction of parameters is done by applying physical knowledge to create valid approximations.

In the short-circuit region, the J-V curve can be approximated as the equation 2.4:

$$J = J_{ph} - \frac{V + J \cdot R_s}{R_{sh}} \tag{2.4}$$

This equation can be reorganized to obtain equation 2.5:

$$J = \frac{J_{ph} \cdot R_{sh} - V}{R_{sh} + R_s} \tag{2.5}$$

Assuming series resistance is negligible when compared to shunt resistance, photo-generated current density can be approximated as short-circuit current density according to the following equation:

$$J_{sc} = J_{ph} \cdot \frac{R_{sh}}{R_{sh} + R_s} \approx J_{ph} \tag{2.6}$$

In addition, the shunt resistance can be approximated using the derivative of the J-V curve in the short-circuit region. This result agrees with observations from the literature [55].

$$\left.\frac{dJ}{dV}\right|_{J \approx J_{sc}} = -\frac{1}{R_{sh} + R_s} \approx -\frac{1}{R_{sh}} \tag{2.7}$$

After calculating the photo-generated current and shunt resistance, the next step is to approximate the ideality factor and saturation current. This procedure is used by Mayer [56] to study the influence of irradiance on ideality factor. First, the lumped model implicit equation is considered at the open circuit point. Assuming large shunt resistance, the resulting equation is shown below.

$$0 = J_{ph} - J_0 \cdot exp\left(\frac{q \cdot V_{oc}}{n \cdot k_B \cdot T}\right) \tag{2.8}$$

Equation 2.8 can be rearranged to express the open circuit voltage as a function of other variables.

$$V_{oc} = \frac{n \cdot k_B \cdot T}{q} \cdot (\ln J_{sc} - \ln J_0) \tag{2.9}$$

Then, using values of V_{oc} and J_{ph} at different irradiance level, the above equation can be used to calculate the ideality factor and saturation current density via equations 2.10 and 2.11

$$n = \frac{q}{k_B \cdot T} \cdot \frac{d\,V_{oc}}{d(\ln J_{sc})} \tag{2.10}$$

$$J_0 = \frac{q}{n(G) \cdot k_B \cdot T} \cdot y \tag{2.11}$$

where y is the intercept of the plot. The method assumes a constant saturation current as irradiance varies; however, the saturation current can vary significantly versus temperature and thus needs to be modelled. Baruch et. al developed an equation that describes the minimum value of a diode's saturation current [57]. The variation of this value is given by the equation 2.12

$$J_0 = \frac{q}{k_B} \cdot \frac{15\,\sigma}{\pi^4} \cdot T^3 \int_u^\infty \frac{x}{e^x - 1} dx \;; u = \frac{E_g}{k_B \cdot T} \tag{2.12}$$

Where σ is Stefan-Boltzmann constant and E_g is the material bandgap. The material bandgap is temperature dependent and can be expressed as a function of temperature via equations 2.13 for c-Si [58]and 2.14 for perovskite [59].

$$E_g(T) = 1.12 - 2.3 \cdot 10^{-4} \cdot (T - 300) \tag{2.13}$$

$$E_g(T) = E_g(T_0) - 4.1376 \cdot 10^{-7} \cdot (T - T_0)^2 \tag{2.14}$$

Equation 2.14 expresses the temperature dependence of perovskite of formula PMMA/$CH_3NH_3PbI_3$. For this model, it is assumed that the perovskite material of the solar cell

follows the same behaviour. The variation of saturation current as a function of temperature is assumed to follow the same trend described in equation 2.12. In other words, the calculated saturation current from irradiance values is assumed to be the saturation current at STC temperature, 298.15 K, then a scaled version of equation 2.12 is used to model the effect of temperature on the saturation current density. After calculating the saturation current density values versus temperature, the variation of ideality factor versus temperature can be calculated using equation 2.9.

Finally, with all parameters available, regression is performed on equation 2.1 to calculate the last parameter, series resistance.

Using this approach, it was possible to estimate the parameters of a solar cell from J-V curves. After the J-V curve fittings were completed, mathematical functions were used to model the behaviour of the diode model parameters as temperature or irradiance intensity varies. Thus, each parameter was expressed as a function of temperature at 1000W/m^2 irradiance intensity and as a function of irradiance intensity at 25 °C. The parameters variations and fitted functions can be found in appendix B.

2.5 Fitting Results and Discussion

After the parameters' extraction and fittings, it is possible to assess the extraction method. Although there are no reference values of the model cells for comparison, the general trends of parameters' behaviour are compared to observations from the literature. For this assessment, the silicon heterojunction cell is used. This is because silicon is a mature technology, with more research conducted and more available material and results than perovskite. Table 2.1 presents the parameter trends resulted from fitting and found in the literature. It is important to note that the order of parameters in this table is the same as the order of their extraction from a J-V curve.

Table 2.1 Parameter behavior from extraction compared to observations from literature.

Parameter	*Irradiance Intensity Effect*		*Temperature Effect*	
	Fitting	*Literature*	*Fitting*	*Literature*
I_{ph}	poly. increase	poly. increase [60]	poly. increase	poly. increase [61]
R_{sh}	exp. decrease	exp. decrease [62]	poly. increase	poly. decrease [61]
R_s	poly. increase	poly. increase [60]	poly. decrease	poly. decrease [63]
n	poly. decrease	decrease [64]	poly. decrease	poly. decrease [61]
I_0	constant	poly. increase [62]	exp. increase	exp. increase [63]

Except for the effect of irradiance on saturation current, the trends of all parameters match the observations from literature. This method calculates the ideality factor based on the values at the open-circuit region. However, it has been proven that the value of ideality factor can vary with the injection level, since the injection level determines the dominant recombination mechanism and thus the value of ideality factor [64]. These are the only limitations in the parameter extraction method described in this section.

2.6 Operating Conditions Coupling

As mentioned in the previous section, using the parameter-by-parameter approach and mathematical fittings, it was possible to express the equivalent circuit parameters as one-dimensional functions of temperature at fixed irradiance or functions of irradiance at fixed temperatures. However, a solar cell is expected to operate in a broad variety of operating conditions. Thus, to guarantee accurate modelling, the irradiance and temperature effects need to be coupled. In fact, equations simulating the effects of irradiance and temperature on open-circuit voltage and short-circuit current are available in the literature. For the short-circuit current, a widely used expression is presented in equation 2.15 [65].

$$I_{SC}(G^*, T^*) = I_{SC}(STC) \cdot \frac{G^*}{G^{STC}} \cdot [1 + k_i \cdot (T^* - T^{STC})] \tag{2.15}$$

Consider the following simplifications:

$$\frac{I_{SC}(G^*)}{I_{SC}(STC)} = \frac{G^*}{G^{STC}} \tag{2.16}$$

$$\frac{I_{SC}(T^*)}{I_{SC}(STC)} = [1 + k_i \cdot (T^* - T^{STC})] \tag{2.17}$$

Plugging in these simplifications in equation 2.15 results in equation 2.18, which can be reduced to equation 2.19:

$$I_{SC}(G^*, T^*) = I_{SC}(STC) \cdot \frac{I_{SC}(G^*)}{I_{SC}(STC)} \cdot \frac{I_{SC}(T^*)}{I_{SC}(STC)} \tag{2.18}$$

$$I_{SC}(G^*, T^*) = \frac{I_{SC}(G^*) \cdot I_{SC}(T^*)}{I_{SC}(STC)} \tag{2.19}$$

Using similar steps, the same result can be obtained for open-circuit voltage. These two quantities can be described as expressions of the diode equivalent-circuit parameters. Therefore, it can be concluded that if this relation is valid for coupling irradiance and temperature effects for V_{OC} and I_{SC}, it can be used for the diode equivalent-circuit parameters. As a conclusion, equation 2.20 was used to couple the effects of irradiance and temperature on the equivalent-circuit parameters.

$$X(G^*, T^*) = \frac{X(G^*) \cdot X(T^*)}{X(STC)} \quad ; \quad X \in \{I_{ph}, I_0, n, R_s, R_{sh}\} \tag{2.20}$$

2.7 Lambert W-function

The governing equation of the diode model (Equation 2.1) is ideal at describing the relation between the cell's voltage and current. However, it is an implicit equation. This results in a limitation of the mentioned equation in terms of deriving relations and computation speed for an energy yield software. Therefore, research was conducted to develop solutions that ease the computation process. These solutions include the Bishop's algorithm [66] and the Lambert W-function [46]. Lambert W-

function is based on the work of Johan Lambert and Leonhard Euler in the mid-late 18th century[67], [68]. It is defined as follows:

$$for\ z = x \cdot e^{x}, \qquad W(z) = x \tag{2.21}$$

For photovoltaic simulations, the explicit equation relating current to voltage is [69]:

$$I = \frac{R_{sh} \cdot (I_0 + I_{ph}) - V}{R_{sh} + R_s} - \frac{n \cdot V_{th}}{R_s} \cdot W(z) \tag{2.22}$$

$$z = \frac{R_{sh} \cdot R_s \cdot I_0}{n \cdot V_{th} \cdot (R_{sh} + R_s)} \cdot exp\left[\frac{R_{sh}}{R_{sh} + R_s} \cdot \frac{R_s \cdot (I_{ph} + I_0) + V}{n \cdot V_{th}}\right] \tag{2.23}$$

The benefits of this function in the field of photovoltaics are plentiful. It can be used to derive explicit expression that relate the diode-model parameters. In addition, it allows a much faster computation speed for solar cell simulation while maintaining high accuracy. Simulations performed on MatLab show that the computation using the Lambert W-function is faster solving the implicit equation, equation 2.1, by an order of 10,000. Therefore, the Lambert-W function will be implemented in the *CLEM* to generate I-V curves based on irradiance and temperature values.

2.8 Accuracy of *CLEM*

The development of the electric model started with 2 simulated datasets using ASA: simulations under varying irradiance with STC temperature, and simulations under STC irradiance with varying temperatures. With the irradiance and temperature effects being modelled and coupled, a *Calibrated Lumped Element Model (CLEM)* can be created. This model employs the diode equivalent circuit to simulate the electric behaviour of the cell. In order to test the accuracy of the fittings and coupling method, equation 2.20, the output of *CLEM* was compared to ASA simulations under operating conditions far from the STC. Two scenarios were considered: low irradiance-low temperature and high irradiance-high temperature. Then, the outcomes of ASA and the *CLEM* were compared. With these scenarios, the parameter extraction and the fittings of their behaviour could be tested. Figures 2.8 and 2.9 present the results of ASA and *CLME* simulations for the mentioned scenarios.

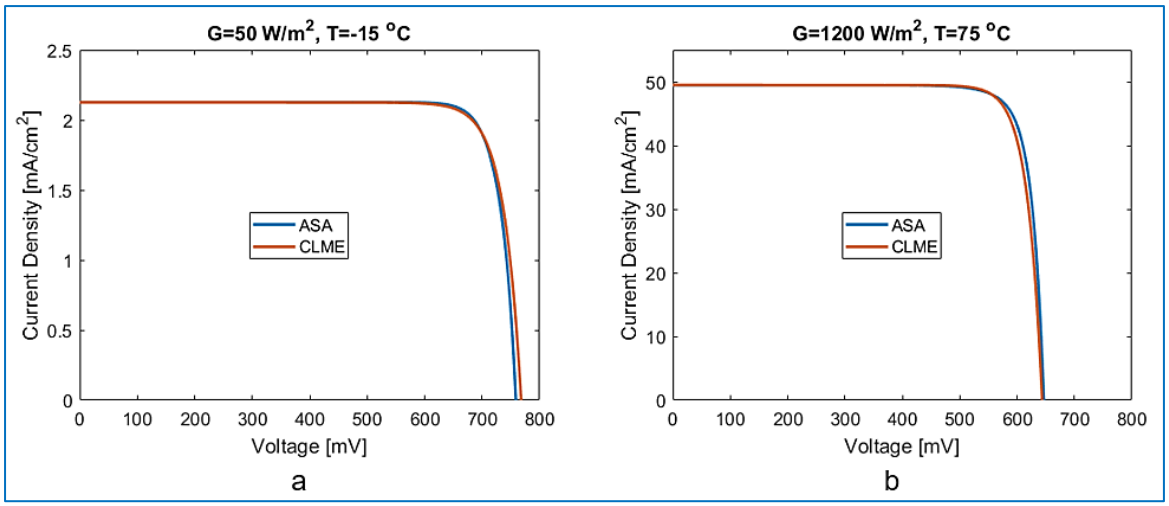

Figure 2.8 The results of ASA and CLEM simulations of the model SHJ for a) low irradiance-low temperature b) high irradiance - high temperature.

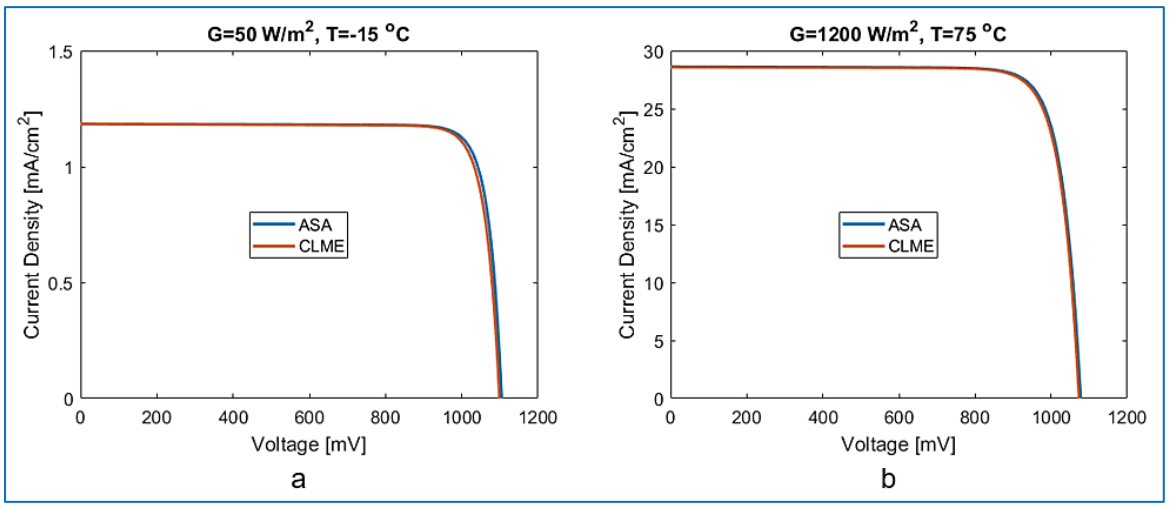

Figure 2.9 The results of ASA and CLEM simulations of the model perovskite cell for a) low irradiance-low temperature b) high irradiance - high temperature.

Table 2.2 presents the percentage errors of *CLEM* simulations for the two scenarios.

Table 2.2 Percentage errors of the *CLEM* under the two scenarios.

	SHJ cell		*Perovskite cell*	
	Low G – Low T	High G – High T	Low G – Low T	High G – High T
P_{MPP}	-0.94%	-0.74%	-1.08%	-0.80%
V_{OC}	1.18%	-0.57%	-0.54%	-0.37%

Therefore, it can be concluded that the *CLEM* can perform electric simulations with a small error margin. In terms of computation speed, the average time required for ASA simulation is one minute. On the other hand, the *CLEM* is capable of performing hundreds of thousands of simulations within a single minute.

2.9 Datasheet Model

Besides using I-V curves from ASA, the toolbox offers the option of energy yield prediction based on input from datasheet. This option allows for more flexibility in the simulation options. However, due to the limited input data, assumptions are needed for the parameters' extraction. This model is based on the user input of the following parameters:

- Maximum power ($P_{Max\text{-}Module}$)
- Open-circuit voltage ($V_{OC\text{-}Module}$)
- Short-circuit current (I_{SC})
- Number of cells (N)
- Maximum power point voltage ($V_{MPP\text{-}Module}$)
- Maximum power point current (I_{MPP})
- Voltage thermal coefficient (K_v)
- Current thermal coefficient (K_i)

The first step for this model is calculating the characteristic quantities per cell:

$$V_{OC-cell} = \frac{V_{OC-Module}}{N_{cells}} \; ; \; P_{MPP-cell} = \frac{P_{MPP-Module}}{N_{cells}} \; ; \; I_{SC-cell} = I_{SC-module} \tag{2.24}$$

Afterwards, the photo-generated current densities, resulting from optical simulations are scaled to match the input's specifications. By performing this step, it is assumed that the simulated cell has the same, yet scaled, spectral response as the model cell.

$$J_{ph-opt} = J_{ph-opt} \cdot \frac{I_{Module-STC}}{J_{model\ cell-STC} \cdot A_{cell}} \tag{2.25}$$

After modifying the optical simulations' results and calculating the cell's parameters, the parameter extraction steps are performed.

Ideally, calculating ideality factor and saturation current values requires a number of open-circuit voltage and short-circuit current values at different irradiance levels. If these inputs are not available, the ideality factor is assumed to be 1 at STC, then the saturation current can be calculated as follows:

$$I_0 = \frac{I_{SC}}{exp\left(\frac{q \cdot V_{oc}}{n \cdot k_B \cdot T}\right)} \tag{2.26}$$

The saturation current is assumed to be constant with irradiance. The effect of irradiance on the ideality factor is modelled as in literature (Table 2.1). Afterwards, the variation of saturation current versus temperature is approximated as in section 2.4.2, using equation 2.12. With the saturation current being available, the variation of ideality factor as a function of voltage can be calculated via equation 2.27.

$$n(T) = \frac{q}{k_B \cdot T} \cdot \frac{V_{oc} \cdot K_V \cdot (T - 298.15)}{\ln\left[\frac{I_{sc} \cdot K_i \cdot (T - 298.15)}{I_0(T)}\right]} \tag{2.27}$$

At STC, shunt resistance can be calculated from the I-V curve using equation 2.7. Then, after calculating all other parameters, the series resistance can be calculated from the implicit equation by on the maximum power point. The effects of irradiance intensity and temperature on the shunt and series resistances are approximated via literature findings presented in table 2.1.

Overall, table 2.3 summarizes the methods for modelling the effects of operating conditions on the one-diode model parameters.

Table 2.3 Summary of assumptions for the datasheet model.

	Irradiance (I_{ph})	*Temperature*
Photo-generated current	Optical simulations	Thermal coefficient
Ideality factor	Literature	Equation 2.27
Shunt resistance	Literature	Literature
Series resistance	Literature	Literature
Saturation current	Constant	Equation 2.12

2.10 Conclusions and recommendations

This chapter describes the improvements made to model the electric performance of PV cells. Two design cells for toolbox simulations were introduced: SHJ by Kaneka with an efficiency of 25.1% and perovskite cell by KRICT with an efficiency of 22.7%.

The parameter-by-parameter approach was successful at extracting the diode model parameters from simulated I-V curves. Based on the coupled effects of irradiance and temperature, a *calibrated lumped element model (CLEM)* was defined in section 2.8. In addition to its computation speed, the *CLEM* simulations proved to be accurate with error percentages limited to 1.18% when compared to ASA simulations. As a conclusion, the work of this chapter serves the first thesis objective by developing a model that simulates the electric performance at the cell level.

Despite the improvements implemented on the cell models, there is still room for improvements. The *CLEM* simulations and *parameter-by-parameter* outputs can be validated against measured values. In addition, more reference cells can be added to the toolbox to offer more simulation options.

3

Electric Model – Module Level

This chapter is a complement to the previous chapter. The models developed and implemented allow the transition of electric simulations from the cell-level to the module-level. Sections 3.1 studies the effect of series-connection among solar cells. In section 3.2, the effects of bypass diode on the I-V curve of the module are modelled. Afterwards, section 3.3 describes an existing model to approximate the metallization losses. In section 3.4, an algorithm to speed up the electric simulations is developed and examined. Section 3.5 summarizes the work presented in this chapter and draws conclusions, followed by recommendations for future work in section 3.6.

3.1 Series-connected cells

In most photovoltaic modules, the solar cells are connected in series to limit the ohmic losses. A drawback of this connection is the possible energy loss if the cells are operating at different conditions. The reason behind this is that the current in a series-connected circuit must be equal for all circuit elements. A fast approximation of the short-circuit current in series-connected solar cells is the minimum value across cells. However, this approach is not accurate, especially if the curve slope is significant due to low shunt resistance.

Because the current is uniform across the cells, it would be more convenient to express cells' voltages as functions of current. Knowing that the voltage is additive in a series-connected circuit, the total voltage of the circuit can be expressed as follows:

$$V_{total}(I) = \sum_{n=1}^{3} V_n(I) \tag{3.1}$$

In addition, the short-circuit current of the branch can be calculated by solving the following equation:

$$V_{total}(I_{sc}) = \sum_{n=1}^{3} V_n(I_{sc}) = 0 \tag{3.2}$$

To demonstrate how the developed model works, an example will be presented. Figure 3.1 shows an equivalent circuit of three series-connected solar cells. Note that the cells' parameters were chosen to clearly demonstrate the effects.

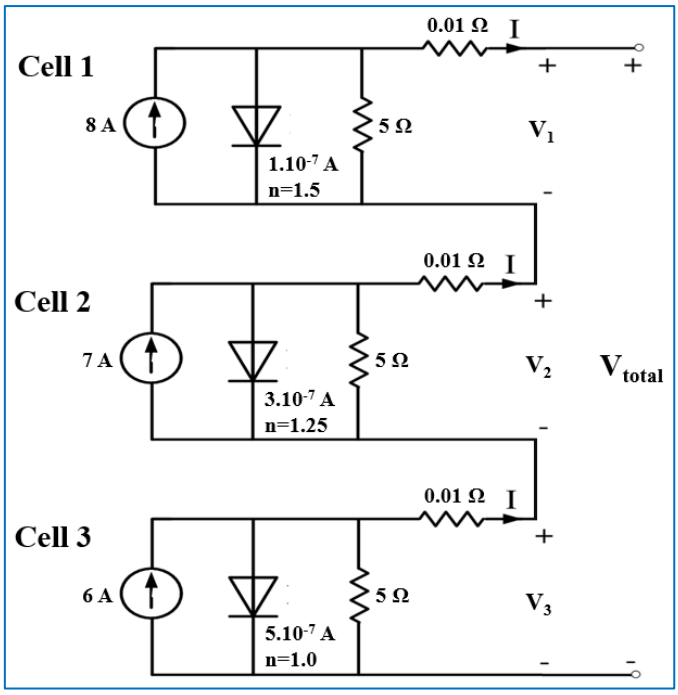

Figure 3.1 The equivalent circuit of three series-connected solar cells.

The output of this approach can be demonstrated in figure 3.2.

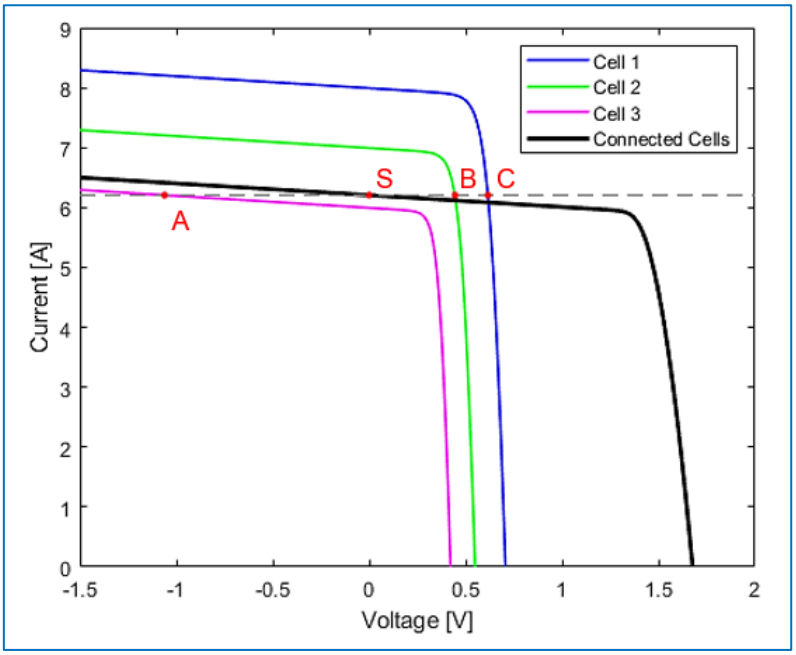

Figure 3.2 The I-V curves of the three cells and of the cell assembly.

Point S, representing the short-circuit point of the branch, is at (6.206, 0). To check the validity of this approach, the summation of three cells' voltages will be calculated:

$$\sum_{n=1}^{3} V_n(6.206) = x_A + x_B + x_C = -1.061 + 0.446 + 0.615 = 0 \qquad (3.3)$$

At the short circuit point of the branch, cell 3 operates in reverse bias whereas cells 1 and 2 operate in forward bias. Therefore, the used equations account for the effects of power dissipation.

3.2 Bypass diode

During the operation of a photovoltaic module, the cells can be shaded because of the surrounding geometry and thus receive dissimilar irradiance intensities. As a result, the current limitation phenomenon explained in the previous section can occur. In addition, the shaded cells would operate in reverse bias, raising their temperature. The creation of these *hotspots* leads to accelerated aging and a higher possibility of unexpected failures or even fire initiation [70]. To avoid these risks, bypass diodes can be installed in the module. These electronic elements allow the current to bypass in a parallel branch, limiting the power dissipation. These elements can dissipate a small quantity of power due to their forward voltage. Figure 3.3 shows the forward voltage as a function of the bypass current at different operating temperatures [71]. This graph is for SM74611 *smart bypass diode*, manufactured by Texas Instruments.

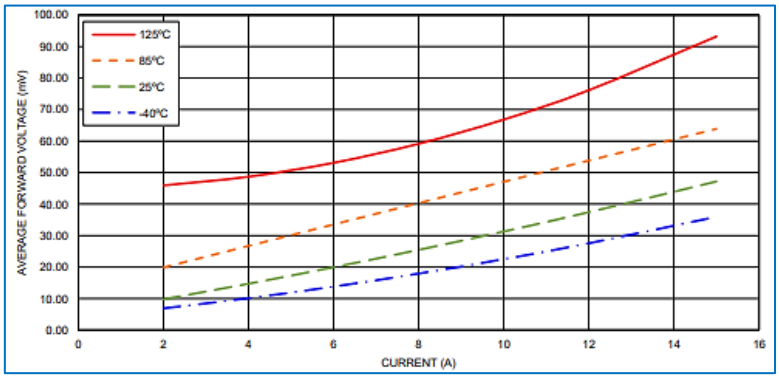

Figure 3.3 Forward voltage vs. current at different temperatures for SM74611 bypass diode [71].

To model the effect of the bypass diode on Equation 3.4:

$$V_{total}\,(I) = \sum_{n=1}^{n} \{\max[V_n(I), 0] - VBY_n\} \tag{3.4}$$

The first term in the summation limits the minimum voltage of all cells to zeros in order to cancel the effects of power dissipation. The second term, VBY, is the forward voltage function of the bypass diode, defined as following:

$$VBY_n = f(Isc_{max} - Isc_n, T) \tag{3.5}$$

Figure 3.4 shows the equivalent circuit of three series-connected solar cells. This circuit will be used to demonstrate the output of equations 3.4 and 3.5 and generated I-V curves shown in figure 3.5.

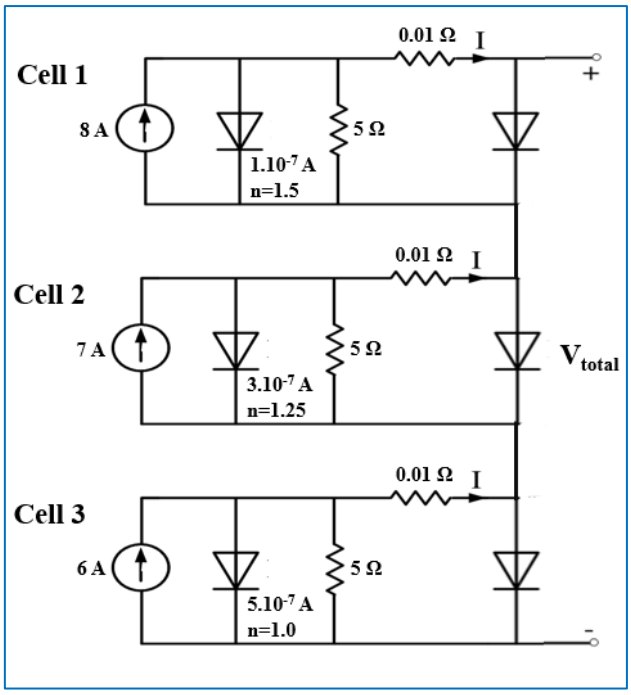

Figure 3.4 Equivalent circuit of three series-connected cells with bypass diodes.

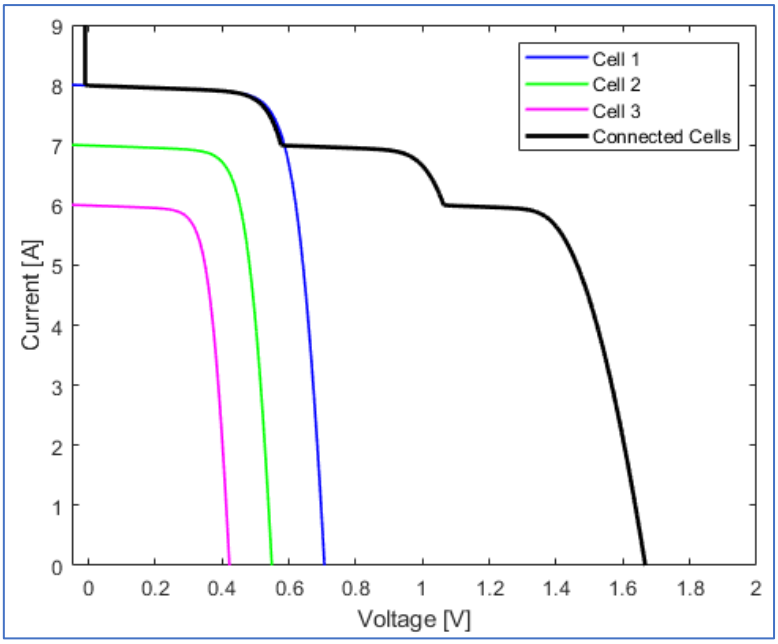

Figure 3.5 I-V curves of the three cells and of the cell assembly.

In the previous example, a bypass diode was connected to every cell in the equivalent circuit. However, for most photovoltaic modules, a bypass diode is connected to a branch of series-connected cells. Therefore, for the module electric simulations, branches of series-connected cells are modelled via equation 3.1. Then, the effects of bypass diodes are considered on the modelled branches. The toolbox offers the user the choice of choosing 0, 3 or 6 bypass diodes for a single module.

3.3 Metallization effects

Connecting the solar cells inside a module is usually done via metallization grids. The research on optimizing losses from metallization has resulted in many metallization layouts. Nevertheless, for this version of the toolbox, front metal contact with *antenna* layout is considered. The implemented model has been developed by a master's student in the PVMD group at Delft University of Technology [72]. Therefore, for detailed derivations and assumptions used, the mentioned reference can be reviewed.

3.3.1 Metallization model

The first step for modelling the metallization effects is dividing the solar cell into a number of unit cells for optical and electrical analysis. The division of the solar cell assures symmetry and ease the calculations. Equations 3.6 and 3.7 describe the number and dimensions of the unit cells, followed by figure 3.6 demonstrating the division of the solar cell into unit cells.

$$N_{unit\ cells} = {N_{busbars}}^2 \tag{3.6}$$

$$L_{unit\ cell} = \frac{L_{solar\ cell}}{N_{busbars}} \tag{3.7}$$

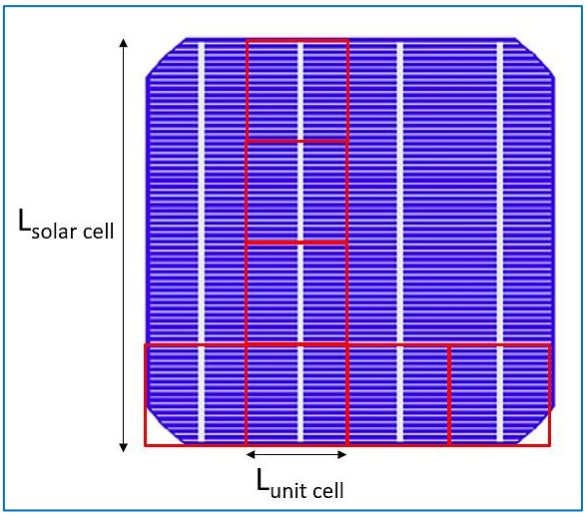

Figure 3.6 Division of a solar cell into unit cells.

Table 2.4 presents the geometric and electric parameters used for deriving the metallization losses.

Table 3.1 Parameter definition of the metallization grid.

Quantity	*Symbol*	*Unit*
Number of finger rows	n_f	-
Number of current extraction points	n_s	-
Finger length	l_f	m
Finger width	W_f	m
Half finger pitch	D	m
Half finger spacing	S	m
Half current extraction distance	H	m

Busbar length	$L_{unit\ cell}$	m
Busbar width	W_b	m
ITO thickness	t_{ITO}	m
Finger thickness	t_f	m
Busbar thickness	t_b	m
ITO resistivity	ρ_{ITO}	Ωm
Finger resistivity	ρ_f	Ωm
Busbar resistivity	ρ_b	Ωm
Contact resistivity	r_c	Ωm^2
ITO sheet resistance	$R\square_{ITO}$	Ω/□
Finger sheet resistance	$R\square_f$	Ω/□
Busbar sheet resistance	$R\square_b$	Ω/□

The shading factor resulting from the metallization grid is shown in equation 3.8. It is a ratio of the area covered by fingers and busbars to the unit cell area.

$$Shading\ factor = \frac{W_f \cdot l_f + D \cdot W_b}{2 \cdot n_f \cdot D^2} \tag{3.8}$$

In addition to the optical losses, metallization results in ohmic losses. The developed model considers four main components for the electric resistance: ITO, finger, contact and busbar. Equation 3.9 shows the total resistance in the unit cell. The contributions of the mentioned componentes are shown successively in the equation.

$$R_T = \frac{1}{12} \cdot \frac{R\square_{ITO} \cdot S}{n_f \cdot l_f} + \frac{1}{6} \cdot \frac{R\square_f \cdot l_f}{n_f \cdot W_f} + \frac{R\square_{ITO} \cdot L_t}{4 \cdot n_f \cdot l_f} \cdot \coth\left(\frac{W_f}{2 \cdot L \cdot t}\right) + \frac{1}{6} \cdot \frac{R\square_b \cdot H}{n_s \cdot W_b} \tag{3.9}$$

3.3.2 Implementing the model

So far, equations 3.8 and 3.9 quantify the effects of metallization on the unit cell. In this sec

Due to symmetry, the shading factor of the solar cell is equal to the shading factor of the unit cell. Therefore, effect of shading can be modelled as follows

$$J_{ph-cell} = J_{ph-optical} \cdot (1 - SF) \tag{3.10}$$

The unit cells are connected in parallel. This can be verified by the fact that the current of the solar cell is equal to the summation of the unit cells' currents whereas the voltage of the solar cell is equal to that of the unit cells. As a result, the modelled resistances of unit cells are connected in parallel as well. Thus, the metallization resistance for the solar cell can be expressed via equation 3.11.

$$R_{solar\ cell} = \frac{R_{unit\ cell}}{N_{unit\ cells}} \tag{3.11}$$

The modelled cell voltage, via *CLEM*, is corrected in equation 3.12.

$$V(I) = V(I) \cdot [1 - I \cdot R] \tag{3.12}$$

3.4 Cell Mapping

Due to the number of sub models and factors in the electric model, the electric simulation required for energy yield can be slow. The implementation of Lambert W-function reduces, to a large extent, the time needed for cell-level simulations. However, with the large number of simulations and interpolations required, the toolbox may remain slow. In fact, the total number of simulations for a 60-cell SHJ module for an annual energy yield calculation exceeds 270,000. Moreover, this number can drastically increase for different modelling scenarios, such as tandem modules or energy yield simulation of a PV array.

3.4.1 Operating conditions bins

The energy yield prediction requires electric simulations of solar cells at various operating conditions. Figure 2.14 depicts the frequency of operating conditions occurrence with bins of 4 A/m^2 and 1 °C.

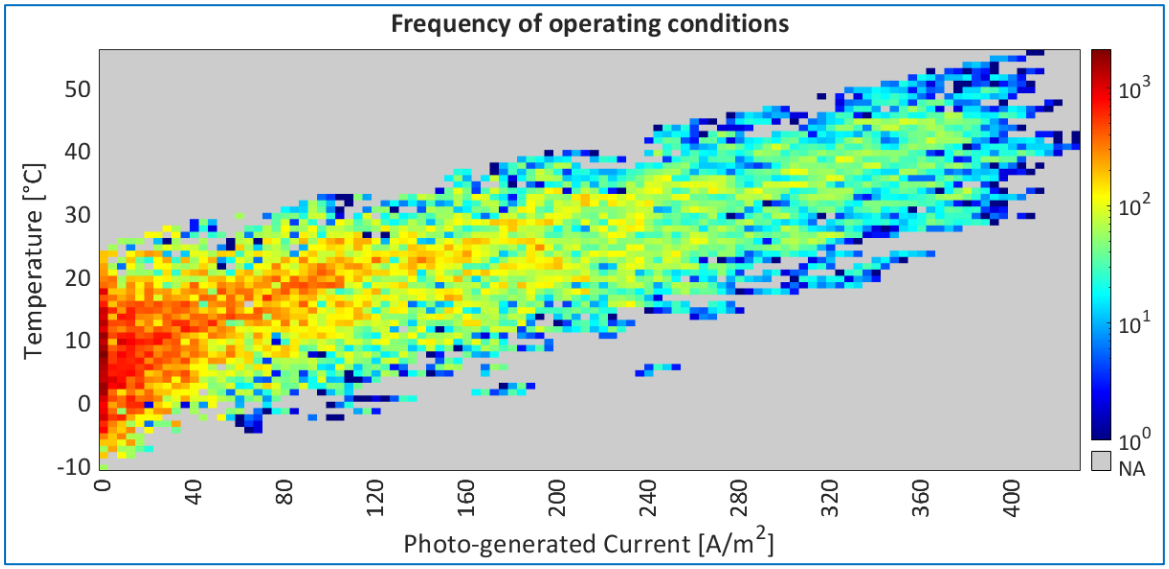

Figure 3.7 Frequency of cell operating conditions with bins of 4 A/m^2 and 1 °C.

From the figure, a positive relation between the photo-generated current and temperature can be noticed. This can be expected because a higher photo-generated current implies higher incident irradiance and therefore higher cell temperature. Another observation is that some bins represent the operating conditions of more than a thousand cells. In fact, the number of colored bins is 2683, compared to 270,000 combinations of operating conditions. Therefore, there could be a room for reducing the number of required simulations for AEY by representing the output of solar cells by the outputs of bins.

The suggested algorithm for reducing the computation speed is called *Cell Mapping*. This algorithm is based on three main steps:

1. The operating conditions of each solar cell for every time step is mapped into bins. Therefore, only the bins representing solar cells are considered rather than considering every possible bin.

2. Simulating the I-V curves for the representative bins using *CLEM*, developed in chapter 2.
3. The I-V curve of each solar cell is assumed to be identical to that of the cell's representing bin.

3.4.2 Bin size analysis

The drop of simulations number is accompanied by inaccuracies. Figure 3.8 Shows a schematic of a bin representing 5 cells, plotted a *x*. The I-V curves of each of the 5 solar cells will be represented by an I-V curve generated based on the bin's center. Simulation errors are expected due to this approximation. The four corners of the bin are the furthest from the center. Therefore, the largest possible error due to this algorithm is expected when a cell lies on one of the four corners.

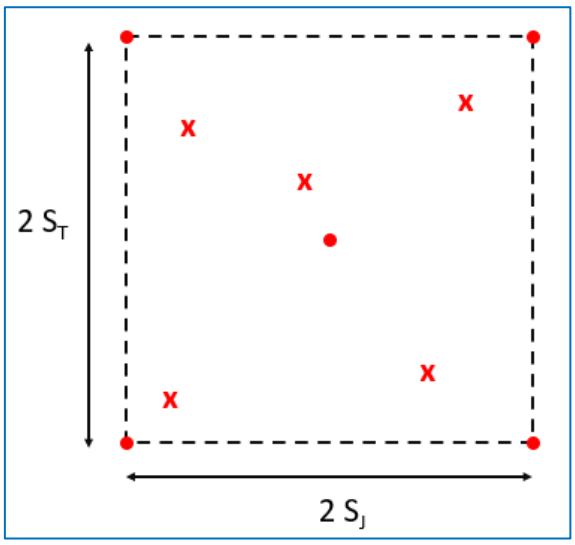

Figure 3.8 Schematic of a bin representing 5 cells.

For simplicity, the effects of photo-generated current and temperature on the cell's power is assumed to be linear. Table 3.2 presents symbols used for bin size analysis.

Table 3.2 Symbols used for bin size analysis

Symbol	*Quantity*
R_J	Range of photo-generated current [0, 460] A/m^2
R_T	Range of operating temperature [-10, 60] °C
K_J	Derivative of power over photo-generated current
K_T	Derivative of power over temperature
S_J	Half the bin's dimension (photo-generated current)
S_T	Half the bin's dimension (temperature

The sizing of the bins affects the computation gain and the resulting inaccuracy of the mapping algorithm. Assuming the effects of photo-generated current and temperature can be coupled similar

to equation 2.20, the maximum possible error, represented in figure 3.8, can be expressed in equation 3.13.

$$Error = P \cdot \left(1 + K_J \cdot S_J\right) \cdot (1 + K_T \cdot S_T) - P = P \cdot \left[K_J \cdot S_J + K_T \cdot S_T + K_J \cdot S_J \cdot K_T \cdot S_T\right] \tag{3.13}$$

Where P is the power generated at the center of the bin. In addition, the sizing can affect the number of available bins and thus the number of simulations required. Equation 3.14 expresses the number of available bins.

$$N_{bins} = \frac{R_J \cdot R_T}{S_J \cdot S_T} \tag{3.14}$$

From equations 3.13 and 3.14, it can be concluded that there is a trade-off between the mapping errors and the computation gain. Therefore, an optimization can be performed to enhance the mapping results, the smallest possible mapping error with the largest possible mapping gain. For this optimization, two variables are defined: the bin aspect ratio and the bin size.

3.4.2.1 Aspect ratio of the bin

The aspect ratio of the bin is defined as the ratio of the bin's dimensions. Based on equations 3.13 and 3.14, the mapping error can vary even if the number of available bins is constant. Therefore, the purpose of optimizing the aspect ratio is to guarantee the smallest possible error for a fixed number of bins.

From equation 3.14, it can be inferred that a fixed number of bins results in a fixed bin area *A*. Therefore, for a fixed number of bins, the bin's dimensions can be related via equation 3.15.

$$S_J = \frac{A}{S_T} \tag{3.15}$$

Substituting this expression in equation 3.13 results in the following equation.

$$Error = P \cdot \left[K_J \cdot \frac{A}{S_T} + K_T \cdot S_T + A \cdot K_J \cdot K_T\right] \tag{3.16}$$

In order to minimize the error, a derivative of its expression is derived then set to be zero.

$$\frac{d\ Error}{d\ S_T} = P \cdot \left[-\frac{K_J \cdot A}{{S_T}^2} + K_T\right] = 0 \tag{3.17}$$

$$-\frac{K_J \cdot A}{{S_T}^2} + K_T = 0 \ \rightarrow \ \frac{A}{{S_T}^2} = \frac{K_T}{K_J} \rightarrow \ \frac{A}{{S_T}^2} = \frac{K_T}{K_J} \rightarrow \frac{S_J}{S_T} = \frac{K_T}{K_J} \tag{3.18}$$

Therefore, for the least mapping error with a constant number of bins, an expression is calculated for the optimal aspect ratio. For the Kaneka model cell, this aspect ratio is equal to the following:

$$\frac{S_J}{S_T} = \frac{1.333\ A/m^2}{1°\mathrm{C}} \tag{3.19}$$

3.4.2.2 Bin size

After calculating the optimal aspect ratio, bin sizing can be directly related to the maximum mapping error. Figure 3.9 shows the effects of bin size on the computation gain and the mapping error of a solar cell.

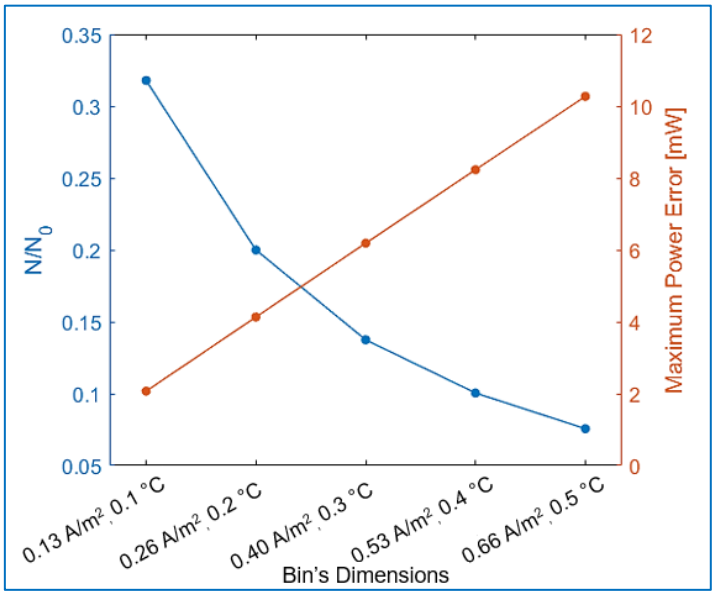

Figure 3.9 Computational gain(N/N_0) and maximum mapping error for different bin dimensions.

The computation gain (N/N_0) is defined as the ratio of the number of bins' simulations to the number of solar cells' simulations. The maximum power error is calculated based on equation 3.13 for a model solar cell with the conventional area. The tradeoff between the computation gain and the mapping error can be observed from the graph. For the toolbox simulations, the chosen bin's dimensions are 0.40 A/m^2 and 0.3 °C.

3.4.3 Mapping results

After defining the mapping steps and the bins' dimensions, the effect of this algorithm is assessed. The assessment is done by comparing the outputs of AEY simulations before and after implementing this algorithm. Figure 3.10 depicts the hourly yield differences between the simulations with mapping and without mapping for a 60-cell module.

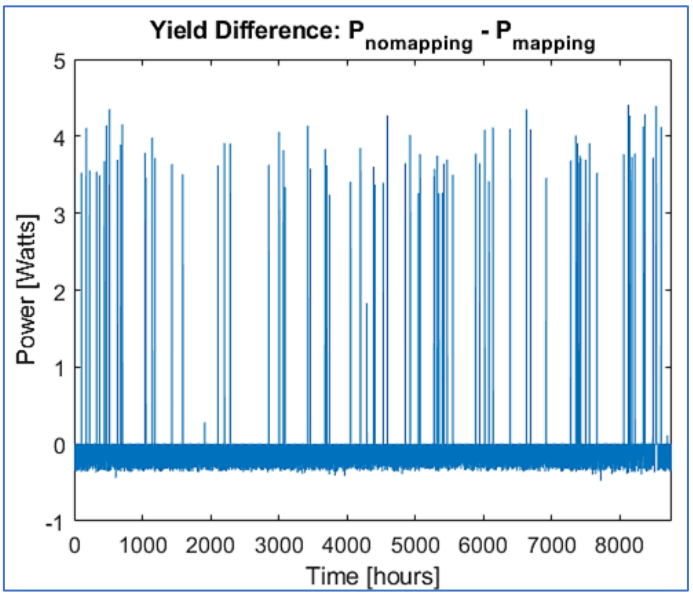

Figure 3.10 Hourly yield differences between the simulations without and with mapping algorithm.

Two types of errors can be observed in the figure above: a random error and a systematic error. For most timesteps, the mapping algorithm slightly overestimates the module's yield. This can be related to the representation of cells with bins. The slight differences in photo-generated current values among the cells, resulting in small quantities of dissipated power, are neglected because of this representation. Due to this error, the mapping algorithm results in an overestimation of energy yield by 0.226%.

Knowing that the module's STC power output is 340 Watts, the highest recorded hourly error is 1.24%. On the other hand, the number of simulations at the cell level is reduced by 86%. This results in a faster AEY simulation by a factor of 5. In fact, compared to version 3, the electric simulation time for AEY for a 60-cell SHJ module has dropped from 1.5 hours to less than 2 minutes (4 CPUs, 3 GHz, 8 GB RAM). Using this algorithm, it would be to quickly simulate the output of larger modules, such as 72-cell modules or 144-half-cell modules.

3.5 Conclusions

The objective of this chapter was to develop a model that simulates the electric performance at the module level. The effects of cells interconnections were modelled and implemented. In addition, a cell mapping algorithm was developed to enhance the computation speed of the electric model. It is based one representing the solar cells by bins to decrease the number of required simulations. Afterwards, the bin's aspect ratio and size were optimized to guarantee the minimum mapping error for a fixed number of simulations. The algorithm was then assessed to examine its effects on accuracy and computation gain. For a bin size of 0.4 A/m^2 and 0.3 °C, the number of required simulations dropped by 86%, with an energy yield error of 0.226%.

In short, the work in this chapter present a great improvement to the toolbox. In addition, the electric simulation time dropped by a factor of 45, compared to version 3.

3.6 Recommendations

In this chapter, an existing model was implemented to simulate the optical and electric effects of metallization. However, this model is only valid for FBC, antenna layout. Therefore, the metallization model can be modified to include other FBC layouts as well as IBC metallization. In addition, the model can be improved by accounting for temperature and injection level effects on the metallization losses. The metallization models are valid to simulate the connection among solar cells based on crystalline silicon technology. It is recommended to develop a model that accounts for interconnection among laser scribed thin film solar cells.

The current electric model assumes series connection among solar cells in the module. However, new module designs, such as half-cell modules and smart modules, guarantee better performance and higher resilience against varying operating conditions. Therefore, it is suggested to improve the current model in order to simulate the performance of new module designs.

4

Model Validation

In this chapter, the performance of the thermal and electric models in the toolbox are analysed and validated against real-life measurements. Section 4.1 describes the validation methodology and statistical indicators used. In section 4.2, various GHI decomposition models are introduced and their suitability for the Dutch climate is checked. After choosing the GHI decomposition technique, the thermal model is validated in section 4.3 The thermal model is adjusted to include the dynamic thermal behaviour and thereby demonstrating minimize lower differences with measurements at higher temperatures. Afterwards, section 4.4 describes the validation of the electric model against measurements recorded at TU Delft. In the following section, the model is validated again against a dataset from NREL. The validation results are summarized, and conclusions are drawn in section 4.6, followed by recommendations for future work in section 4.7.

4.1 Validation Methodology and Criteria

Due to the lack of access to laboratories in the COVID-19 situation, it was not possible to carry out new measurements for data validation. Thus, existing recorded measurements were used to validate the toolbox models. In this section, the validation methodology will be explained. In addition, the statistical indicators used to assess the toolbox models will be described.

4.1.1 Measured Data at TU Delft

This data was provided by Hesan Ziar, an assistant professor in the PVMD group. Electric and temperature measurements were conducted on an in-house module in the monitoring station at Delft University of Technology. This module consists of 16 5 inch, series-connected MAXEON GEN II solar cells [73]. Wind speed, ambient temperature and GHI were recorded every 10 minutes. In addition, the DC power output and maximum power voltage and current values were recorded every minute. The data was recorded between 25 July and 9 October 2019. The available data is used to validate the outputs of the thermal and electric models in the toolbox. However, the optical model takes DHI and DNI, rather than GHI, as inputs. Therefore, the validation requires investigating GHI decomposition models in order to run the optical model in the toolbox. Figure 4.1 shows the measured I-V curve of the in-house module at STC.

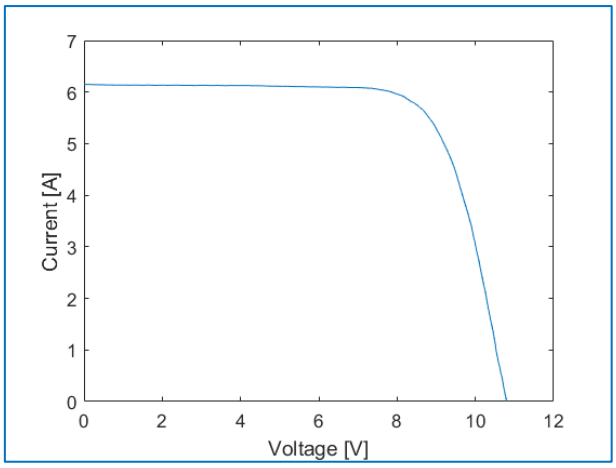

Figure 4.1 Measured I-V curve at STC of the in-house module.

4.1.2 NREL Data

This dataset was provided by NREL upon request. In includes measurements of irradiance, temperature, and electric parameters. For this validation, there is no need for GHI decomposition as DHI and DNI were recorded at each timestep. The measurements were recorded for a 72-cell HIT module deployed in Cocoa, Florida during the period of January 2011 till March 2012 [74].

4.1.3 Statistical Indicators

The purpose of data validation is to assess the quality of models in predicting the output. This is possible by comparing the modelled data to measured data of the real system at the same weather conditions. In order to document the quality of the modelled data, and therefore of the model itself, statistical indicators are used to assess the performance of the models for an adequate period of time. For this validation, three indicators of deviation and one indicator of overall performance of the model. These indicators are used to assess the thermal and electric models in the toolbox [75]. In addition, the indicators are used to determine the best GHI decomposition technique. Note that the measured data points are denoted by *m* and the modelled, or predicted, values are denoted by *p*.

Root mean square difference (RMSD)

It quantifies the scattering of modelled data points with respect to the measured values.

$$RMSD = \sqrt{\frac{\sum_1^N (m_i - p_i)^2}{N}} \tag{4.1}$$

Mean bias difference (MBD)

It is used to study the average bias of the model outputs compared to measurements. Negative MBD value indicates an underestimation of the simulated values and vice versa.

$$MBD = \frac{\sum_1^N (m_i - p_i)}{N} \tag{4.2}$$

Slope of best-line fit (SBF)

It is the slope of regression line that describe the variation of the modelled output versus the measured values. An SBF value close to one indicates an agreement between the modelled and measured outputs.

$$SBF = \frac{\sum_1^N [(m_i - \bar{m}) \cdot (p_i - \bar{p})]}{\sum_1^N (m_i - \bar{m})^2} \tag{4.3}$$

Willmott's index of agreement (WIA)

It is an index developed by Willmott in 1981 to assess the overall accuracy of a model [76]. This index values varies between 0 for complete disagreement and 1 for perfect agreement.

$$WIA = 1 - \frac{\sum_1^N (m_i - p_i)^2}{\sum_1^N (|p_i - \bar{m}| + |m_i - \bar{m}|)^2} \tag{4.4}$$

From the definition above, it can be inferred that the smaller the fraction the more accurate the model is. The numerator of the fraction is a summation of the square of the individual errors. Therefore, smaller errors result in a smaller numerator and a higher index value. The denominator consists of an expression that quantifies how far are the measurements and predicted data points are from the mean of measured data points. This indicates that the effect of errors for data points far from the mean is less significant.

4.2 GHI Decomposition

The global horizontal irradiance (GHI) refers to the instantaneous power incident on a horizontal plane per unit area (W/m^2). This quantity is composed of normal and diffuse incident irradiance. The direct normal irradiance (DNI), or direct beam irradiance, is the irradiance on a plane perpendicular to the line connecting the plane to the solar disc. On the other hand, the diffuse horizontal irradiance (DHI) is the scattered component of the solar irradiation throughout the sky dome. These three quantities can be related via the following relation [77]:

$$GHI = DHI + DNI \cdot \cos(\theta_z) \tag{4.5}$$

The available measured quantity for data validation is only GHI. Knowing that the diffuse and normal components are needed for optical simulations, GHI decomposition models are to be investigated to generate DHI and DNI values for the optical model.

4.2.1 Input Parameters

Air Mass

In addition to the solar zenith angle, air mass is one of the inputs required for decomposition models. It represents the ratio of the direct optical path followed by the solar irradiance to the overhead path length. This quantity can be calculated from the solar zenith angle via equation 4.6 [78].

$$AM = \frac{1.002432 \cdot cos^2(\theta_z) + 0.148386 \cdot \cos(\theta_z) + 0.0096467}{cos^3(\theta_z) + 0.149864 \cdot cos^2(\theta_z) + 0.0102963 \cdot \cos(\theta_z) + 0.000303978} \tag{4.6}$$

Sky Clearness Index

Sky clearness index is the ratio of the incident irradiance on Earth surface to the extra-terrestrial irradiance on the Earth's atmosphere. Due to the elliptical orbit of the Earth around the sun, the extra-terrestrial irradiance varies throughout the year. This variation can be modelled via equation 4.7 [79].

$$E_{Ex} = E_{SC} \cdot \left[1 + 0.033 \cdot cos\left(\frac{2 \cdot \pi \cdot d_n}{365}\right)\right] \tag{4.7}$$

Where:

E_{sc}: Solar constant = 1,367 W/m^2

dn: day number in the year

After calculating the extra-terrestrial irradiance, sky clearness index can be calculated as follows [80]:

$$k_t = \frac{GHI}{E_{Ex} \cdot \cos(\theta_z)} \tag{4.8}$$

4.2.2 Decomposition Models

In this section, two decomposition models from literature and two models developed at TU Delft, by Ajay Jamodkar, are introduced.

Lee Model

This model was developed by K. Lee [81]. It takes the sky clearness index as an only input. The model is defined in equation 4.9:

$$k_d = \begin{cases} 0.92, & k_t \leq 0.2 \\ 0.691 + 2.4306 \cdot k_t - 7.3371 \cdot {k_t}^2 + 4.7002 \cdot {k_t}^3, & k_t > 0.2 \end{cases} \tag{4.9}$$

Reindl-2 Model

This model was developed by D. T. Reindl in 1990. It takes the solar elevation angle and the sky clearness index as inputs. The diffuse coefficient is calculated via a piece-wise function shown in equation 4.10 [82].

$$k_d = \begin{cases} 1.020 - 0.254 \cdot k_t + 0.0123 \cdot \sin(a_s), & k_t \leq 0.3 \\ 1.400 - 0.1749 \cdot k_t + 0.177 \cdot \sin(a_s), & 0.3 < k_t < 0.78 \\ 0.486 \cdot k_t - 0.182 \cdot \sin(a_s), & k_t \geq 0.78 \end{cases} \tag{4.10}$$

Dutch-I and Dutch-II Models

The Dutch-I and Dutch-II models are based on Liu-Jordan models and developed by a A. Jamokdar, a master's student at TU Delft [83]. Both models are piecewise relations that over seven regions of

k_m values. The Dutch-I model describes the diffuse factor as a linear function of clear sky factor and the cosine of zenith angle.

$$k_d = c_1 + c_2 \cdot k_t + c_3 \cdot \cos(\theta_z) \tag{4.11}$$

On the other hand, the Dutch-II model estimates the diffuse factor from quadratic relations of the same inputs.

$$k_d = f_1 + f_2 \cdot k_t + f_3 \cdot \cos(\theta_z) + f_4 \cdot k_t \cdot \cos(\theta_z) + f_5 \cdot {k_t}^2 + + f_6 \cdot \cos(\theta_z)^2 \tag{4.12}$$

Table 4.1 presents the coefficients for Dutch-I and Dutch-II models over the clear sky index ranges.

Table 4.1 Dutch-I and Dutch-II coefficients over the clear sky index regions.

Clear sky index range	*Dutch-I model coefficients*			*Dutch-II model coefficients*					
	c_1	c_2	c_3	f_1	f_2	f_3	f_4	f_5	f_6
[0, 0.3]	0.99	-0.09	0.01	1.00	-0.02	-0.02	0.08	-0.06	-0.01
[0.3,0.4]	1.14	-0.67	0.07	0.93	0.37	0.05	-0.08	-0.61	-0.04
[0.4,0.5]	1.54	-1.79	0.18	1.36	-0.16	0.53	1.96	-2.76	-0.17
[0.5,0.6]	1.65	-2.04	0.23	2.36	-4.63	0.07	-0.69	2.56	0.67
[0.6,0.75]	1.49	-1.76	0.12	2.75	-7.75	3.03	-6.20	6.60	1.41
[0.75,0.8]	-0.17	0.81	-0.32	12.57	-31.99	-0.65	-1.45	21.68	1.25
[0.8,1]	0.00	0.69	-0.35	-2.45	6.97	-1.81	0.76	-3.79	0.73

4.2.3 Results

The four models, described in the previous section, were used to estimate the diffuse factor for a sample year in the Netherlands. Dataset set for a sample year was downloaded from *The Dutch PV Portal 2.0*. Then, the simulated diffuse irradiance values were calculated according to equation 4.13. In fact, the comparison of the decomposition models' performance was based on the DHI values rather than k_d values. This is because the magnitude of resulting residuals in optical simulations depend on the DHI mismatch, not on the k_d mismatch.

$$DHI = k_d \cdot GHI \tag{4.13}$$

Figure 4.2 shows the modelled DHI values vs. the measurements, followed by the calculated statistical indicators of the four models presented in table 4.2.

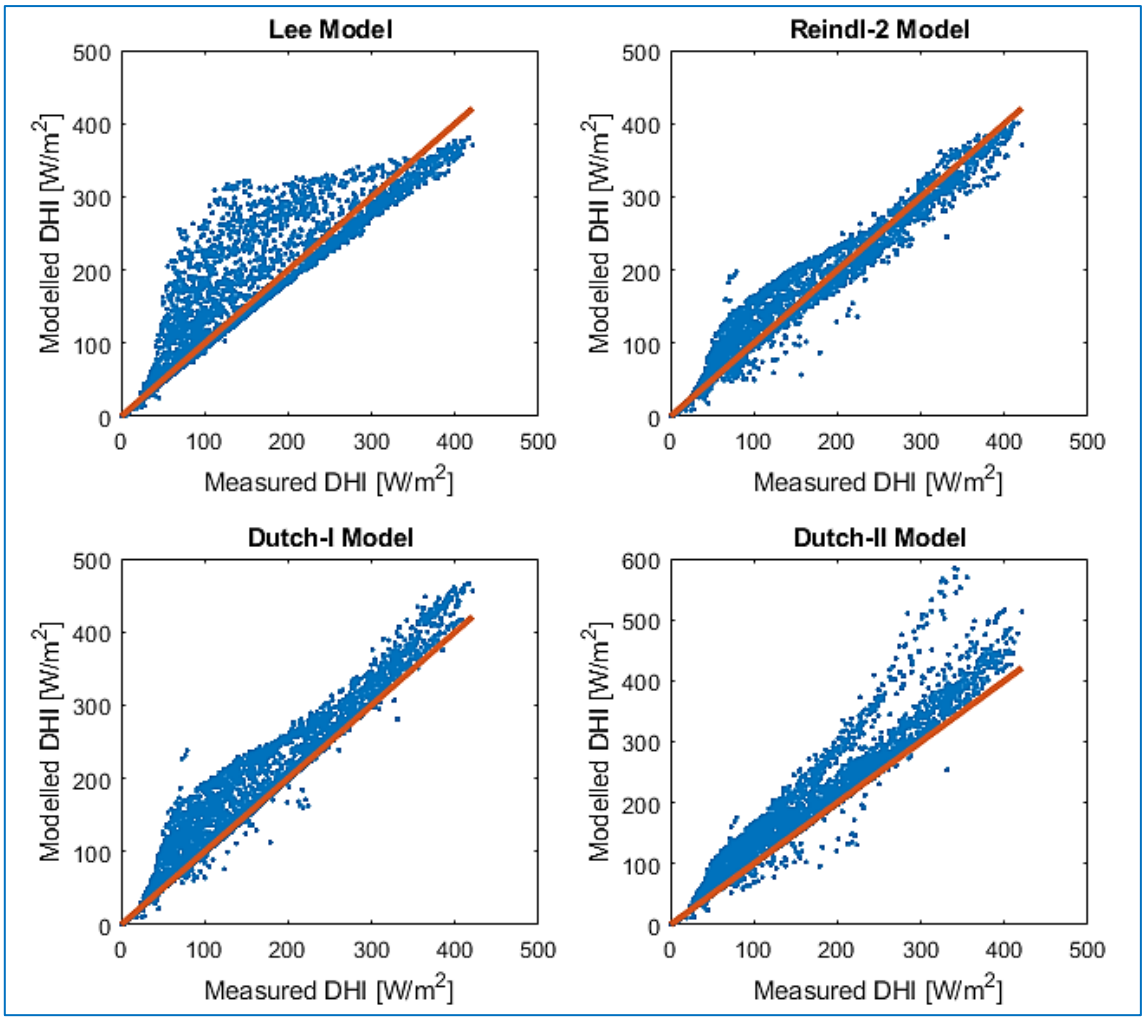

Figure 4.2 Modelled DHI values vs. measured values for the four models.

Table 4.2 Statistical indicators for the GHI decomposition models.

Models	*RMSD [W]*	*MBD [W]*	*SBF*	*WIA*
Lee	41.71	12.23	0.9439	0.9582
Reindl-2	19.71	3.39	0.9544	0.9904
Dutch-I	30.71	17.17	1.0663	0.9794
Dutch-II	37.87	20.57	1.1437	0.9709

It can be inferred from the calculated indicators that Reindl-2 outperforms the three other models. This observation agrees with previous studies at TU Delft. Still, it slightly overestimates the DHI values, especially for low-mid range values; this can be noticed in the graph and from the SBF value. After choosing the decomposition model, the DHI and DNI values can be estimated based on the GHI measurements. Then, the optical and thermal models become ready for simulations.

4.3 Thermal Model Validation

The operating temperature is a decisive factor that influences the module's performance and output power. In fact, a photovoltaic module's temperature varies on a daily and seasonal basis. Therefore,

an accurate thermal model is a prerequisite for accurate energy yield simulations. In the toolbox, a one-dimensional, lumped-element thermal model is used to calculate individual cell temperatures within the module. The current model neglects cross-sectional heat transfer and the effects of power dissipation in case of current mismatch among series-connected cells. The key factors affecting the thermal behaviour are absorbed solar irradiance, convection heat transfer (natural and forced), and radiative cooling with the ground and the sky. In this section, the results of the thermal model present in version 3 will be presented. In addition, applied modifications will be discussed and an assessment of the thermal model performance will be carried out.

4.3.1 Initial Model

The fluid dynamics model, implemented by Elias Garcia Goma [36], is a steady state, textbook model [84]. For energy yield study, the timestep for the toolbox simulations is one hour. Knowing that the time constant for a photovoltaic module thermal response is close to 7 minutes [85], it is convenient to perform steady state analysis. However, for a validation with a timestep of 5 minutes, the module would still be in the transient phase. This may account for an inevitable inaccuracy. In addition, the formula for modelled temperatures must be modified to account for the change in timestep. Figure 4.3 demonstrates the module's thermal response and the module's temperature after a 5-minute timestep.

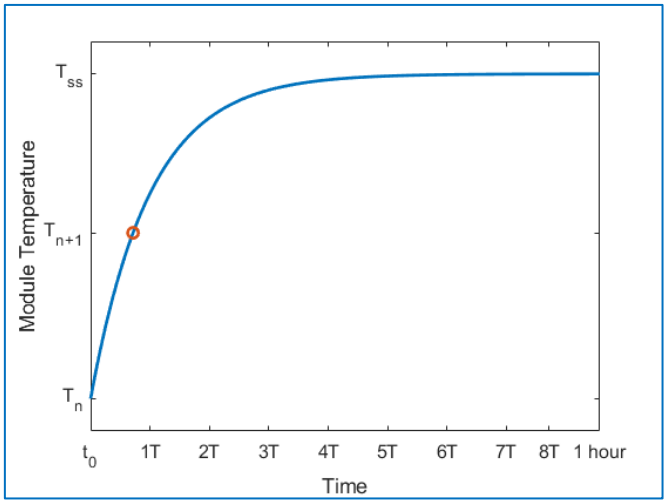

Figure 4.3 Module thermal response.

The module's thermal response is defined by equation 4.14:

$$T(t) = T_{ss} + (T_i - T_{ss}) \cdot exp\left(^{-t}/_{\tau}\right) \tag{4.14}$$

Where T is the instantaneous temperature, T_{SS} is the steady state temperature, T_i is initial temperature and τ is the time constant. Therefore, for the thermal model, the temperature equation can be written as follows:

$$T_{n+1} = T_{ss} + 0.5105 \cdot (T_n - T_{ss}) \tag{4.15}$$

After modifying the temperature equation, the modelled was compared to the measured temperatures. Note that the assessment is conducted by comparing the average temperatures. Figure 4.4 shows the measured and modelled temperatures for the week with highest deviation.

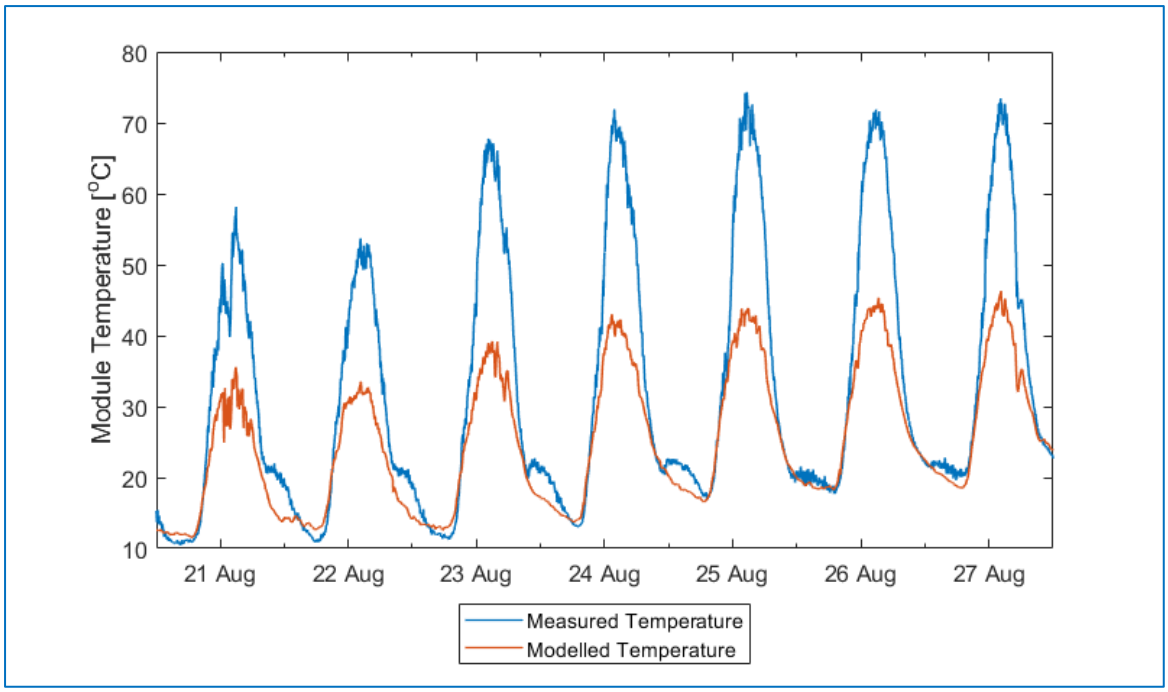

Figure 4.4 Measured and modelled temperatures for the week with highest deviation using the initial model.

As shown, there is a significant deviation between the measured and modelled values, with the highest recorded deviation exceeding 30 ˚C. Therefore, there is a room for improving the model.

4.3.2 Modified Model

In this section, the applied modifications to the thermal model are discussed. These modifications include adjusting the assumptions or approximations without changing the model's essence.

Conductive coefficient

In the original model, the conduction of glass was only considered. However, the module's structure includes layers of Tedlar and EVA. Then, a new coefficient is implemented to account for the series-connected conductive coefficients.

$$h_c = \frac{1}{\frac{1}{h_{glass}} + \frac{1}{h_{EVA}} + \frac{1}{h_{Tedlar}}} = \frac{1}{\frac{d_{glass}}{k_{glass}} + \frac{d_{EVA}}{k_{EVA}} + \frac{d_{Tedlar}}{k_{Tedlar}}} \tag{4.16}$$

Where d and k are the layer thickness and the thermal conductivity. Table 4.3 presents the thicknesses and thermal conductivities of the considered layers.

Table 4.3 Thicknesses and thermal conductivities of the considered layers [86].

Material	*Thickness [mm]*	*Thermal conductivity [W/m.K]*
Glass	4	1.7
EVA	2	0.235
Tedlar	2	0.158

Convective coefficients

In the thermal model, the convective coefficient equation does not account for the air flow type (laminar/turbulent) or for the ambient temperature effect. The original approximation is shown in equation 4.17.

$$h_{forced} = 5.78 + 3.86 \cdot wind\ speed \tag{4.17}$$

However, equation may account for free convective and radiative effects [87]. The new approximation for the forced convective coefficient is [88]:

$$h_{forced} = 2.8 + 3 \cdot wind\ speed \tag{4.18}$$

In addition, the mixed convective coefficient was approximated as the sum of the forced and free coefficients. A more accurate formula is demonstrated in equation 4.19 [9].

$$h_{mixed} = \left({h_{forced}}^{3} + {h_{free}}^{3}\right)^{1/3} \tag{4.19}$$

After applying the mentioned modifications, the modelled and measured temperatures were compared again. Figure 4.5 shows the temperature variations of the new thermal model for the same simulation time of figure 4.4.

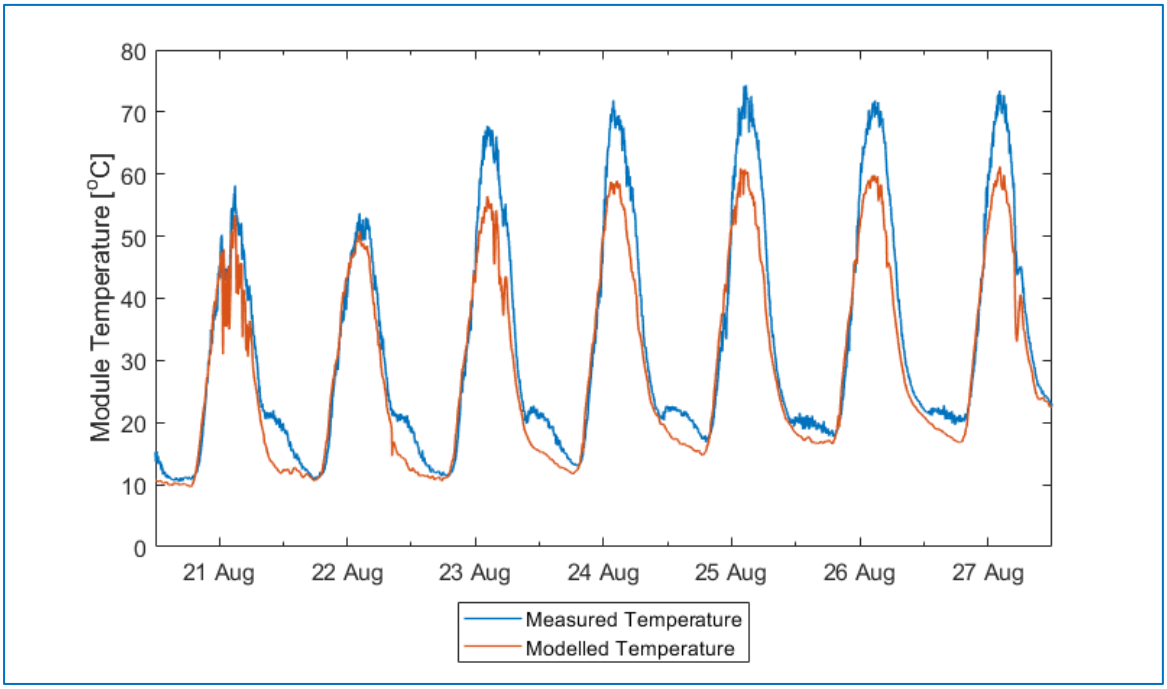

Figure 4.5 Measured and modelled temperatures for the week with highest deviation.

A noted observation from the graph is the significant decrease in deviation between the modelled and measured values. The maximum deviation during the whole period dropped to 17 ˚C. Besides, the plots show that the model underestimates the module's temperature during the peak hours and the late hours of the day.

4.3.3 Results and discussion

To analyse the possible benefits from applying the mentioned modifications to the thermal model, the data point plots of the thermal models' outputs during operating hours are presented in figure 4.6.

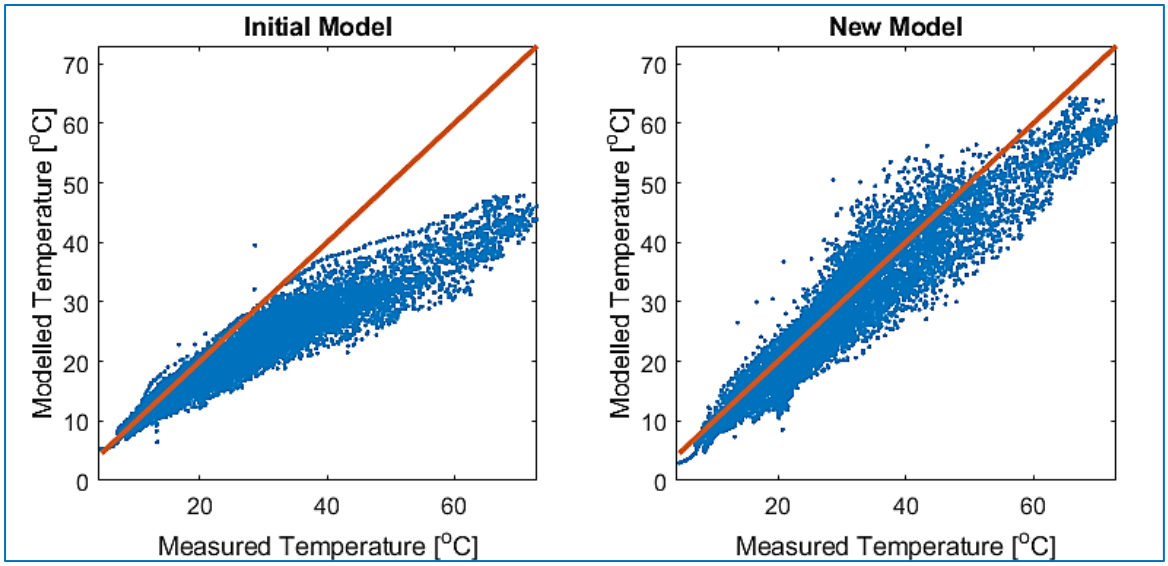

Figure 4.6 Comparison of the initial and modified models' performances.

The improvement in the thermal model's behaviour can be observed visually. To further assess the two models, table 4.4 presents their statistical indicators.

Table 4.4 Statistical indicators for initial and modified thermal models.

Models	*RMSD (°C)*	*MBD (°C)*	*SBF*	*WIA*
Initial	8.764	-6.096	0.544	0.830
New	4.389	-1.966	0.896	0.969

The increase in WIA indicator confirms the, visual, observation from figure 3.5. Still, The MDB indicates that the modified model underestimates the module's temperature. In addition, the SBF value shows that as the simulated temperature increases, the underestimation of the module's temperature increases as well.

Although the new thermal model proves to result in an acceptable performance, the statistical indicators show that there is a room for further improvement. Suggestions are presented below for future work:

1. Accounting for the air flow type (laminar or turbulent) when calculating the convective coefficients
2. Accounting for wind direction when considering the convective heat transfer. It has been proven that for the same wind speed, the convective coefficient may vary by more than 40% depending on the angle between the module and the air flow direction [89].
3. Accounting for the temperature effect on the material properties, such as the thermal conductivity.

4.4 Electric model validation – TU Delft data

This section aims at validating the output of the new electric model, described in chapters 2 and 3, within the toolbox. Comparing the modelled output to measured values is important to assess the accuracy of the electric model. In this section, the DC power output and the operating voltage and current at maximum power point are validated.

In order to evaluate the performance of the electric model, the remaining deviations originating from the thermal model must be eliminated. Therefore, the measured cell temperatures are used as inputs to the electric model. The available measured temperatures are for 7 cells at each time step. To compensate for the missing temperature values of the remaining 9 cells, the mean and standard deviation of the measured temperature values were calculated at every time step. Then, values were generated for the 9 cells using a normal distribution based on the calculated mean and standard deviation.

On the other hand, with the available measurements, it was not possible to eliminate the potential errors of the optical model simulations. These errors are either caused by the optical model itself or the GHI decomposition technique. After generating the temperature values, the electric performance was simulated based on the electric parameters of the in-house photovoltaic module. The outputs comparison will be performed on two levels. At the macro-level, the errors of daily and total yield values are calculated. On the other hand, the micro-level assessment is concerned with the individual output differences.

4.4.1 Macro-Level Validation

The first step for validation is comparing the results at the macro-level, the daily and total yield. The measured and simulated DC energy output are 14.614 kWh and 14.226 kWh. Hence, the simulated energy yield is 2.65% lower than the measured one. The same inputs were used for energy yield simulation on version 3 of the toolbox, resulting in an energy yield error of 7.43%. In addition to the total energy yield comparison, the daily energy yield values are compared. Figure 4.7 shows the daily energy yield deviation throughout the simulation period.

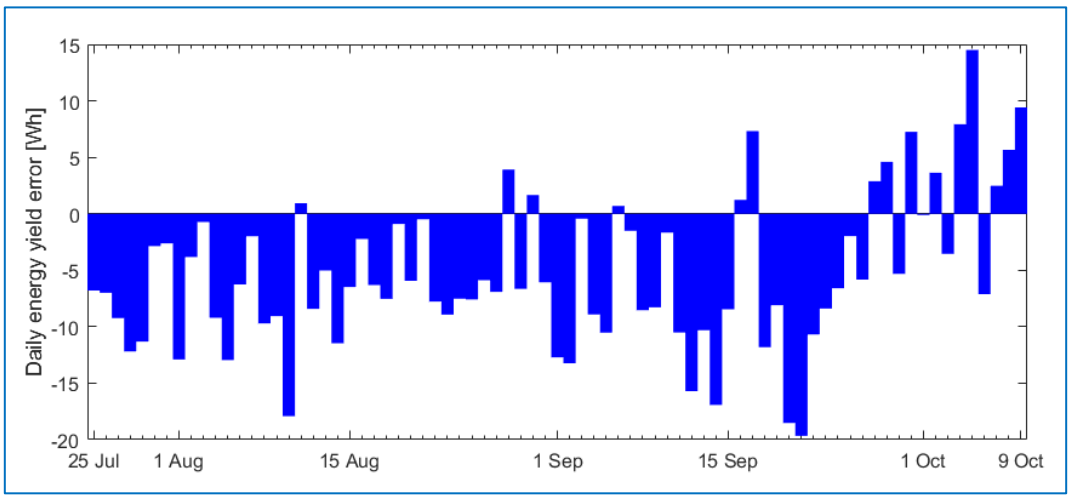

Figure 4.7. Daily energy yield error throughout the simulation period.

As expected from the -2.65% yield error, the model underestimates the energy yield for most of the days. The maximum deviation magnitude between the measured and modelled daily energy yield values is -19.54 Wh, equivalent to the module's output for 24 minutes under STC. Table 4.5 presents the statistical indicators for the daily energy yield. RMSE and MBD are expressed as percentages of mean daily yield. The SBF value, being lower than one, implies that the electric model underestimates the power output for days with high energy yield.

Table 4.5 Statistical indicators for daily energy yield.

	RMSD	*MBD*	*SBF*	*WIA*
Daily yield	4.49%	-2.65%	0.9718	0.9976

4.4.2 Micro-Level Validation

The validation at the micro-level, 5-minute timestep, is important to analyse the model's behavior and pinpoint the possible sources of error. Figure 4.8 shows the measured and modelled electric parameters during August 21-22.

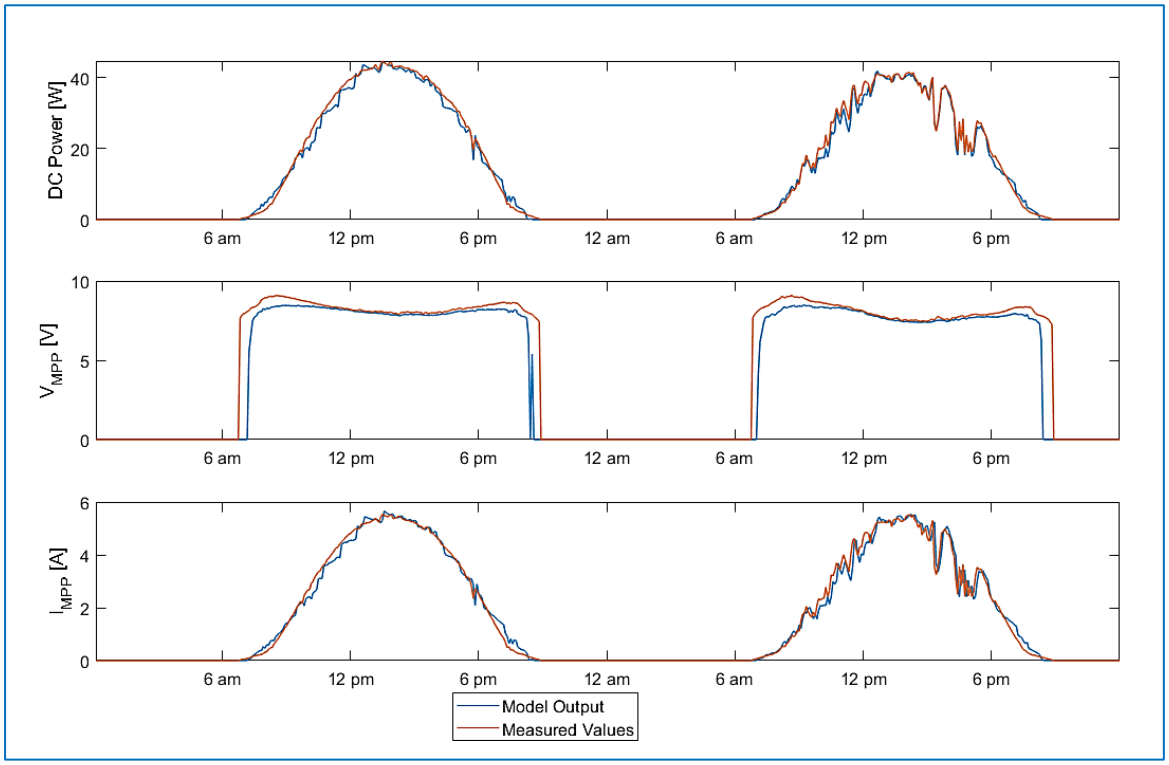

Figure 4.8 Measured and simulated electric parameters during August 21 and 22.

From the V_{MPP} plot, it can be noted that the model underestimates the voltage in the early and late hours of the day, or during the times of low irradiance and low I_{MPP} values. To validate this observation, figure 4.9 shows the voltage bias error variation as a function of modelled I_{MPP} values.

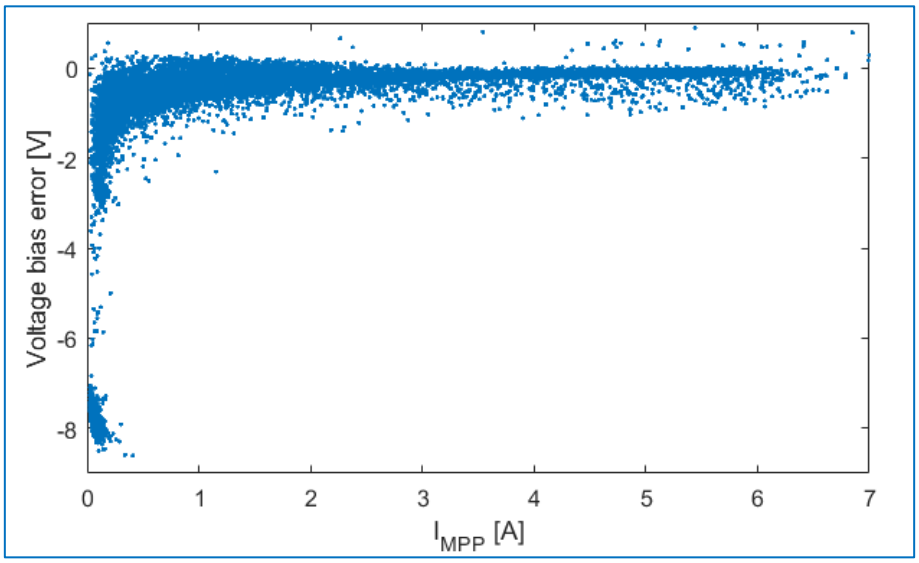

Figure 4.9 The voltage bias error vs. modelled Impp.

In order to further analyse the model's performance, figure 4.10 shows the modelled parameters versus the measured values, followed by calculated statistical indicators presented in table 4.6.

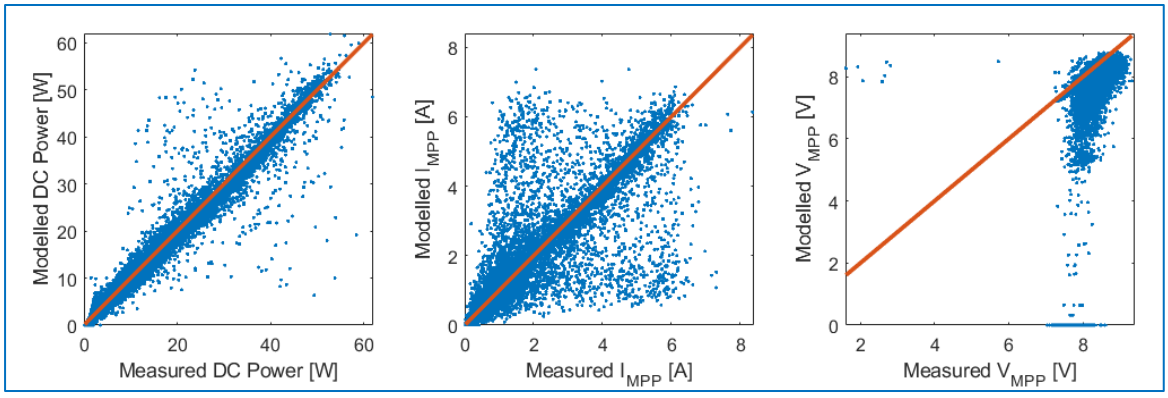

Figure 4.10 Modelled electric parameters vs. measured values.

Table 4.6 Statistical indicators for the electric model parameters.

Quantities	*RMSD*	*MBD*	*SBF*	*WIA*
DC Power	5.94%	-0.824%	0.9769	0.9891
I_{MPP}	17.37%	-0.092%	0.8443	0.9143
V_{MPP}	27.90%	-11.17%	2.7238	0.2740
V_{MPP} (I_{MPP} >1A)	4.19%	-2.517%	0.5309	0.7599

Based on figure 4.10 and table 4.6, the modelled DC power output agrees to a good extent with the measurements, with a small negative bias. On the other hand, the scattered I_{MPP} values result in a high RMSD value, even though the MBD is almost null. This is expected because of the GHI decomposition. Finally, the V_{MPP} values exhibit a large deviation from the measurements. However, when neglecting values modelled at low irradiance levels, the V_{MPP} shows a better agreement with the measured values.

4.5 Electric model validation – NREL data

The data validation for a longer period and different location is an opportunity to test the accuracy and robustness of the electric model. In addition, the used dataset contains measured values of DHI and DNI. Thus, the error resulting from GHI decomposition is eliminated. However, another source of error is present for this dataset. Due to the long period, the module's performance has degraded over time. In fact, the module's STC short circuit current and power output decreased by 0.3% and 1.7% respectively between the start and the end of deployment at Cocoa, Florida [90].

The available values were measured during the day. Therefore, it is not possible to validate the thermal model based on this set of data. Besides, the measured temperature is an average module temperature. To account for temperature difference among cells, a standard deviation value of 1 °C was assumed to generate random cell temperature values based on normal distribution. Finally, the measured irradiance values were not available in 1,046 time steps, out of a total of 38,377; thus these time steps were neglected for the validation.

4.5.1 Macro-level validation

The measured and simulated energy yield of the studied module are 286 kWh and 274.12 kWh, respectively. Therefore, the energy yield percentage error is -4.15%. In addition to the total energy yield, the daily energy yield values were compared. Figure 4.11 shows the daily energy yield deviation for the layout period. The days with missing irradiance values are shaded.

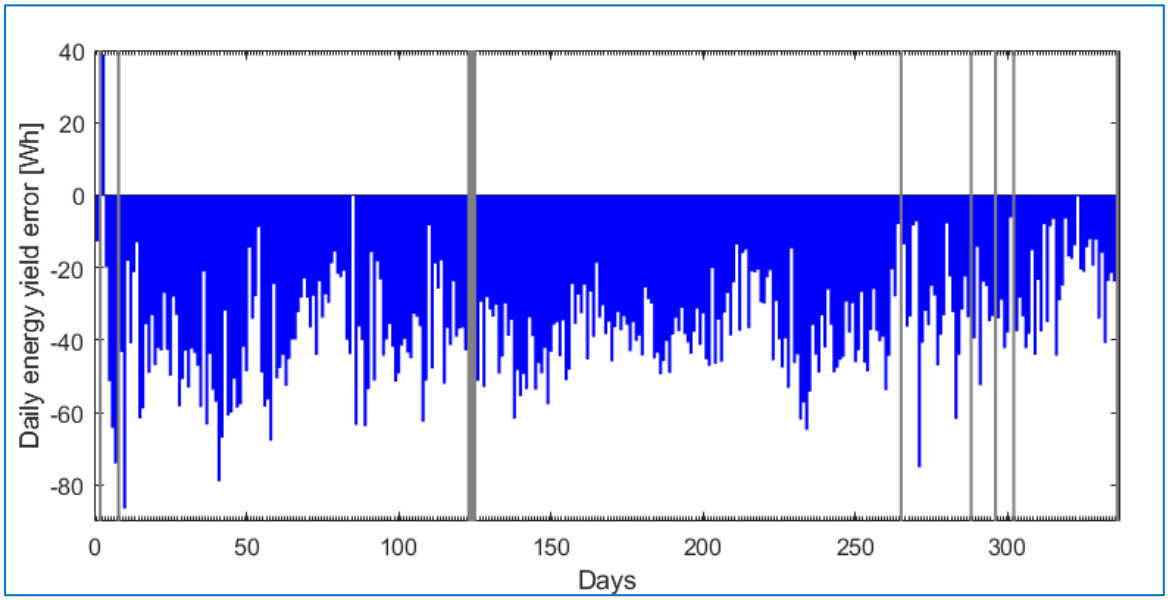

Figure 4.11 Daily energy yield errors in Wh throughout the layout period.

The model underestimates the daily energy yield for the majority of the days. The highest deviation was recorded on February,1 2011. The model underestimated the energy yield by 86.44 Wh. To put this quantity into perspective, it is equal to the power output of the module under STC conditions for 25 minutes. Table 4.7 presents the statistical indicators for the daily energy yield. RMSE and MBD are expressed as percentages of mean daily yield.

Table 4.7 Statistical indicators for daily energy yield

	RMSD	*MBD*	*SBF*	*WIA*
Daily yield	4.49%	-4.16%	0.9773	0.9968

4.5.2 Micro-level validation

The micro-level validation is important to assess the instantaneous output of the electric model. In this section, five electric parameters will be validated. Figure 4.12 presents a comparison between the modelled electric values and the recorded measurements, followed by calculated statistical indicators in table 4.8.

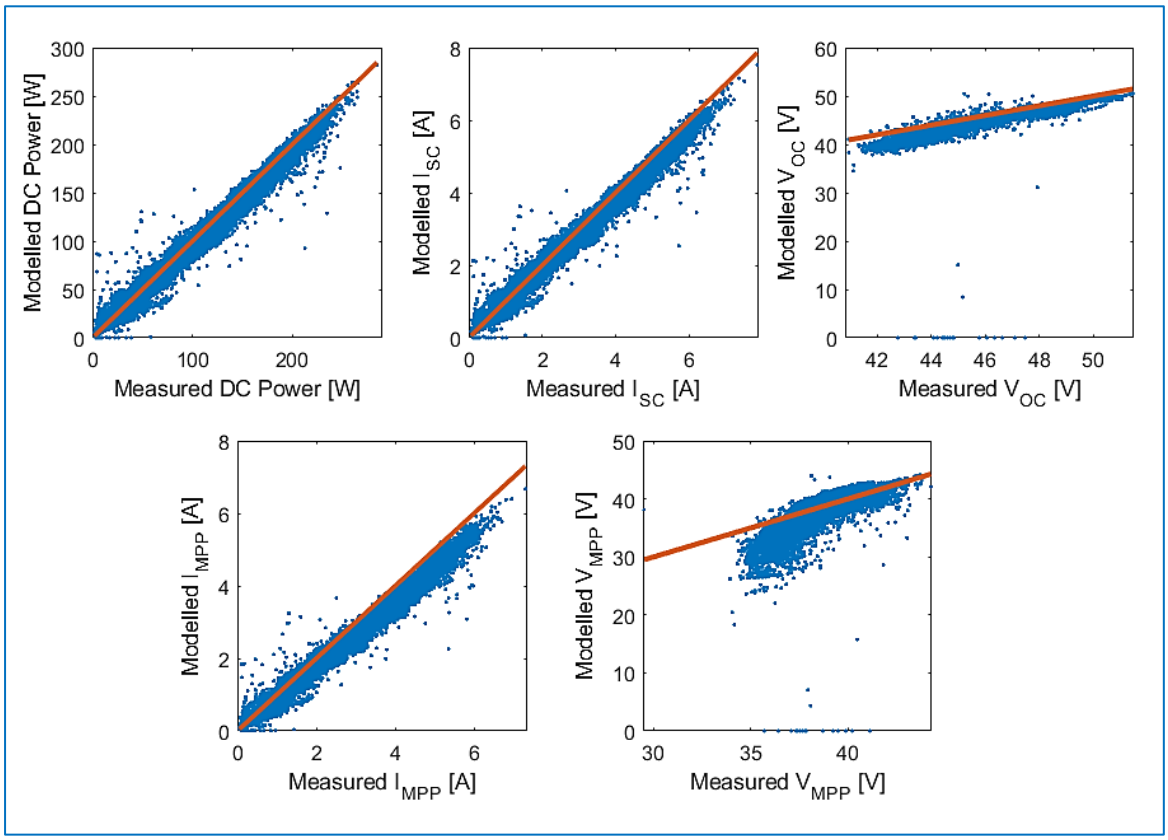

Figure 4.12 Modelled electric parameters vs. measured values.

Table 4.8 Statistical indicators of the electric model parameters.

Quantities	*RMSD*	*MBD*	*SBF*	*WIA*
DC Power	3.674%	-1.777%	0.9610	0.9967
I_{SC}	3.707%	-1.880%	0.9389	0.9962
V_{OC}	2.928%	-1.726%	1.2352	0.8514
I_{MPP}	3.871%	-2.079%	0.9371	0.9959
V_{MPP}	4.018%	-0.886%	1.5073	0.7733

Based on the above graphs and table, the modelled values show a good agreement with the measurements. The short-circuit current errors, affecting the energy yield, are simulated via the optical models. However, that the optical models have been previously validated and showed a

small error margin for the previous validation. Therefore, a probable cause of energy yield error is the errors in recorded irradiance values.

4.5.3 Confidence intervals

With the growing share of photovoltaic technology in the energy mix in power markets, the uncertainty in the yield generation may lead to economic losses or grid-stability problems [91]. Therefore, efficient market operations require uncertainty analysis in addition to the single value yield prediction [92]. The data points for Cocoa validation allows to calculate an 95% confidence interval for the electric model power output.

To calculate the confidence interval, the standard deviation of the residual (SD) must be calculated first. It can be calculated via the following equation.

$$SD = \frac{\sqrt{\sum N \cdot (p_i - m_i)^2 - [\sum (p_i - m_i)^2]^{1/2}}}{N} \tag{4.20}$$

Where N is the number of data points, and p_i and m_i are the predicted and measured data points, respectively. Based on the standard deviation of the residuals and root mean square difference (equation 3.1), the 95% confidence interval can be calculated by equation 4.21 [75].

$$U_{95} = 1.96 \cdot (RMSD^2 + SD^2)^{1/2} \tag{4.21}$$

The confidence interval for the HIT05667 deployed in Cocoa is 20.6 Watts, or 9.57% of the STC power output. This value is fixed for the deployment period. The calculated value is tested for February-1-2011, the day with the highest recorded deviation between the measurements and simulations.

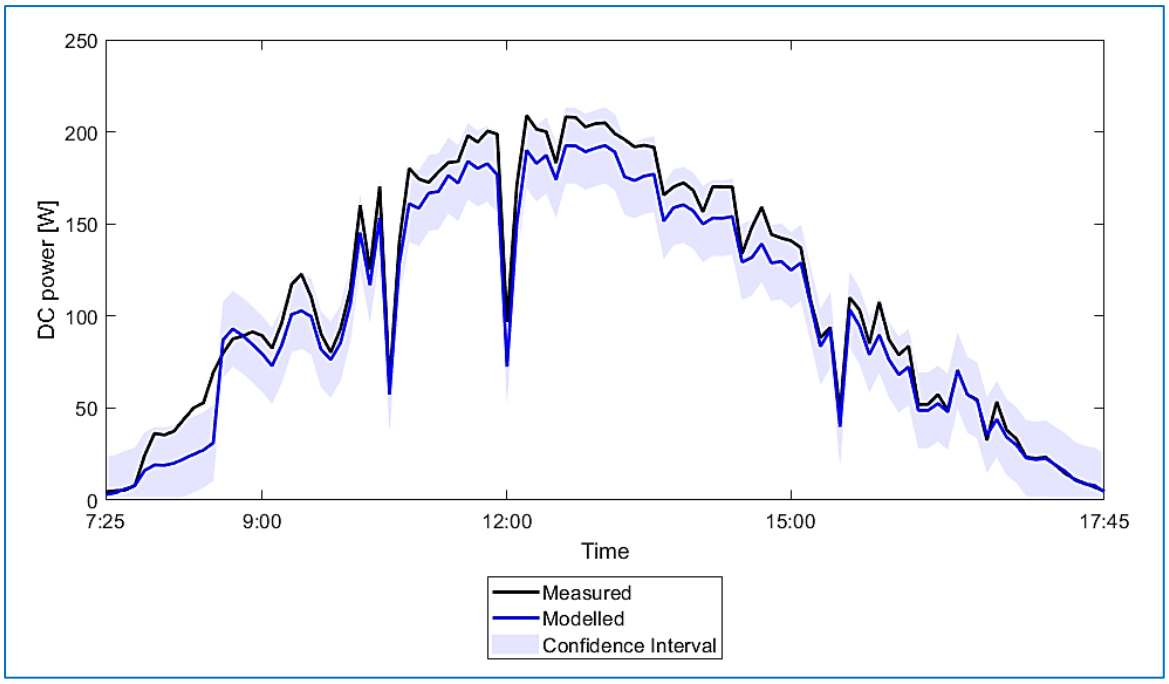

Figure 4.13 The simulated and measured power output and the 95% confidence interval on February-1-2011

It can be noted from the figure that the measured data points are within the 95% confidence interval of the electric simulations, even for the day with the highest recorded deviation. The confidence interval can be even narrower, relative to the modelled output, if the electric model is calibrated or when considering a larger time step such as hourly or daily energy yield simulations.

4.6 Conclusion

In this chapter, the thermal and electric models within the PVMD toolbox are validated. Section 4.1 presents the validation layouts and the four statistical indicators used to assess the models' accuracy and behaviours.

Section 4.2 presents four GHI decomposition models. Based on an assessment of the models' outputs with reference to given data from a sample year in Netherlands, Reindl-2 decomposition model is the best model among the four considered options. This model is used to decompose the measured GHI values for TU Delft data validation.

In section 4.3, the original thermal model is assessed based on measurements at TU Delft. Then, a few modifications were applied in order to enhance the model's performance. After applying the modifications, the new model is assessed again. The modifications result in a significant reduction in RMSD from 8.76 °C to 4.39 °C and reduce the maximum deviation from 31 to 17 °C. Afterward, few recommendations are given for further enhancing the thermal model.

Section 4.4 presents validation of the new electric model, as presented in chapter 2, against measurements recorded at TU Delft. The energy yield deviation of the electric model and the PVMD toolbox are -2.65% and -2.34%. However, the higher accuracy of the latter is based on a masked error since the thermal model underestimates the module's temperature. In addition, the maximum recorded daily energy yield deviation is -19.54 Wh, equivalent to the STC power output for 24 minutes. After analysing the data points, it is noted that the main source of deviation is the underestimation of the module's voltage.

Section 4.5 validates the electric model against a dataset from NREL. An energy yield deviation of -4.16% is recorded. Besides, the highest deviation in the daily energy yield is -86.44 Wh, equivalent to the STC power output for 25 minutes. The statistical indicators of the electric parameters show that the module's current is slightly underestimated during high irradiance conditions, whereas the module's voltage is underestimated at low irradiance conditions. Finally, the 95% confidence interval is calculated and demonstrated for 5-minute time step simulations.

4.7 Recommendations

Despite the improvement of the modified thermal model accuracy, the module temperature error is still significant. A possible source of error is modelling the forced convection coefficient as a linear function of wind speed. However, the nature of air flow, laminar or turbulent, affects the magnitude of convective coefficient [93]. In addition, experiments has shown that the convective coefficient is influenced by the wind direction and the module tilt angle [94]. Considering these two effects, as well as implementing a finite element thermal model, are recommended for better accuracy.

As mentioned in section 4.5, the electric performance of PV modules degrades over time. Therefore, implementing a degradation model can be useful for energy yield calculations. Finally, it is suggested to perform more models validation to examine the accuracy of the toolbox under various climates.

5

Tandem Modules – Case Study

In this chapter, the developed, and validated, electric models will be implemented to simulate the electric performance of tandem modules. Section 5.1 includes a literature review over c-Si/perovskite tandem modules. Afterwards, section 5.2 presents the procedure of optimizing the STC power output for each of the design options. In section 5.3, the optical and electric outputs resulting from AEY simulations are presented and analysed. Finally, the work is summarized, and conclusions are drawn in section 5.4, followed by recommendations for future work in section 5.5.

5.1 Literature Review

Spectral mismatch is one of the key factors for limiting the efficiency of a solar cell. The harvested energy from an absorbed photon is limited by the bandgap of the absorber material. Consequently, the excess photon energy is dissipated via thermalization.

In order to improve the optical performance of a solar cell, research has been conducted on multi-junction cells, or tandem cells. The design of this cell includes two or more absorber layers with different bandgap values. This results in a better spectral performance. In figure 5.1, the useful energy for crystalline silicon and crystalline silicon/perovskite under AM 1.5 spectrum. This figure assumed perfect absorption up to the wavelength corresponding to the absorber's bandgap.

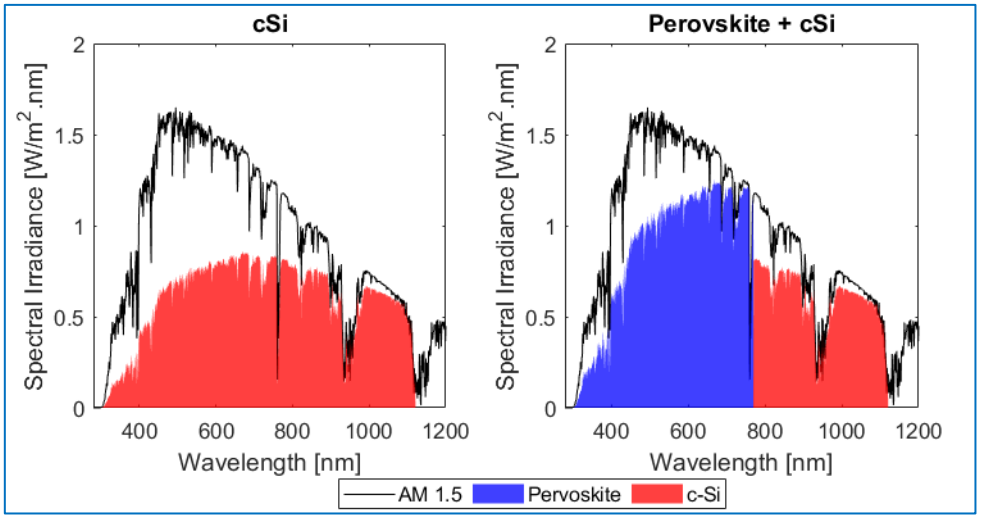

Figure 5.1 Useful energy for c-Si and for Pervoskite/c-Si tandem cells under AM 1.5 spectrum.

5.1.1 Tandem cells

As mentioned before, c-Si/Perovskite tandem cells are considered for this report. The top sub-cell is the novel perovskite cell fabricated by KRICT with efficiency of 22.7% [54]. For the bottom sub-cell, the silicon heterojunction model cell fabricated by Kaneka with an efficiency of 25.1% is considered [52]. Section 2.3 presents the two model cells as well as the methodology used to model their optical and electric behaviours. Aside from removing the back reflector of the model cells, no other modifications were applied to their design.

After defining the tandem cell, the tandem module can be defined as 60 square cells. GenPro4 and Lux optical models are used to generate a sensitivity map of the tandem module. Combining this map with irradiance data results in photo-generated current values for each of the sub-cells. In addition, the fluid dynamics model assumes a negligible thermal mass for the cells. Thus, the two sub-cells are assumed to operate at the same temperature.

After modelling the sub-cells' temperature and photo-generated current values, the electric simulations can be performed. The calibrated lumped element model, presented in chapter 2, is used to generate the I-V curves of the sub-cells for each tandem cell and time step. In addition, the models developed in chapter 3 are used to simulate the electric performance at the module-level. These models account for series-connection between the cells, the bypass-diode behaviour, and the influence of metallization on the electric performance.

The considered types of tandem cells are two-terminal (2T) and four-terminal (4T) stacked tandem cells. In the 2T tandem cells, the two sub-cells are series-connected. Therefore, the I-V curve of the tandem cell can be obtained by applying the series-connection model to the two sub-cells. On the other hand, the electric outputs of the sub-cells in a 4T tandem cell are decoupled. Thus, inter-cell connections are considered separately for the top and bottom sub-cells. In other words, the electric output of the tandem module, at any time step, includes two separate I-V curves. Finally, the metallization model is applied for the 2T tandem cell and for the bottom sub-cell, silicon heterojunction, for the 4T cell.

5.1.2 Cell architecture

In addition to the tandem type, cell architecture has a great influence on the tandem cell behaviour. Light management techniques are critical for enhancing the optical performance of the solar cell. One of the most important techniques is surface texturing which leads to scattering of the incident light and can improve the optical performance by a theoretical limit of $4n^2$, where n is the refractive index of the absorber material [95].

Two designs are considered for surface texturing in tandem cells: a double-side texture design that involves texturing of the front and rear surfaces of the two sub-cells, and a rear-side texture design that involves texturing of the rear surface of the bottom sub-cell. Figure 5.2 illustrates the mentioned architectures as well as a planar reference device for a given 2T tandem cell design[96].

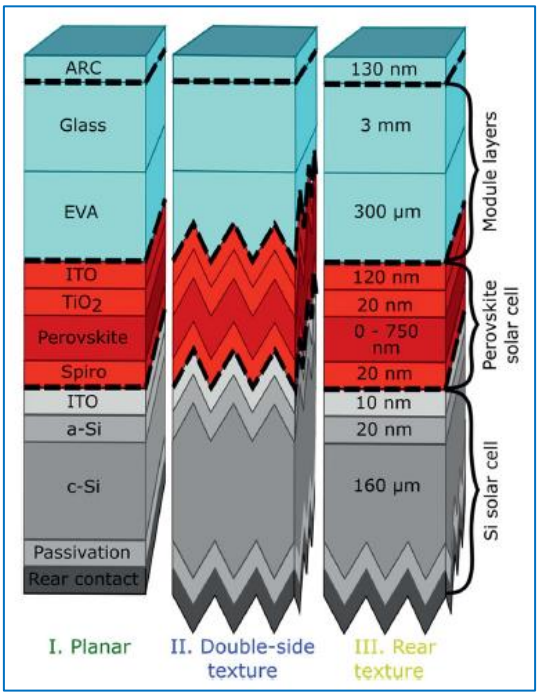

Figure 5.2 Three architecture options for tandem cell design [96].

The 4T tandem cell design assumes stacked, yet electrically decoupled, perovskite and silicon heterojunction sub-cells. On the other hand, the electric performance is coupled in 2T tandem cells. Therefore, four design options are available: 2TT-RT, 2TT-DT, 4TT-RT and 4TT-DT.

The difference in architectures and working principles among the considered tandem modules implies dissimilar optical behaviours. Therefore, a comprehensive comparison between the considered tandem options requires an optimized tandem cell design. To verify this hypothesis, the outputs of a study for the energy yield of 2T tandem modules are presented in figure 5.3 [96]. In 5.3-b, the different shades of green represent different perovskite bandgaps, ranging from 1.55eV for the lightest to 1.88 eV for the darkest.

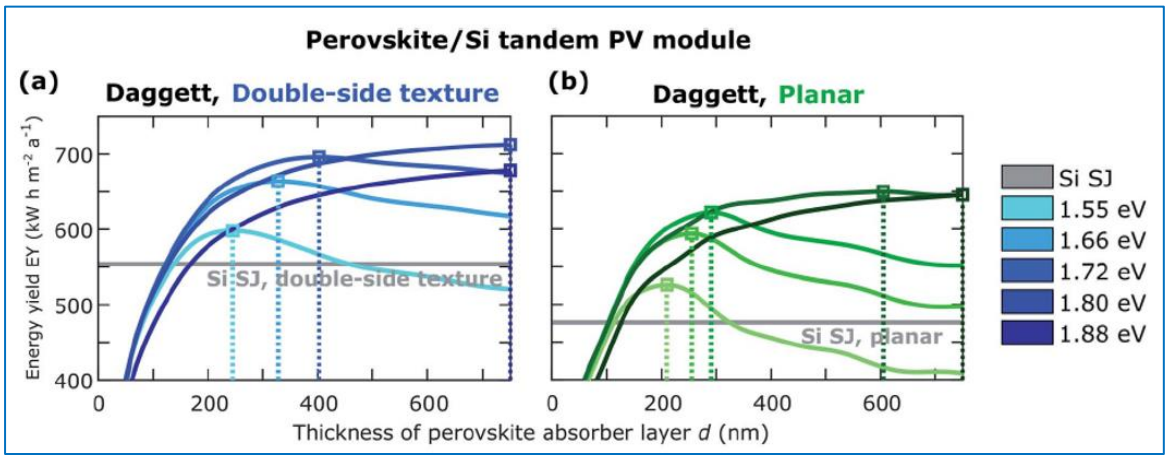

Figure 5.3 Effect of perovskite absorber layer thickness on the energy yield output for a) double-side texture and b) planar tandem cells [96].

Although this study only considers 2T tandem modules, it clearly shows the effects of the cell architecture on the optimal perovskite thickness. It can be noted that a module with double-side texture outperforms the planar module in terms of energy yield. Another important observation is that the energy yield for planar module is more sensitive to the perovskite thickness. Without texture the near infrared response is worse, due to a lack of light trapping. Thus, a 2T tandem will be limited by the bottom cell more quickly as the perovskite thickness increases than one with better light trapping.

5.2 Optimizing power output

For this case study, maximum power output of the 4 design options optimize at STC. The considered degree of freedom for optimization is the perovskite thickness. Assuming no effect of the perovskite thickness on its electric properties, GenPro4 was used to estimate the optimal perovskite thickness for the four considered cells. Optical simulations were run for perovskite thicknesses ranging between 300 and 400 nm, with an increment of 10 nm. The results of these simulations are depicted in figure 5.4. The points in the figure depict the simulation values and the lines represent fits of the variation trends.

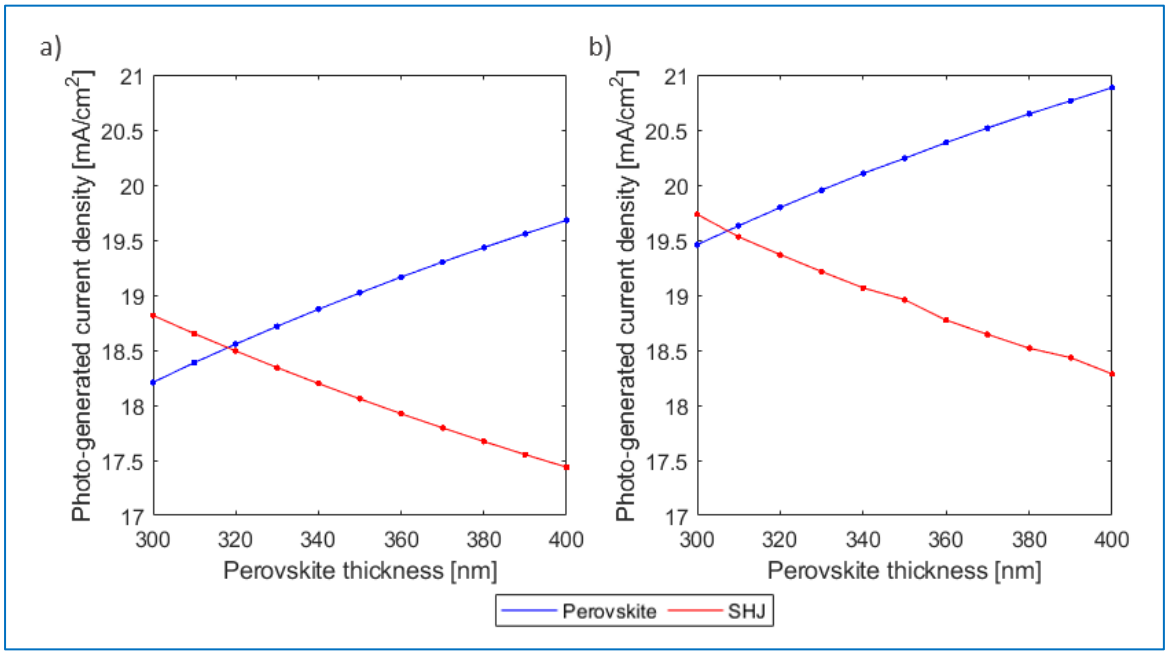

Figure 5.4 The STC photo-generated current of Perovskite and SHJ sub-cells for a) rear-textured cell b) double-textured cell.

For both cell architectures, the same trend can be observed; larger perovskite thickness implies a higher J_{ph} of perovskite and a low J_{ph} of SHJ. Nevertheless, the double-textured cell outperforms the rear-textured cell due to better light management. With the optical simulation results being available, the optimization criteria before choosing the optimal thicknesses.

For 2T tandem cells, power dissipation, resulting from current mismatch, is a significant loss mechanism. Therefore, the optimization criterion is minimizing difference in photo-generated currents between top and bottom cells at STC. Therefore, the optimal perovskite thicknesses are

318 nm for rear-textured tandem module and 307 nm for double-texture tandem module. On the other hand, the electric output of the sub-cells in a 4T tandem cell is decoupled. Thus, the optimization criterion is maximum power output. Figure 5.5 shows the output power density for perovskite and SHJ sub-cells vs. photo-generated current.

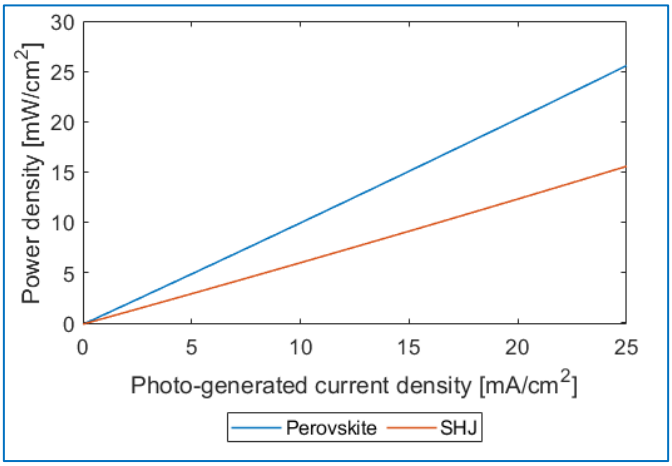

Figure 5.5 Power density for perovskite and SHJ sub-cells vs. photo-generated current density.

Although the efficiency of the SHJ (25.1%) is higher than that of the perovskite cell (22.7%), the perovskite cell is more efficient for the same photo-generated current. This is due to the larger bandgap of perovskite, resulting in a larger amount of energy harvested from absorbed photons. Therefore, for a maximum energy yield, the optimal perovskite thickness is 400 nm for both cell architectures. The I-V curves of the optimized designs at STC are shown in figure 5.6.

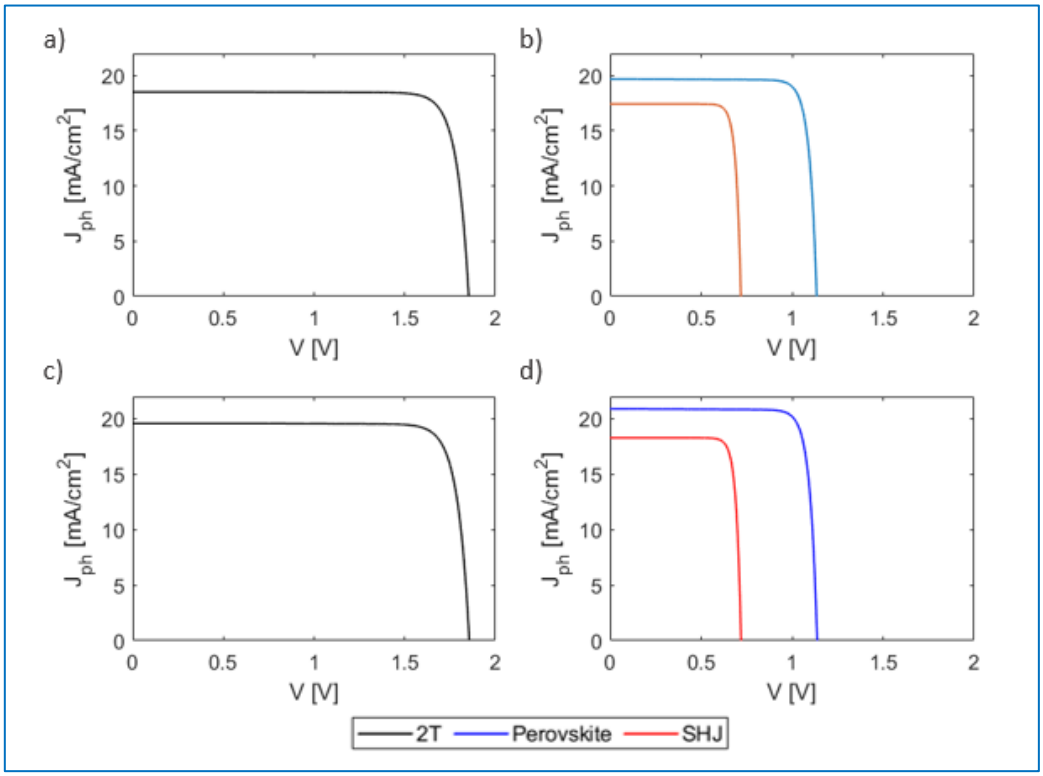

Figure 5.6 J-V curves at STC of a) 2TT-RT b) 4TT-RT c) 2TT-DT d) 4TT-DT

The resulting power densities, from shown J-V curves, are depicted in figure 5.7. As mentioned before, the energy generation contribution of the perovskite is larger than that of SHJ for 4T cells. In fact, the 4TT-DT outperforms the other options with an STC efficiency of 31.5%. This was expected since this option combines good light management with electric decoupling of sub-cells.

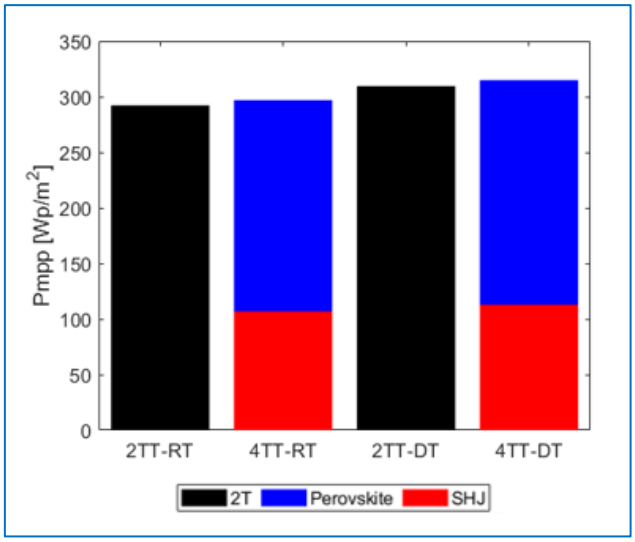

Figure 5.7 Maximum power densities at STC of the four design options.

The best design option offers a higher efficiency than the reference SHJ cell by 25.5%. Nevertheless, these modules are not expected to only perform under STC conditions. In the next section, the performance of these options under real life conditions will be assessed.

5.3 Modelling Results

After optimizing the STC power output of design options, the toolbox was used for an annual energy yield simulation of the tandem modules based on the four design options. The metallization and bypass diode effects were considered for the 2T tandem module and the bottom sub-cell of the 4T tandem modules. The simulations were performed for 72-cell modules, with a tilt angle of 40°, based on weather data of a sample year in Delft. Table 5.1 shows the calculated power output of the four modules.

Table 5.1 STC efficiencies of the four modules.

Modules	*2TT-RT*	*4TT-RT*	*2TT-DT*	*4TT-DT*
STC Power [Watts]	496	517	526	549

5.3.1 Optical performance

Before assessing the simulated electric output, it is crucial to examine the optical outputs of the toolbox simulations. In fact, analysing the optical results can create a better understanding of the weather effects on energy generation. This analysis will only include 2T tandem modules because they are highly affected by current mismatches. Figure 4.8 shows the hourly mismatch between the perovskite and silicon heterojunction sub-cells throughout the year for rear-textured modules. It also includes a plot of the maximum daily solar altitude in Delft.

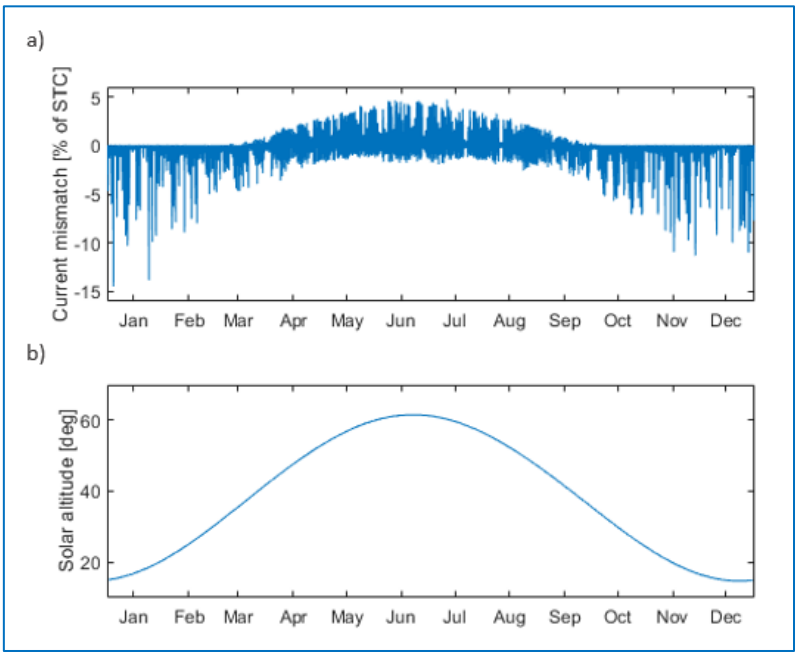

Figure 5.8 a)Hourly current mismatch for 2TT-DT module and b) maximum daily solar altitude throughout the year.

From the above figure, a clear seasonal variation of the current mismatch can be noticed. The same trend, or curve, is visible in the plot of the maximum daily solar altitude. This observation is linked to the irradiance model that is resolved based on the AM spectrum. Lower solar altitudes during the winter months imply higher optical air mass values. Consequently, a higher optical air mass implies a lower average photon energy of the spectrum and thus higher photo-generated current of the bottom sub-cell. A similar trend is followed by the rear-textured tandem module.

Although both 2T tandem modules exhibit similar seasonal variations, their different architectures still lead to different optical, and therefore electric, outputs. To analyse the distinct behaviours of the two modules, the *weekly dissipated photo-generated current* value is used. This quantity is defined as the summation of the weekly summation of the hourly photo-generated current dissipated due to current mismatches. Figure 5.9 shows the variation of the defined quantity over the year.

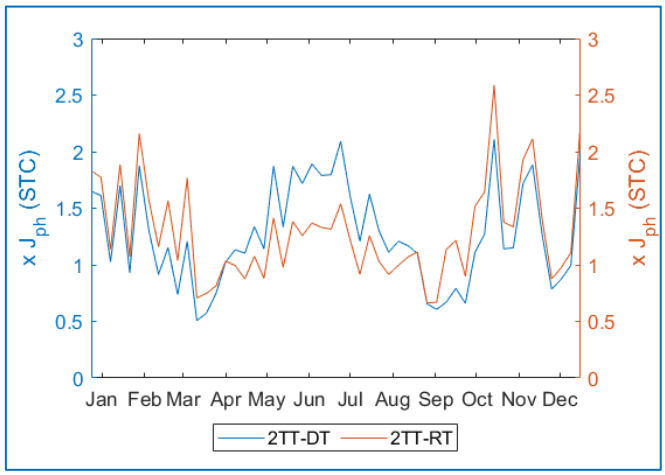

Figure 5.9 Weekly dissipated photo-generated current of 2TT-DT and 2TT-RT.

From the above figure, it can be noted that the current mismatch for the two tandem modules leads to significant electric losses. Nevertheless, the two modules exhibit slightly different seasonal variations. The double-textured module has a smaller current mismatch in the period extending between September and April. On the other hand, more power is dissipated by this module between April and September.

This observation can be related to the seasonal solar altitude, shown in figure 5.8-b, and the effect of the cell architecture on the optical performance. As explained before, during the winter period, the near infrared component of the spectrum is higher compare to the summer period. However, the top cell light management, in the 2TT-DT module, allows a higher absorption potential in the top cell. This results in a better performance of this architecture when compared to 2TT-RT. This advantage is reversed in the summer period, where the current absorbed by the top cells of 2TT-DT increases with the increase of the spectrum APE. In short, when compared to 2TT-RT, the 2TT-DT exhibits advantages for low APE spectrum, during the winter, and suffers from more losses for high APE spectrum, during the summer.

5.3.2 Electric performance

The toolbox was used to simulate the energy yield of the considered modules. Figure 5.10 shows the monthly energy yield of the four modules.

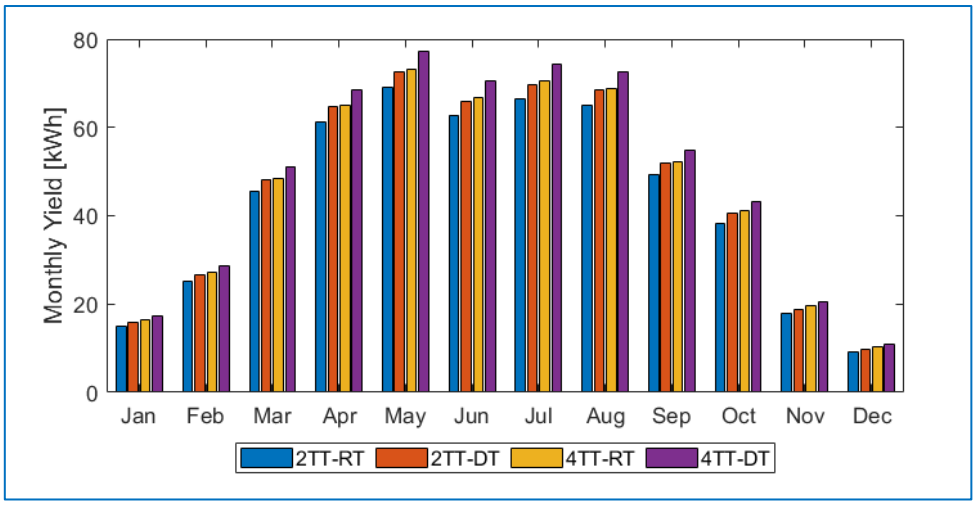

Figure 5.10 Monthly energy yield of the four design options

The monthly energy yield of the four modules follow the same seasonal variation. As expected, based on the modules' designs, the 2TT-RT module generates the least energy yield. This is due to the power dissipation and the light management technique used. On the other hand, 4TT-DT outperforms the other modules since it combines electric decoupling with a good light management technique. The benefit of four-terminal modules, compared to two-terminal, is significant during the summer due to the large solar elevation angles.

Figure 5.11 presents the annual energy yield of the four modules compared to the single junction module, the base case.

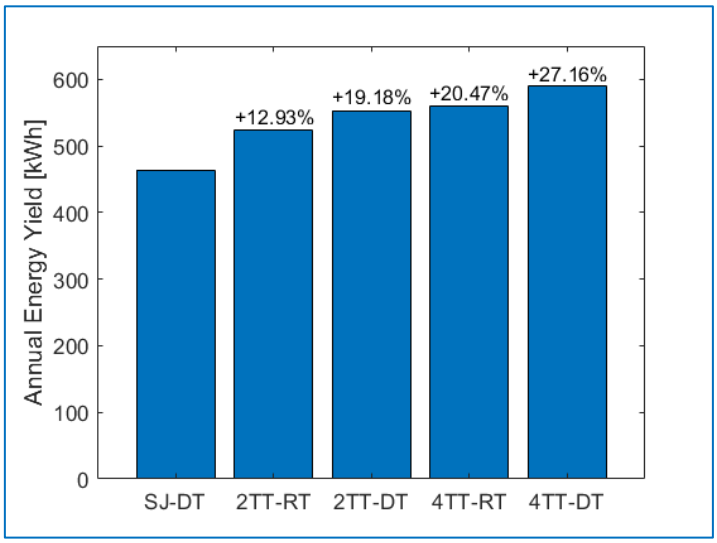

Figure 5.11 Annual energy yield of the four modules, compared to the SJ module.

The results show the benefit of electric decoupling of the sub-cells of four-terminal modules, for both cell architectures. In addition, the double-textured architecture proves to increase the AEY of PV modules. The highest recorded energy yield is for the 4TT-DT, with 590.5 kWh. This quantity represents 27.16% increase compared to the SJ-DT, with an AEY of 464 kWh. In order to analyse the influence of the weather on the modules' output, specific yield is calculated. Equation 5.1 shows describes the definition of this quantity

$$SY = \frac{AEY}{P_{STC}} \ [kWh/kW_p] \tag{5.1}$$

Based on equation 5.1, table 5.2 presents the calculated values of the four modules, compared to the base case.

Table 5.2 Specific yield of the base case and the four modules.

Modules	*SJ-DT*	*2TT-RT*	*2TT-DT*	*4TT-RT*	*4TT-DT*
Specific yield [kWh/kWp]	1143	1056	1052	1081	1075

Because it is the least sensitive to spectral variations, the SJ-DT had the highest specific yield among the considered modules. Besides, the four-terminal modules generated a higher specific yield compared to the two-terminal modules. This is a result of the absence of power dissipation in this design. An interesting observation is that the modules, based on rear-textured architecture, had a higher specific yield than double-textured modules. This result implies that the DT modules are more sensitive to the meteorological conditions that RT modules.

The previous section presents the simulated energy yields of the four design options. These simulations were based on existing irradiance models in the toolbox. In this section, these irradiance models are presented. In addition, their associated assumptions, and their implications, are discussed. This is a motivation for improving the existing models for better simulation results.

An accurate spectral resolution is a prerequisite for accurate optical simulations of solar cells, especially for tandem cells where the optical behaviour of the two (or more) sub-cells are coupled. In order to account for this variation, the toolbox contains a dataset of AM solar spectra. Based on the solar zenith angle, this data is used to model the spectral resolution of solar irradiance. While this data is accurate for describing the direct normal irradiance, it may result in some errors in the diffuse spectrum. The diffuse irradiance is mainly caused by the scattering of the incident solar irradiance in the atmosphere. Therefore, the spectral composition of diffuse irradiance can be modelled as a function of the cloud coverage, albedo, turbidity and ground reflection [97].

5.4 Conclusions

This chapter presents case studies for energy yield simulations of c-Si/Perovskite tandem modules. The simulations were performed by utilizing the developed electric models in chapters 2 and 3.

Section 5.1 includes a literature review to study the different tandem cell layouts and architectures. and modelling assumptions are defined. Based on the review, four design options were considered: 2TT-RT, 2TT-DT,4TT-RT and 4TT-DT. Section 5.2 presents the STC power optimization procedure for the four design options. Based on defined criteria, the optimization resulted in optimal perovskite thicknesses for the design options: 307 nm for 2TT-DT, 318 nm for 2TT-RT and 400 nm for the 4TT designs. In section 5.3, the toolbox was used to simulate the performance of the four tandem modules. Then, the optical and electric outputs were analysed. Compared to SJ module, the tandem modules generated more energy yield. The increase percentage ranges between 12.93% for 2TT-RT and 27.13% for 4TT-DT. However, the specific yield of the tandem modules was lower than that of the SJ module. Therefore, it can be concluded that tandem modules are more sensitive to meteorological conditions.

5.5 Recommendations

The irradiance model is a key factor in determining the thermal and electric behaviour of the modelled PV module. The current irradiance model resolves spectrally the incident irradiance based on the AM spectrum. Although this can be considered as a good approximation, research has shown that the spectral composition of diffuse irradiance can be influenced by several factors including ground reflection, aerosol scattering and cloud scattering [97]. Thus, implementing a spectral model for the diffuse irradiance is crucial for better accuracy, especially for tandem modules simulation. In addition, the current irradiance model does not consider the possible effects of the cloud coverage on the irradiance distribution and, consequently, the module POA irradiance. Therefore, the influence of cloud coverage is to be studied. Finally, irradiance model validation is suggested to assess the possibility of inaccuracy.

In this, the developed work focused on investigating the effects of architecture and electric configurations (2T and 4T) on c-Si/Pervoskite tandem cells. Three-terminal tandem configuration is a less known design with efficiency that can reach 32% for c-Si/Perovskite tandem cells. It is recommended to model this configuration using equivalent circuits. In addition, it is recommended to optimize the AEY of tandem cells by modifying the top cell design, absorber bandgap and thickness, for a given location and weather data.

6

Conclusions

This chapter presents answers to the research questions defined in chapter 1, draws conclusions, and gives recommendations for future development. The MSc thesis project aimed at improving the PVMD Toolbox, an energy yield prediction software package for photovoltaic systems. In short, the main purpose of the project is to develop an

"Improved Electrical Model and Experimental Validation of the PVMD Toolbox-Extending the Energy Yield Prediction Model to Tandem PV Modules"

Section 6.1 summarizes the work done to achieve the defined thesis objectives. Section 6.2 includes the improvements implemented on the toolbox code. Finally, an outlook for future work is presented in section 6.3

6.1 Conclusions

This section summarizes the results and draws conclusions.

Electric Model Improvements

In chapter 2, an electric model was developed at the cell level. First, reference cells were chosen for the toolbox simulations. Then, input parameters of GenPro4 and ASA7 were adjusted to match the optical and electric behaviour of the reference cells from literature under standard test conditions. Parameter-by-parameter approach was successful at extracting the diode model parameters based on the simulated I-V curves. Based on the fittings of extracted parameters, a *Calibrated Lumped Element Model* was introduced.

In chapter 3, the electric model is extended to simulate the electric behaviour on the module-level based on the generated I-V curves of individual cells. The effects of power dissipation and bypass diodes were modelled. Furthermore, a metallization model, already developed by a master's student in the PVMD group, was implemented to account for shading and series resistance effects. Finally, a cell mapping algorithm was developed and implemented to the toolbox. For an annual energy yield simulation of a silicon heterojunction module, this algorithm decreased the number of cell simulations by 86%, reducing the computation time of the electric model by a factor of 5. Besides, the AEY error resulting from this algorithm was 0.22% and the root mean square difference of the hourly predicted yield was 0.13% of the STC power output.

As a conclusion, the work presented in chapters 2 and 3 fulfilled the first objective of the thesis by developing a model that simulates the electric behaviour at the cell and module levels. Compared to version 3 of the toolbox, the developed electric model is more realistic because it accounts for the effects of temperature and irradiance on all diode-model parameters as well as the cells' connections influence. In addition, the computation time for the electric model was drastically

reduced. For an annual energy yield simulation of silicon heterojunction, the electric simulation time dropped by a factor of 45, from 1.5 hours to less than 2 minutes (4 CPUs, 3 GHz, 8 GB RAM).

After implementing the electric model, two datasets were used to validate the thermal and electric models in the toolbox. Electric and temperature measurements for an in-house module were recorded at TU Delft. In addition, a dataset for a HIT module in Cocoa – Florida, provided by NREL, was used. The data recorded at Delft contained GHI as the only irradiance measurements. After comparing four decomposition models, Reindl-2 was selected as the most appropriate for the Dutch climate. Upon validating the existing thermal model in the toolbox, the results showed that it underestimates the module's temperature with a RMSD of 8.674 ˚C and an MBD of -6.096 ˚C. Various modifications were implemented on the conductive and convective coefficients in the thermal model. As a result, the modified version showed better agreement with the measurements as the RMSD and MBD dropped to 4.389 ˚C and -1.966 ˚C, respectively. Afterwards, the electric model outputs (*Pmpp,Vmpp*, *Impp*) were validated against measurements. The simulated parameters showed a good agreement with the measurements. The accuracy of the toolbox has improved with the energy yield error -2.65%, compared to 7.43% for version 3. Besides, the largest daily energy yield was -19.54 Wh, equivalent to module STC power output for 24 minutes.

The validation based on NREL data tested the electric model robustness as it was recorded in different location and for a longer period. Again, the simulated electric parameters were compared to the recorded measurements. The simulated values showed a good agreement with the measurements with an AEY error of -4.15% and a highest daily yield error of only 86.44 Wh, equivalent to module STC power output for 25 minutes. In addition, it was possible to calculate the 95% confidence interval of the module's power output.

The developed electric model was utilized for tandem modules simulations. The considered cell architecture options were rear-textured and double-textured designs. In addition, the electric configuration options included two-terminal (2T) and four terminal (4T). Assuming 72-cell tandem modules with the same size of SHJ commercial modules, simulations were run for the four design options based on Delft weather data. Out of the four options, the 4T-double textured tandem module resulted in the highest AEY, with a 27.16% increase compared to a SHJ module. Nevertheless, tandem modules generated lower specific yield, compared to a SHJ module, with small advantage of four-terminal modules over two terminal ones.

6.2 Toolbox improvements

In addition to the implementation of developed models in the toolbox, several improvements were applied on the toolbox to guarantee a user-friendly experience. These improvements include:

- Easy input of simulations options, such as simulation period, metallization parameters, number of bypass diodes and a better representation of the simulation outputs
- Possibility of performing optical simulations to a thin film module layout
- Autosaving the generated plots and data as *png* and *dat* files in *Results* folder
- Possibility of loading saved optical simulation results for a faster use

Besides, an AC/DC power conversion model was implemented by Tim Stark, MSc student in the PVMD group.

6.3 Outlook – extending the energy yield simulation

The current version of the toolbox simulates the AEY of a single module. However, most photovoltaic systems, such as solar farms and solar roofs, include more than one module. Therefore, it is recommended to extend the application of the toolbox to simulating the AEY of PV arrays. In fact, the developed cell mapping algorithm can limit the computation time for PV arrays because the cells are expected to operate at similar conditions. Besides, the implemented power conversion model allows to simulate the power electronics at the array level.

A

Reference Cells Design

This appendix presents a detailed design of the reference cells.

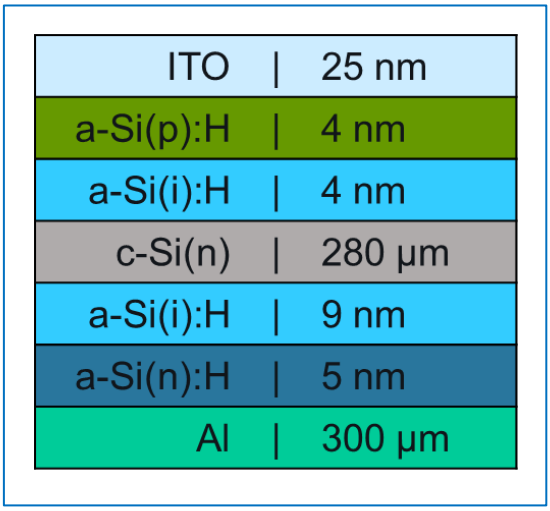

Figure A.1 The design of SHJ reference cell.

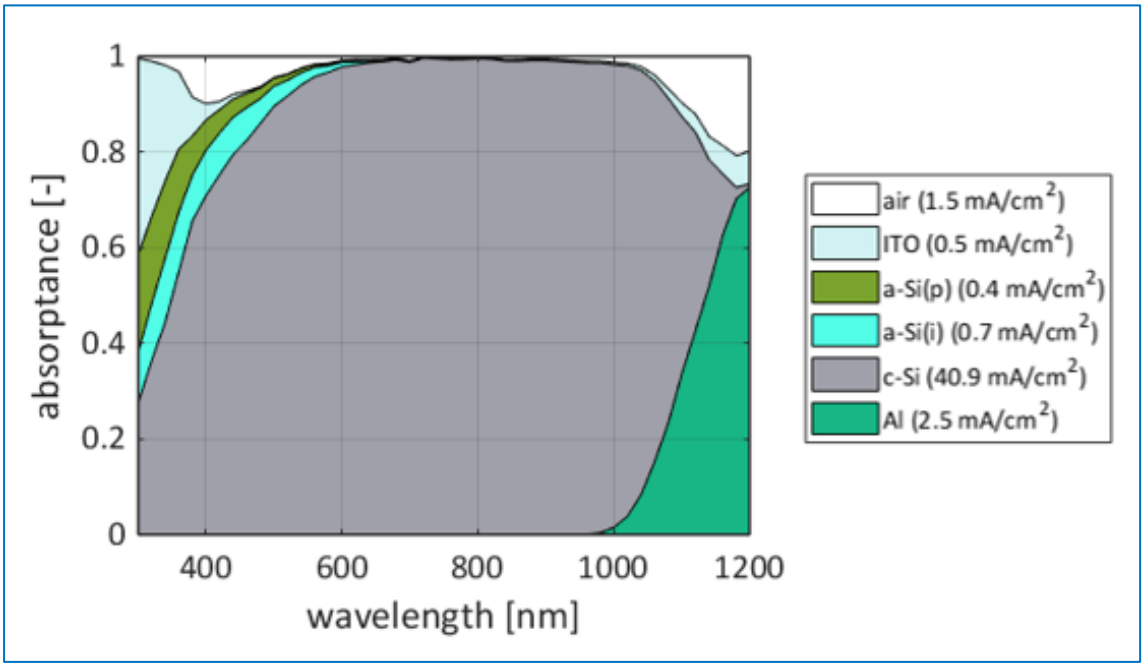

Figure A.2 Absorption of different layers under STC irradiance.

Table A.1 Optical properties of SHJ reference cell layers.

λ	*ITO* [98]		*a-Si(p):H* [99]		*a-Si(i):H*		*c-Si(n)* [100]		*a-Si(n)* [101]		*Al* [102]	
(nm)	*n*	*k*	*n*	*k*	*n*	*k*	*n*	*α*	*n*	*k*	*n*	*k*
300	2.290	0.366			4.410	1.802	5.060	1.7E6	3.750	3.156	6.768	41.03
325	2.342	0.271			4.410	1.802	5.140	1.2E6	4.176	2.803	6.013	38.15
350	2.308	0.174	4.275	1.356	4.410	1.802	5.480	1.0E6	4.476	2.420	5.446	35.63
375	2.271	0.094	4.186	1.028	4.601	1.404	6.705	5.0E5	4.667	2.041	4.874	33.37
400	2.232	0.041	4.083	0.769	4.752	1.148	5.590	9.5E4	4.771	1.682	4.450	31.50
425	2.195	0.022	3.964	0.569	4.793	0.943	5.010	4.5E4	4.808	1.356	4.058	29.85
450	2.157	0.012	3.837	0.413	4.748	0.769	4.680	2.6E4	4.793	1.068	3.671	28.26
475	2.118	0.006	3.709	0.294	4.686	0.551	4.455	1.6E4	4.741	0.821	3.371	26.93
500	2.084	0.003	3.588	0.203	4.607	0.402	4.290	1.1E4	4.662	0.612	3.070	25.60
525	2.059	0.003	3.482	0.137	4.541	0.311	4.170	8.3E3	4.566	0.442	2.850	24.48
550	2.040	0.004	3.390	0.088	4.425	0.236	4.080	6.4E3	4.462	0.307	2.630	23.35
575	2.023	0.004	3.314	0.053	4.310	0.161	4.005	5.1E3	4.355	0.204	2.446	22.35
600	2.008	0.004	3.251	0.034	4.205	0.108	3.940	4.1E3	4.250	0.130	2.264	21.37
625	1.994	0.005	3.200	0.021	4.111	0.070	3.890	3.4E3	4.155	0.081	2.123	20.55
650	1.980	0.006	3.156	0.014	4.031	0.037	3.840	2.8E3	4.072	0.051	1.987	19.78
675	1.967	0.006	3.120	0.009	3.964	0.020	3.810	2.3E3	4.001	0.032	1.880	19.05
700	1.953	0.007	3.089	0.007	3.906	0.010	3.770	1.9E3	3.942	0.021	1.772	18.32
725	1.940	0.007	3.063	0.005	3.881	0.005	3.745	1.6E3	3.893	0.014	1.684	17.72
750	1.926	0.008	3.040	0.004	3.859	0.002	3.720	1.3E3	3.851	0.009	1.595	17.14
775	1.912	0.009	3.021	0.003	3.810	0.001	3.705	1.1E3	3.815	0.006	1.517	16.57
800	1.897	0.010	3.003	0.002	3.790	4E-4	3.680	8.5E2	3.784	0.004	1.440	16.00
825	1.883	0.011	2.988	0.002	3.766	1E-4	3.665	6.8E2	3.757	0.003	1.384	15.44
850	1.868	0.012	2.975	0.002	3.737	4E-5	3.650	5.4E2	3.734	0.002	1.329	14.89
875	1.852	0.013	2.963	0.001	3.709	1E-5	3.635	4.1E2	3.713	0.002	1.293	14.43
900	1.836	0.014	2.952	0.001	3.684	3E-6	3.620	3.1E2	3.695	0.001	1.259	13.98
925	1.820	0.015	2.942	0.001	3.664	9E-7	3.605	2.3E2	3.678	0.001	1.243	13.56
950	1.803	0.017	2.933	0.001	3.649	1E-6	3.590	1.6E2	3.663	0.001	1.229	13.16
975	1.786	0.018	2.925	0.001	3.634	1E-6	3.580	1.1E2	3.650	0.001	1.219	12.83
1000	1.768	0.020	2.918	0.001	3.619	1E-6	3.570	6.4E1	3.638	4E-4	1.210	12.50
1025	1.753	0.021			3.619	1E-6	3.560	3.5E1	3.627	3E-4	1.210	12.13
1050	1.734	0.023			3.619	1E-6	3.550	1.6E1	3.617	3E-4	1.210	11.81
1075	1.715	0.025			3.619	1E-6	3.550	7.1E0	3.608	2E-4	1.205	11.49
1100	1.694	0.027			3.619	1E-6	3.540	3.5E0	3.599	2E-4	1.201	11.17
1125	1.673	0.029			3.619	1E-6	3.535	1.8E0	3.591	1E-4	1.205	10.87
1150	1.652	0.031			3.619	1E-6	3.530	0.680	3.584	1E-4	1.212	10.58
1175	1.630	0.034			3.619	1E-6	3.525	0.145	3.577	1E-4	1.234	10.31
1200	1.606	0.036			3.619	1E-6	3.520	0.020	3.571	1E-4	1.257	10.04

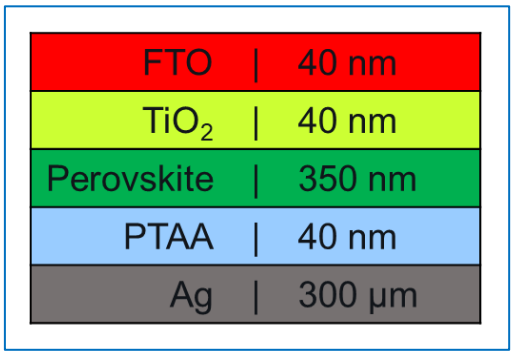

Figure A.3 The design of perovskite reference cell.

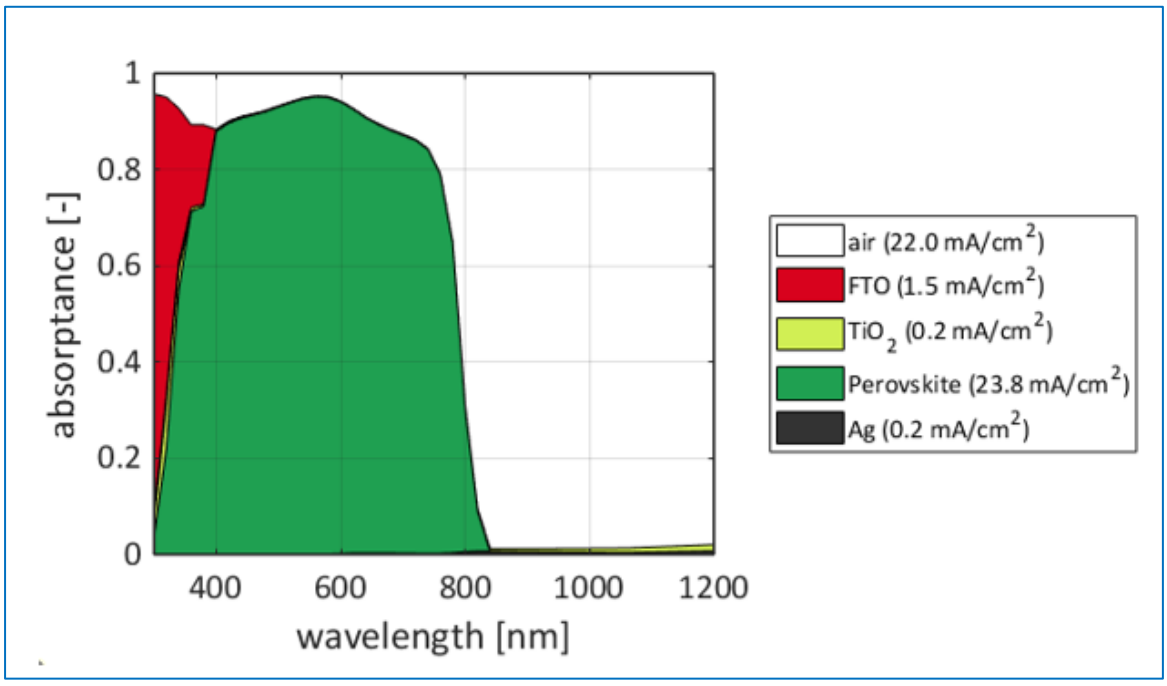

Figure A.4 Absorption of different layers under STC irradiance.

Table A.2 Optical properties of perovskite reference cell layers.

λ	*FTO* [103]		TiO_2 [104]		*Per.* [105]		*PTAA* [106]		*Ag* [102]	
(nm)	*n*	*k*	*n*	*k*	*n*	*k*	*n*	*k*	*n*	*k*
300	2.289	0.078	2.998	0.412	1.675	0.926	1.472	1.47E-1	1.346	0.986
325	2.140	0.018	2.891	0.137	1.686	0.959	1.430	2.87E-1	0.546	0.572
350	2.069	0.009	2.691	0.007	1.833	1.193	1.450	4.36E-1	0.115	1.318
375	2.031	0.007	2.558	0.000	2.244	1.333	1.657	6.33E-1	0.060	1.764
400	2.005	0.005	2.487	0.000	2.624	1.078	2.099	5.33E-1	0.050	2.103
425	1.985	0.004	2.440	0.000	2.646	0.832	2.009	4.22E-2	0.043	2.402
450	1.969	0.003	2.405	0.000	2.612	0.735	1.865	3.11E-2	0.040	2.648
475	1.956	0.003	2.379	0.000	2.615	0.705	1.804	3.09E-2	0.050	2.901
500	1.943	0.002	2.358	0.000	2.670	0.643	1.778	3.45E-2	0.050	3.130
525	1.932	0.002	2.341	0.000	2.745	0.577	1.766	2.71E-2	0.051	3.362
550	1.922	0.002	2.328	0.000	2.773	0.460	1.751	1.55E-2	0.060	3.597
575	1.912	0.002	2.316	0.000	2.746	0.360	1.734	8.49E-3	0.052	3.800
600	1.902	0.002	2.306	0.000	2.690	0.281	1.720	5.58E-3	0.055	4.009
625	1.893	0.002	2.298	0.000	2.641	0.234	1.709	4.28E-3	0.058	4.215
650	1.883	0.002	2.290	0.000	2.595	0.209	1.701	3.50E-3	0.052	4.409
675	1.874	0.002	2.284	0.000	2.563	0.199	1.693	2.94E-3	0.047	4.605
700	1.864	0.003	2.278	0.000	2.544	0.193	1.687	2.50E-3	0.041	4.802
725	1.854	0.003	2.273	0.000	2.541	0.188	1.682	2.16E-3	0.036	4.998
750	1.844	0.003	2.269	0.000	2.557	0.172	1.677	1.88E-3	0.031	5.194
775	1.834	0.003	2.265	0.000	2.569	0.115	1.673	1.65E-3	0.033	5.383
800	1.824	0.004	2.261	0.000	2.517	0.033	1.669	1.47E-3	0.037	5.569
825	1.814	0.004	2.258	0.000	2.423	0.002	1.666	1.32E-3	0.040	5.758
850	1.803	0.005	2.255	0.000	2.371	0.000	1.663	1.19E-3	0.040	5.965
875	1.792	0.005	2.252	0.000	2.343	0.000	1.660	1.08E-3	0.040	6.171
900	1.781	0.006	2.249	0.000	2.326	0.000	1.657	9.84E-4	0.040	6.370
925	1.769	0.006	2.247	0.000	2.314	0.000	1.654	9.04E-4	0.040	6.555
950	1.757	0.007	2.245	0.000	2.304	0.000	1.652	8.35E-4	0.040	6.740
975	1.745	0.008	2.243	0.000	2.296	0.000	1.650	7.75E-4	0.040	6.925
1000	1.732	0.008	2.241	0.000	2.289	0.000	1.648	7.22E-4	0.040	7.160
1025	1.719	0.009	2.239	0.000	2.283	0.000	1.646	6.76E-4	0.040	7.426
1050	1.706	0.010	2.238	0.000	2.277	0.000	1.644	6.35E-4	0.040	7.691
1075	1.692	0.011	2.236	0.000	2.270	0.000	1.642	5.98E-4	0.045	7.896
1100	1.678	0.012	2.235	0.000	2.268	0.000	1.640	5.66E-4	0.053	8.061
1125	1.664	0.014	2.233	0.000	2.267	0.000	1.638	5.36E-4	0.061	8.227
1150	1.649	0.015	2.232	0.000	2.262	0.000	1.636	5.11E-4	0.069	8.393
1175	1.633	0.017	2.231	0.000	2.257	0.000	1.634	4.87E-4	0.077	8.558
1200	1.618	0.018	2.229	0.000			1.633	4.66E-4	0.085	8.724

B

Fitted Diode-Model Parameters

This appendix contains the parameters extraction results, shown as red circles, and the mathematical fittings of the parameters' behaviours, shown as blue line.

Silicon Heterojunction Model Cell - Irradiance Effect

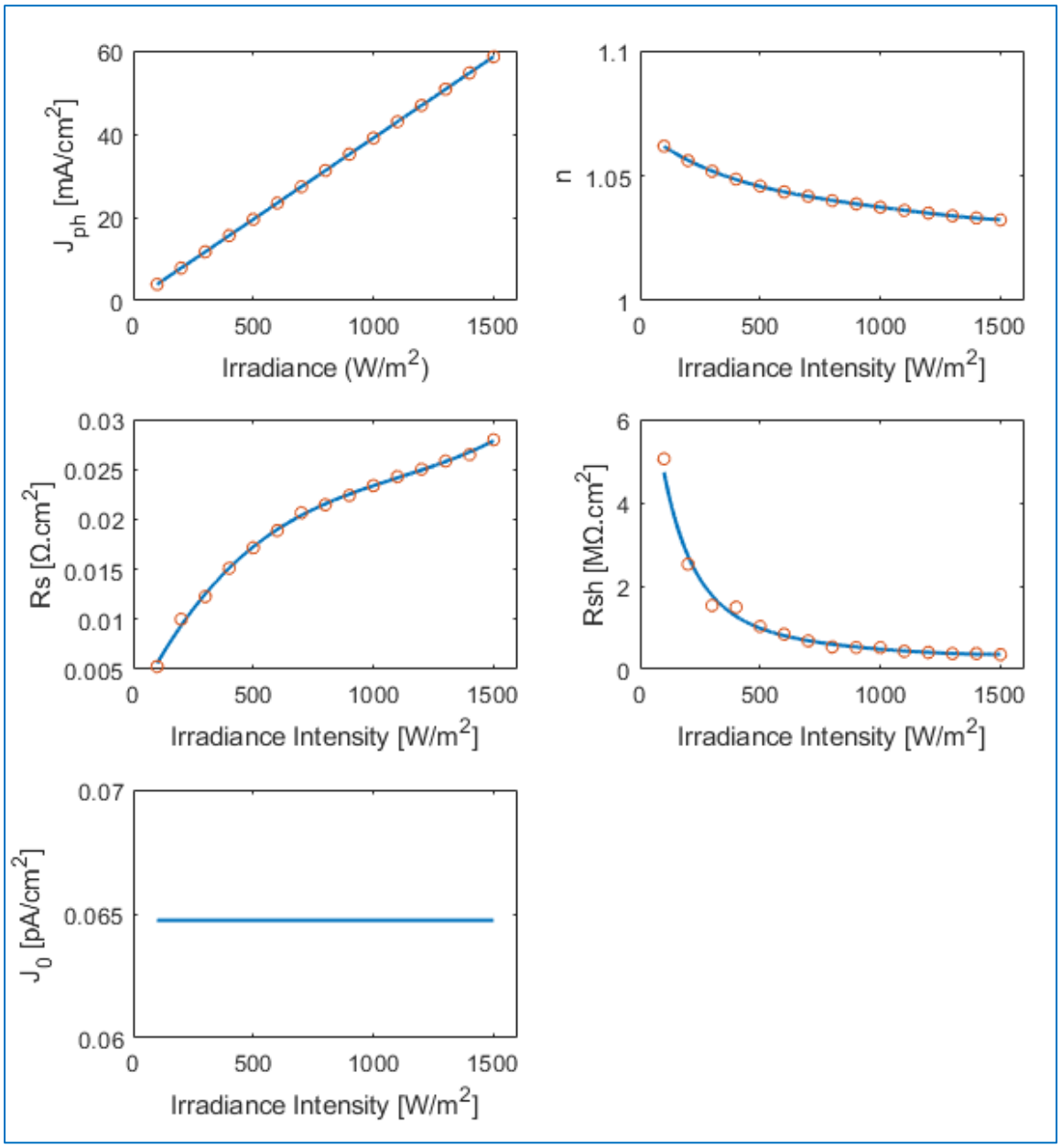

Figure B.1 Irradiance effect on SHJ parameters.

Silicon Heterojunction Model Cell - Temperature Effect

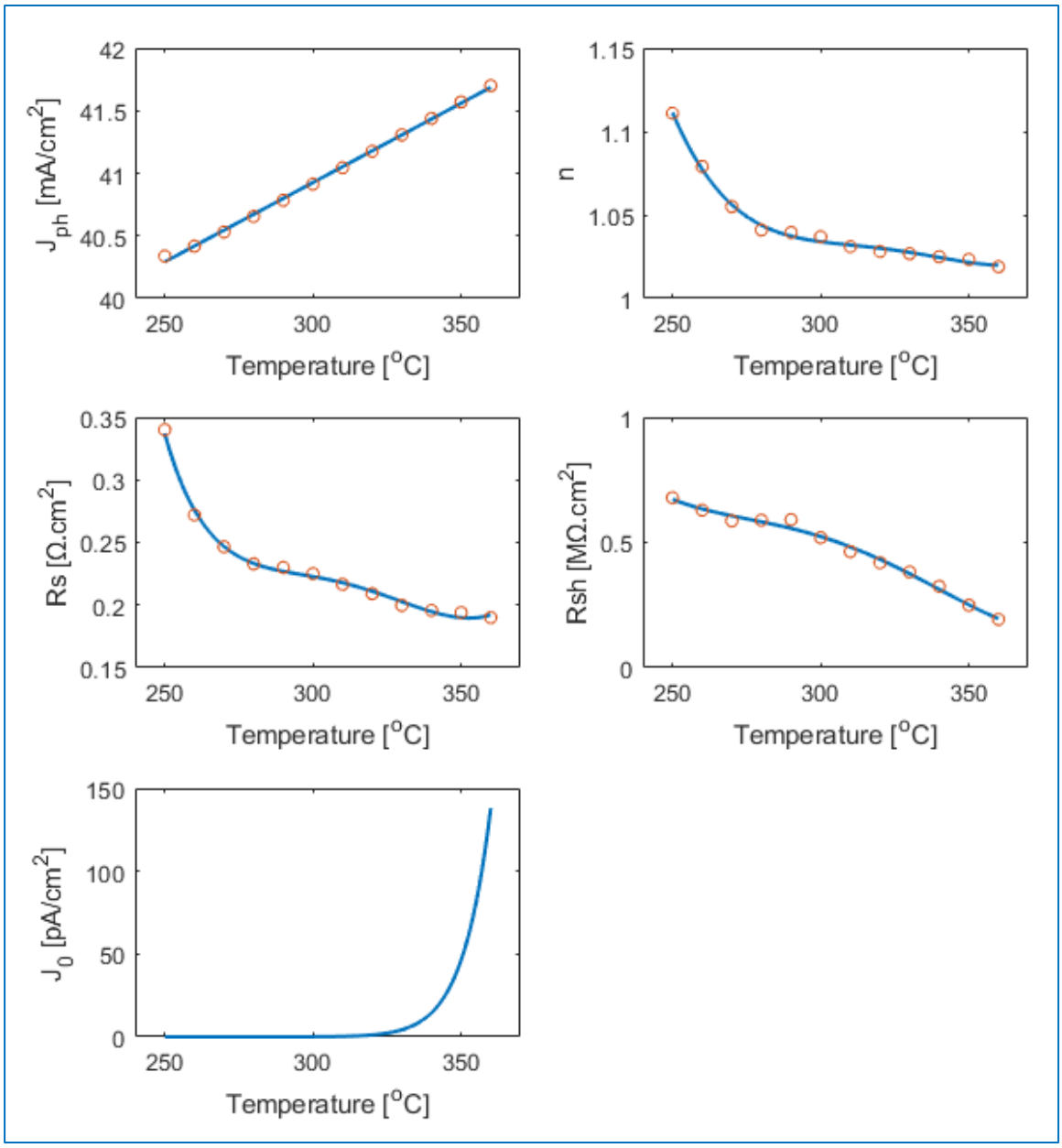

Figure B.2 Temperature effect on SHJ parameters.

Perovskite Model Cell - Irradiance Effect

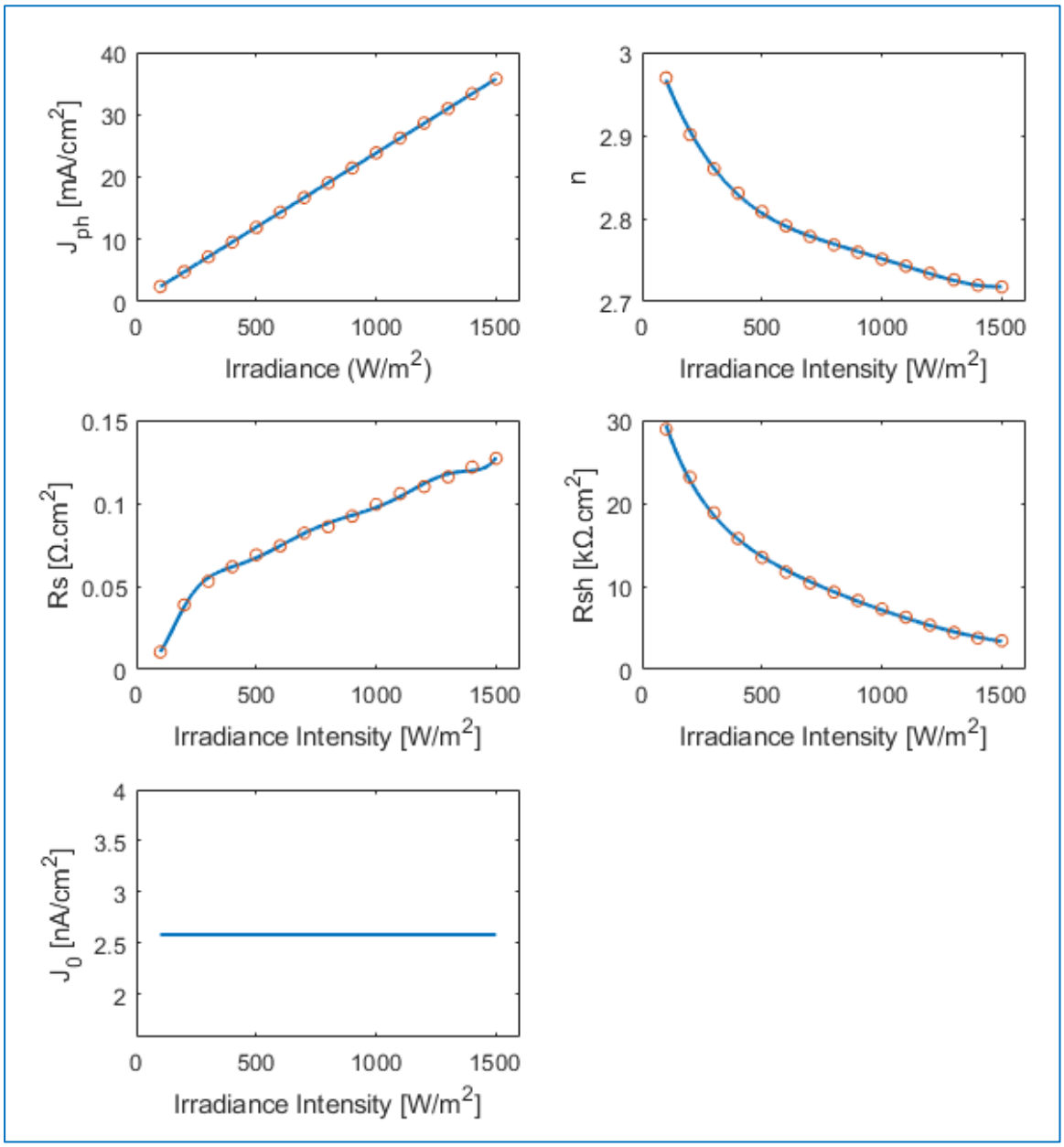

Figure B.3 Irradiance effect on perovskite parameters.

Perovskite Model Cell - Temperature Effect

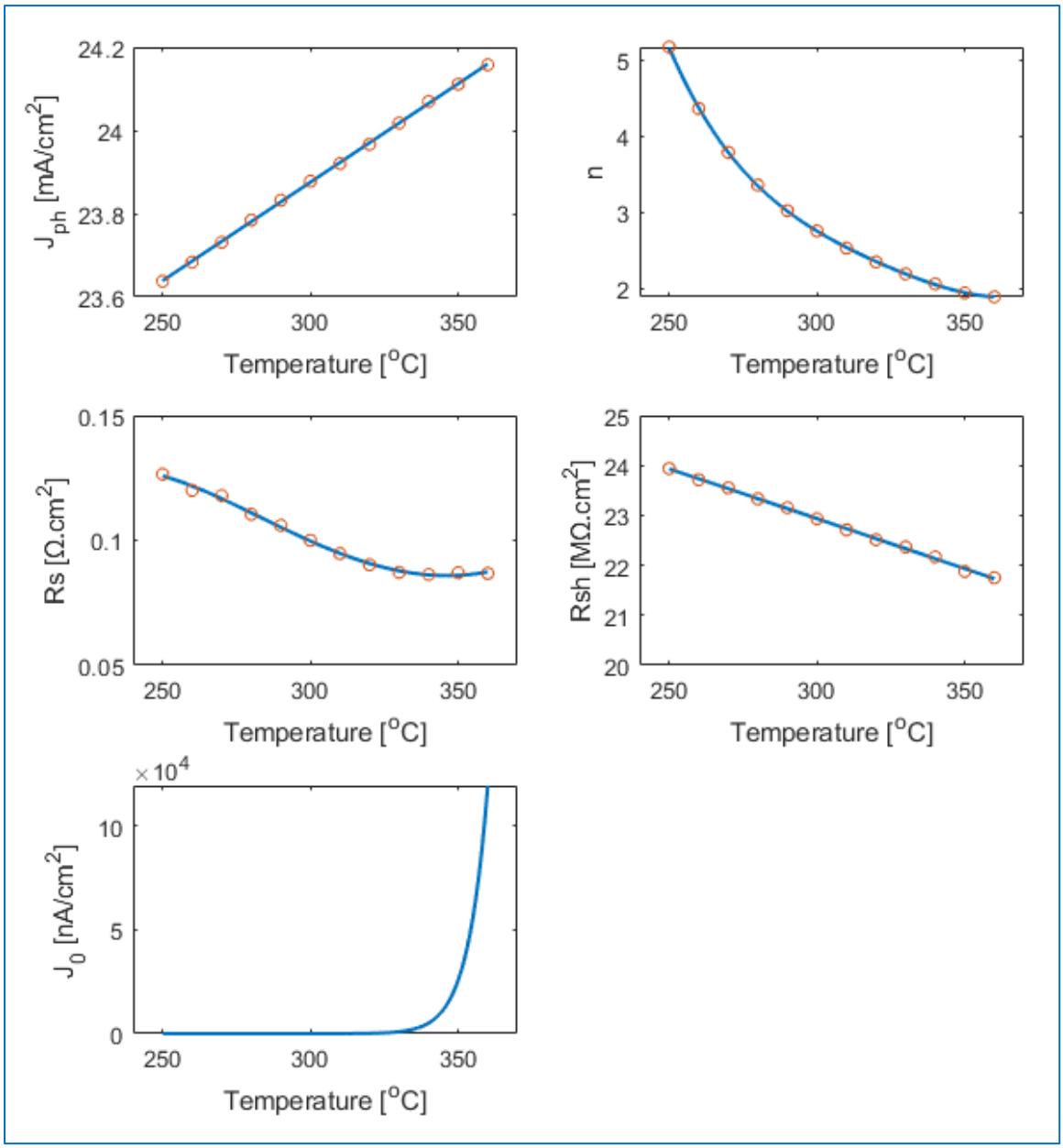

Figure B.4 Temperature effect on perovskite cell parameters.

Bibliography

[1] D. Spencer, “BP Statistical Review of World Energy Statistical Review of World,” 2019. [Online]. Available: https://www.bp.com/content/dam/bp/business-sites/en/global/corporate/pdfs/energy-economics/statistical-review/bp-stats-review-2019-full-report.pdf.

[2] V. Smil, “World History and Energy,” *Encycl. Energy*, vol. 6, pp. 549–561, 2004, doi: 10.1016/b0-12-176480-x/00025-5.

[3] IRENA, *Renewable Energy Statistics 2019*, vol. 1, no. 1. 2019.

[4] “A Fundamental Look At Supply Side Energy Reserves For The Planet,” 2015. doi: 10.1016/j.eneco.2008.12.011.

[5] “Renewable Power Generation Costs in 2018,” 2019. doi: 10.1007/springerreference_7300.

[6] M. Gaetan, O. Sinead, and R. Manoel, “Global Market Outlook For Solar Power / 2018 - 2022,” 2018. doi: 10.1787/key_energ_stat-2014-en.

[7] M. Hosenuzzaman, N. A. Rahim, J. Selvaraj, M. Hasanuzzaman, A. B. M. A. Malek, and A. Nahar, “Global prospects, progress, policies, and environmental impact of solar photovoltaic power generation,” *Renew. Sustain. Energy Rev.*, vol. 41, no. November, pp. 284–297, 2015, doi: 10.1016/j.rser.2014.08.046.

[8] W. Shockley and H. J. Queisser, “Detailed balance limit of efficiency of p-n junction solar cells,” *J. Appl. Phys.*, vol. 32, no. 3, pp. 510–519, 1961, doi: 10.1063/1.1736034.

[9] A. Smets, K. Jager, O. Isabella, R. Van Swaaij, and M. Zeman, *Solar Energy The physics and engineering of photovoltaic conversion, technologies and systems*. UIT Cambridge, 2016.

[10] N. S. A. S. Pujari, “International Technology Roadmap for Photovoltaic (ITRPV),” 2018. [Online]. Available: http://www.ncbi.nlm.nih.gov/pubmed/14945410.

[11] G. E. Eperon, M. T. Hörantner, and H. J. Snaith, “Metal halide perovskite tandem and multiple-junction photovoltaics,” *Nat. Rev. Chem.*, vol. 1, no. 12, 2017, doi: 10.1038/s41570-017-0095.

[12] A. De Vos, “Detailed balance limit of the efficiency of tandem solar cells,” *J. Phys. D. Appl. Phys.*, vol. 13, no. 5, pp. 839–846, 1980, doi: 10.1088/0022-3727/13/5/018.

[13] Z. Wang, Z. Song, Y. Yan, S. (Frank) Liu, and D. Yang, “Perovskite—a Perfect Top Cell for Tandem Devices to Break the S–Q Limit,” *Adv. Sci.*, vol. 6, no. 7, 2019, doi: 10.1002/advs.201801704.

[14] T. Duong *et al.*, “Rubidium Multication Perovskite with Optimized Bandgap for Perovskite-Silicon Tandem with over 26% Efficiency,” *Adv. Energy Mater.*, vol. 7, no. 14, pp. 1–11, 2017, doi: 10.1002/aenm.201700228.

[15] S. Albrecht *et al.*, “Towards optical optimization of planar monolithic perovskite/silicon-heterojunction tandem solar cells,” *J. Opt. (United Kingdom)*, vol. 18, no. 6, 2016, doi: 10.1088/2040-8978/18/6/064012.

[16] M. A. Green, A. Ho-Baillie, and H. J. Snaith, “The emergence of perovskite solar cells,” *Nat. Photonics*, vol. 8, no. 7, pp. 506–514, 2014, doi: 10.1038/nphoton.2014.134.

[17] H. T. C. Pedro and C. F. M. Coimbra, "Assessment of forecasting techniques for solar power production with no exogenous inputs," *Sol. Energy*, vol. 86, no. 7, pp. 2017–2028, 2012, doi: 10.1016/j.solener.2012.04.004.

[18] R. Shah, N. Mithulananthan, R. C. Bansal, and V. K. Ramachandaramurthy, "A review of key power system stability challenges for large-scale PV integration," *Renew. Sustain. Energy Rev.*, vol. 41, pp. 1423–1436, 2015, doi: 10.1016/j.rser.2014.09.027.

[19] S. J. Steffel, P. R. Caroselli, A. M. Dinkel, J. Q. Liu, R. N. Sackey, and N. R. Vadhar, "Integrating solar generation on the electric distribution grid," *IEEE Trans. Smart Grid*, vol. 3, no. 2, pp. 878–886, 2012, doi: 10.1109/TSG.2012.2191985.

[20] J. Umuhoza, Y. Zhang, S. Zhao, and H. A. Mantooth, "An adaptive control strategy for power balance and the intermittency mitigation in battery-PV energy system at residential DC microgrid level," *Conf. Proc. - IEEE Appl. Power Electron. Conf. Expo. - APEC*, pp. 1341–1345, 2017, doi: 10.1109/APEC.2017.7930870.

[21] B. Sivaneasan, N. K. Kandasamy, M. L. Lim, and K. P. Goh, "A new demand response algorithm for solar PV intermittency management," *Appl. Energy*, vol. 218, no. March, pp. 36–45, 2018, doi: 10.1016/j.apenergy.2018.02.147.

[22] J. Torriti, M. G. Hassan, and M. Leach, "Demand response experience in Europe: Policies, programmes and implementation," *Energy*, vol. 35, no. 4, pp. 1575–1583, 2010, doi: 10.1016/j.energy.2009.05.021.

[23] F. Ueckerdt, R. Brecha, and G. Luderer, "Analyzing major challenges of wind and solar variability in power systems," *Renew. Energy*, vol. 81, pp. 1–10, 2015, doi: 10.1016/j.renene.2015.03.002.

[24] G. Gowrisankaran, S. S. Reynolds, and M. Samano, "Intermittency and the value of renewable energy," *J. Polit. Econ.*, vol. 124, no. 4, pp. 1187–1234, 2016, doi: 10.1086/686733.

[25] M. GREEN *et al.*, "Regional PV power prediction for improved grid integration," *Ieee Trans Fuzzy Syst*, 2012. .

[26] N. Blair *et al.*, "System Advisor Model (SAM) General Description," 2018. [Online]. Available: https://www.nrel.gov/docs/fy18osti/70414.pdf.

[27] "PVSyst Features." https://www.pvsyst.com/features/ (accessed Dec. 10, 2019).

[28] T. Gurupira, A. J. Rix, T. Gurupira, and A. J. Rix, "Pv Simulation Software Comparisons: Pvsyst, Nrel Sam and Pvlib," no. February, 2017, [Online]. Available: https://www.researchgate.net/publication/313249367.

[29] B. Djaber, J. Libal, and S. Gluntz, "MoBiDiG: simulations and LCOE," 2017. https://www.researchgate.net/publication/322626669_MoBiDiG_simulations_and_LCOE (accessed Dec. 10, 2019).

[30] "THE POTENTIAL OF BIFACIAL PV," 2018. https://www.tno.nl/en/about-tno/news/2018/7/the-potential-of-bifacial-pv/ (accessed Nov. 28, 2019).

[31] "ENHANCED ENERGY YIELD AND NOVEL APPLICATIONS WITH DOUBLE-SIDED (BIFACIAL) PV." https://www.tno.nl/en/focus-areas/ecn-part-of-tno/roadmaps/towards-ubiquitous-solar-energy/global-leader-with-innovative-solar-panels/enhanced-energy-yield-and-novel-applications-with-double-sided-bifacial-pv/

(accessed Nov. 27, 2019).

[32] "HIGHER YIELD AND BETTER INTEGRATION IN LANDSCAPE WITH BIFACIAL SOLAR PANELS." https://www.tno.nl/en/focus-areas/ecn-part-of-tno/roadmaps/towards-ubiquitous-solar-energy/smart-integration-of-solar-energy-into-our-environment/higher-yield-and-better-integration-in-landscape-with-bifacial-solar-panels/ (accessed Nov. 27, 2019).

[33] Z. Wang, "Improvements and Experimental Validation of the PVMD Toolbox," Delft University of Technology, 2018.

[34] R. Santbergen, T. Meguro, T. Suezaki, G. Koizumi, K. Yamamoto, and M. Zeman, "GenPro4 Optical Model for Solar Cell Simulation and Its Application to Multijunction Solar Cells," *IEEE J. Photovoltaics*, vol. 7, no. 3, pp. 919–926, 2017, doi: 10.1109/JPHOTOV.2017.2669640.

[35] R. Santbergen, V. A. Muthukumar, R. M. E. Valckenborg, W. J. A. van de Wall, A. H. M. Smets, and M. Zeman, "Calculation of irradiance distribution on PV modules by combining sky and sensitivity maps," *Sol. Energy*, vol. 150, pp. 49–54, 2017, doi: 10.1016/j.solener.2017.04.036.

[36] E. G. Goma, "Development of Cell to System Annual Energy Yield Toolbox for Bifacial Modules by," 2018.

[37] S. Bowden and A. Rohatgi, "RAPID AND ACCURATE DETERMINATION OF SERIES RESISTANCE AND FILL FACTOR LOSSES IN INDUSTRIAL SILICON and SOLAR CELLS," *17th Eur. Photovolt. Sol. Energy Conf.*, 2001.

[38] M. Zeman *et al.*, "Advanced Semiconductor Analysis: opto-electronic simulator for amorphous and crystalline semiconductor devices," 1997.

[39] V. Franzitta, A. Orioli, and A. di Gangi, "Assessment of the Usability and Accuracy of the Simplified One-Diode Models for Photovoltaic Modules," *Energies*, vol. 9, no. 12, 2016, doi: 10.3390/en9121019.

[40] N. Jensen *et al.*, "Recombination mechanisms in amorphous silicon/crystalline silicon heterojunction solar cells," *J. Appl. Phys.*, vol. 87, no. 5, pp. 2639–2645, 2000, doi: 10.1063/1.372230.

[41] O. Breitenstein, J. P. Rakotoniaina, M. H. Al Rifai, and M. Werner, "Shunt types in crystalline silicon solar cells," *Prog. Photovoltaics Res. Appl.*, vol. 12, no. 7, pp. 529–538, 2004, doi: 10.1002/pip.544.

[42] G. Ciulla, V. Lo Brano, V. Di Dio, and G. Cipriani, "A comparison of different one-diode models for the representation of I-V characteristic of a PV cell," *Renew. Sustain. Energy Rev.*, vol. 32, pp. 684–696, 2014, doi: 10.1016/j.rser.2014.01.027.

[43] A. Orioli and A. Di Gangi, "A criterion for rating the usability and accuracy of the one-diode models for photovoltaic modules," *Energies*, vol. 9, no. 6, 2016, doi: 10.3390/en9060427.

[44] S. xian Lun *et al.*, "An explicit approximate I-V characteristic model of a solar cell based on padé approximants," *Sol. Energy*, vol. 92, pp. 147–159, 2013, doi: 10.1016/j.solener.2013.02.021.

[45] Y. Xu, X. Kong, Y. Zeng, S. Tao, and X. Xiao, "A modeling method for photovoltaic cells using explicit equations and optimization algorithm," *Int. J. Electr. Power Energy Syst.*, vol.

59, pp. 23–28, 2014, doi: 10.1016/j.ijepes.2014.01.017.

[46] J. Cubas, S. Pindado, and C. De Manuel, “Explicit expressions for solar panel equivalent circuit parameters based on analytical formulation and the lambert W-function,” *Energies*, vol. 7, no. 7, pp. 4098–4115, 2014, doi: 10.3390/en7074098.

[47] H. Mekki, a Mellit, H. Salhi, and B. Khaled, “Modeling and simulation of photovoltaic panel based on artificial neural networks and VHDL-language BT - 14th IEEE International Conference on Electronics, Circuits and Systems, ICECS 2007, December 11, 2007 - December 14, 2007,” pp. 58–1424413788, 2007, [Online]. Available: http://dx.doi.org/10.1109/ICECS.2007.4510930.

[48] L. Sandrolini, M. Artioli, and U. Reggiani, “Numerical method for the extraction of photovoltaic module double-diode model parameters through cluster analysis,” *Appl. Energy*, vol. 87, no. 2, pp. 442–451, 2010, doi: 10.1016/j.apenergy.2009.07.022.

[49] A. Askarzadeh and A. Rezazadeh, “Parameter identification for solar cell models using harmony search-based algorithms,” *Sol. Energy*, vol. 86, no. 11, pp. 3241–3249, 2012, doi: 10.1016/j.solener.2012.08.018.

[50] J. A. Jervase, H. Bourdoucen, and A. Al-Lawati, “Solar cell parameter extraction using genetic algorithms,” *Meas. Sci. Technol.*, vol. 12, no. 11, pp. 1922–1925, 2001, doi: 10.1088/0957-0233/12/11/322.

[51] M. GREEN *et al.*, “Solar cell efficiency tables (version 48),” *Ieee Trans Fuzzy Syst*, vol. 20, no. 6, pp. 1114–1129, 2012, doi: 10.1002/pip.

[52] D. Adachi, J. L. Hernández, and K. Yamamoto, “Impact of carrier recombination on fill factor for large area heterojunction crystalline silicon solar cell with 25.1% efficiency,” *Appl. Phys. Lett.*, vol. 107, no. 23, pp. 22–25, 2015, doi: 10.1063/1.4937224.

[53] M. A. Green, Y. Hishikawa, E. D. Dunlop, D. H. Levi, J. Hohl-Ebinger, and A. W. Y. Ho-Baillie, “Solar cell efficiency tables (version 51),” *Prog. Photovoltaics Res. Appl.*, vol. 26, no. 1, pp. 3–12, 2018, doi: 10.1002/pip.2978.

[54] E. H. Jung *et al.*, “Efficient, stable and scalable perovskite solar cells using poly(3-hexylthiophene),” *Nature*, vol. 567, no. 7749, pp. 511–515, 2019, doi: 10.1038/s41586-019-1036-3.

[55] C. S. Ruschel, F. P. Gasparin, E. R. Costa, and A. Krenzinger, “Assessment of PV modules shunt resistance dependence on solar irradiance,” *Sol. Energy*, vol. 133, pp. 35–43, 2016, doi: 10.1016/j.solener.2016.03.047.

[56] E. L. Meyer, “Extraction of Saturation Current and Ideality Factor from Measuring Voc and Isc of Photovoltaic Modules,” *Int. J. Photoenergy*, vol. 2017, 2017, doi: 10.1155/2017/8479487.

[57] P. Baruch, A. De Vos, P. T. Landsberg, and J. E. Parrott, “On some thermodynamic aspects of photovoltaic solar energy conversion,” *Sol. Energy Mater. Sol. Cells*, vol. 36, no. 2, pp. 201–222, 1995, doi: 10.1016/0927-0248(95)80004-2.

[58] H. FWolf., *Semiconductors*. 1971.

[59] T. Dittrich, C. Awino, P. Prajongtat, B. Rech, and M. C. Lux-Steiner, “Temperature Dependence of the Band Gap of CH3NH3PbI3 Stabilized with PMMA: A Modulated Surface Photovoltage Study,” *J. Phys. Chem. C*, vol. 119, no. 42, pp. 23968–23972, 2015,

doi: 10.1021/acs.jpcc.5b07132.

[60] M. Chegaar, A. Hamzaoui, A. Namoda, P. Petit, M. Aillerie, and A. Herguth, “Effect of illumination intensity on solar cells parameters,” *Energy Procedia*, vol. 36, pp. 722–729, 2013, doi: 10.1016/j.egypro.2013.07.084.

[61] P. Singh, S. N. Singh, M. Lal, and M. Husain, “Temperature dependence of I-V characteristics and performance parameters of silicon solar cell,” *Sol. Energy Mater. Sol. Cells*, vol. 92, no. 12, pp. 1611–1616, 2008, doi: 10.1016/j.solmat.2008.07.010.

[62] J. A. Eikelboom and A. Reinders, “Determination of the irradiation dependent efficiency of multicrystalline Si PV modules on basis of IV curve fitting and its influence on the annual performance,” *Measurement*, no. January, pp. 2–5, 1997, [Online]. Available: ftp://kerntechniek.nl/pub/www/library/report/1997/rx97045.pdf.

[63] S. Bensalem and M. Chegaar, “Thermal behavior of parasitic resistances of polycrystalline silicon solar cells,” *Rev. des Energies Renouvelables*, vol. 16, no. 1, pp. 171–176, 2013.

[64] M. Leilaeioun and Z. C. Holman, “Accuracy of expressions for the fill factor of a solar cell in terms of open-circuit voltage and ideality factor,” *J. Appl. Phys.*, vol. 120, no. 12, 2016, doi: 10.1063/1.4962511.

[65] V. Lo Brano, A. Orioli, G. Ciulla, and A. Di Gangi, “An improved five-parameter model for photovoltaic modules,” *Sol. Energy Mater. Sol. Cells*, vol. 94, no. 8, pp. 1358–1370, 2010, doi: 10.1016/j.solmat.2010.04.003.

[66] J. W. Bishop, “Computer simulation of the effects of electrical mismatches in photovoltaic cell interconnection circuits,” *Sol. Cells*, vol. 25, no. 1, pp. 73–89, 1988, doi: 10.1016/0379-6787(88)90059-2.

[67] J. Lambert, “Observationes variae in mathesin puram,” *Acta Helvetica, physico-mathematico-anatomico-botanico-medica*, vol. 3. pp. 128–168, 1758.

[68] L. Euler, “De serie Lambertina Plurimisque eius insignibus proprietatibus,” *Acta Acad. Scient. Petropol.*, vol. 2. pp. 29–51, 1783.

[69] A. Jain and A. Kapoor, “Exact analytical solutions of the parameters of real solar cells using Lambert W-function,” *Sol. Energy Mater. Sol. Cells*, vol. 81, no. 2, pp. 269–277, 2004, doi: 10.1016/j.solmat.2003.11.018.

[70] P. Guerriero, P. Tricoli, and S. Daliento, “A bypass circuit for avoiding the hot spot in PV modules,” *Sol. Energy*, vol. 181, no. November 2018, pp. 430–438, 2019, doi: 10.1016/j.solener.2019.02.010.

[71] T. A. Circuits, “SM74611 Smart Bypass Diode SM74611,” no. December, 2012.

[72] G. Papakonstantinou, “Investigation and Optimization of the Front Metal Contact of Silicon Heterojunction Solar Cells,” no. July, 2014.

[73] S. P. Coorporation, “MAXEON ™ GEN II SOLAR CELLS Electrical Characteristics of a typical Maxeon Gen II Cell,” 2017, pp. 3–4.

[74] B. Marion, M. G. Deceglie, and T. J. Silverman, “Analysis of measured photovoltaic module performance for Florida, Oregon, and Colorado locations,” *Sol. Energy*, vol. 110, pp. 736–744, 2014, doi: 10.1016/j.solener.2014.10.017.

[75] C. A. Gueymard, “A review of validation methodologies and statistical performance indicators for modeled solar radiation data: Towards a better bankability of solar projects,”

Renew. Sustain. Energy Rev., vol. 39, pp. 1024–1034, 2014, doi: 10.1016/j.rser.2014.07.117.

[76] C. J. Willmott, "On the validation of models," *Phys. Geogr.*, vol. 2, no. 2, pp. 184–194, 1981, doi: 10.1080/02723646.1981.10642213.

[77] D. R. Myers, *Solar radiation: Practical modeling for renewable energy applications*. 2017.

[78] A. T. Young, "Air mass and refraction," *Appl. Opt.*, vol. 33, no. 6, p. 1108, 1994, doi: 10.1364/ao.33.001108.

[79] M. Iqbal, *An Introduction to Solar Radiation*, vol. 47, no. 5. 1983.

[80] B. Ridley, J. Boland, and P. Lauret, "Modelling of diffuse solar fraction with multiple predictors," *Renew. Energy*, vol. 35, no. 2, pp. 478–483, 2010, doi: 10.1016/j.renene.2009.07.018.

[81] K. Lee, H. Yoo, and G. J. Levermore, "Quality control and estimation hourly solar irradiation on inclined surfaces in South Korea," *Renew. Energy*, vol. 57, pp. 190–199, 2013, doi: 10.1016/j.renene.2013.01.028.

[82] D. T. REINDL, W. A. BECKMAN, and D. J. A., "Diffuse fraction correlations," *Sol. Energy*, vol. 47, no. 4, pp. 311–312, 1991, doi: 10.1016/0038-092X(91)90123-E.

[83] A. Jamodkar, "Energy Yield Prediction of Solar Powered E-Bike Charging Station," 2017.

[84] J. A. Duffie and W. A. Beckmann, *Solar Engineering of Thermal Processes*, 4th ed. Wiley, 2016.

[85] A. D. Jones and C. P. Underwood, "A thermal model for photovoltaic systems," *Fuel Energy Abstr.*, vol. 43, no. 3, p. 199, 2002, doi: 10.1016/s0140-6701(02)85831-3.

[86] E. Ruiz-reina, M. Sidrach-de-cardona, and M. Piliougine, "Heat Transfer and Working Temperature Field of a Photovoltaic Panel under Realistic Environmental Conditions," pp. 1–3.

[87] S. Armstrong and W. G. Hurley, "A thermal model for photovoltaic panels under varying atmospheric conditions," *Appl. Therm. Eng.*, vol. 30, no. 11–12, pp. 1488–1495, 2010, doi: 10.1016/j.applthermaleng.2010.03.012.

[88] J. H. Watmuff, W. W. F. Charters, and D. Proctor, "Solar and wind induced external coefficients - Solar collectors," *Rev. Int. d'Heliotechnique*, p. 56, 1977.

[89] D. I. Ladas and T. Stathopoulos, "Wind effects on the performance of solar collectors on roofs 1 2," 2004.

[90] W. Marion *et al.*, "User's Manual for Data for Validating Models for PV Module Performance," no. April, 2014.

[91] K. Y. Bae, H. S. Jang, and D. K. Sung, "Hourly Solar Irradiance Prediction Based on Support Vector Machine and Its Error Analysis," *IEEE Trans. Power Syst.*, vol. 32, no. 2, pp. 935–945, 2017, doi: 10.1109/TPWRS.2016.2569608.

[92] J. G. da S. Fonseca, H. Ohtake, T. Oozeki, and K. Ogimoto, "Prediction intervals for day-ahead photovoltaic power forecasts with non-parametric and parametric distributions," *J. Electr. Eng. Technol.*, vol. 13, no. 4, pp. 1504–1514, 2018, doi: 10.5370/JEET.2018.13.4.1504.

[93] T. L. Bergman, A. S. Lavine, F. P. Incropera, and D. P. Dewitt, *Fundamentals of Heat and Mass Transfer*, 7th ed. John Wiley & Sons, 2012.

[94] E. Kaplani and S. Kaplanis, "Thermal modelling and experimental assessment of the dependence of PV module temperature on wind velocity and direction, module orientation and inclination," *Sol. Energy*, vol. 107, pp. 443–460, 2014, doi: 10.1016/j.solener.2014.05.037.

[95] E. Yablonovitch and G. D. Coady, "Intensity Enhancement in Textured Optical Sheets for Solar Cells," *IEEE Trans. Electron Devices*, vol. 29, no. 2, pp. 300–305, 1982, doi: 10.1109/T-ED.1986.22753.

[96] J. Lehr *et al.*, "Energy yield modelling of perovskite/silicon two-terminal tandem PV modules with flat and textured interfaces," *Sustain. Energy Fuels*, vol. 2, no. 12, pp. 2754–2761, 2018, doi: 10.1039/c8se00465j.

[97] A. Usami and N. Kawasaki, "Modeling of solar spectral irradiance data from cloudless to overcast skies," *Jpn. J. Appl. Phys.*, vol. 51, no. 10 PART 2, 2012, doi: 10.1143/JJAP.51.10NF06.

[98] "ITO measurements at TU Delft /PVMD."

[99] "p-type a-Si fabricated and measured at TU Delft," 1998.

[100] M. A. Green and M. J. Keevers, "Optical Properties of Intrinsic Silicon at 300K," *Prog. Photovoltaics*, vol. 3, pp. 189–192, 1995.

[101] "a-Si(n) measurements at TU Delft / PVMD."

[102] P. B. Johnson and R. . Christy, "Optical Constants of Noble Metals," *Phys. Rev. B*, vol. 6, no. 12, pp. 4370–4379, 1972.

[103] J. Sap., "Measurements at TU Delft / PVMD."

[104] J. Blanker, "TiO2 measurements at TU Delft /PVMD," 2015.

[105] P. Loper and E. Al., "Complex Refractive Index Spectra of CH3NH3PbI3 Perovskite Thin Films," *J. Phys. Chem. Lett.*, no. 6, pp. 66–71, 2015.

[106] R. Santbergen and J. Blanker, "PTAA Measurements at TU Delft," 2015.